NOVEL DESIGN AND DEVELOPMENT OF PDMS-GLASS HYBRID MICROFLUIDIC DEVICES FOR CONTINUOUS DOUBLE ENCAPSULATION OF LIQUID-OIL DROPLETS

LIM CHANG NONG

THESIS SUBMITTED TO THE UNIVERSITY OF NOTTINGHAM FOR THE DEGREE OF DOCTOR OF PHILOSOPHY

APRIL 2018

ABSTRACT

Microfluidics have been a topic studied intensely until current by most of the researchers due to its broad application in different industry sector. Comparing to the conventional bulk method, fabrication of double emulsion droplets using microfluidic technique is the highly sought-after method as it provides a flexible platform which enabled the generation of highly monodispersed droplets. Current technology shows establishment on glass capillary and polydimethylsiloxane (PDMS) microfluidic device, while the researchers continue to develop simple and facile platform with different materials competent to their applications.

Multiphase flow was involved in generating the double emulsion droplets and hence the significance of the fluid wetting properties and the intrinsic properties of the respective material. Localised surface treatment in a one-chip configuration microfluidic device, however, is a complex procedure which involves expensive chemicals with short recovery period. Therefore, this thesis aimed to develop and fabricate a cost-effective hybrid microfluidic device, able to generate monodisperse W/O/W double emulsion droplets without chemical surface treatment.

By utilising the two commonest materials i.e. glass capillary tube and PDMS, a PDMS-Glass Capillary Hybrid Microfluidic Device (PGHD) was developed. To further establish the system, the standard operating procedure (SOP) was developed to enable definite start-up of the experiment. On top of that, the fabrication methodology was optimised to improve the efficiency and precision. The design geometry was modified and optimised accordingly to ensure the practicability of the PGHD. Quantitative experimental analysis was carried out to understand the flow profile and droplet behaviour in the PGHD, which then enable the manipulation of the parameters such as flow rate ratio accordingly to achieve the desired number of encapsulation.

LIST OF PUBLICATIONS AND PAPERS PRESENTED

1. **C.N. Lim**, K.S. Koh and J.K. Chin, *'Monodisperse Multiple Droplets Encapsulation in Polydimethylsiloxane (PDMS) – Glass Capillary Hybrid Microfluidic Device'*, 8th International Symposium on Microchemistry and Microsystems, Hong Kong, China, May 2016
2. **C.N. Lim**, Y. Ren, K.S. Koh and J.K. Chin, *'Numerical Model for Droplet Encapsulation in a Polydimethylsiloxane (PDMS) – Glass Capillary Hybrid Microfluidic Device'*, Lab on a Chip International Symposium: Droplet-based Microfluidics, Hangzhou, China, November 2016
3. **C. N. Lim**, K. S. Koh, Y. Ren, J. K. Chin, Y. Shi, and Y. Yan, "Analysis of liquid-liquid droplets fission and encapsulation in single/two layer microfluidic devices fabricated by xurographic method," *Micromachines*, vol. 8, no. 2, p. 49, Feb. 2017.
4. **C.N. Lim** and J.K. Chin, "Fabrication of Microgel Particles with a Microfluidic Approach," in *Microgels: Synthesis, Properties and Applications*, W.F. Lai, Ed. Nova Science New York, 2018 [Accepted and in production]

ACKNOWLEDGEMENTS

When I first started this project, there was a period where I failed countless time on the experiments worked just fine previously. I did not know why and I got tired of doing it until I came across part of the movie, "Frankenweenie" one night. The young boy, Victor asked his science teacher, Mr Rzykruski: *I was doing my experiment, my project, and the first time it worked great, but the next time it didn't. I mean, it sort of worked, but then it didn't. And I don't know why.* Mr Rzykruski replied: *Then maybe you never really understood it the first time. People think science is here (points to his head), but it is also here (places his hand on his chest). The first time, did you love your experiment?* Victor: *Yes.* Mr Rzykruski: *And the second time?* Victor: *No. I just wanted it over.* Mr Rzykruski: *Then you changed the variables.* Victor: *I was doing it for the wrong reason.* Mr Rzykruski: *Science is not good or bad, Victor. But it can be used both ways. That is why you must always be careful.* These dialogues have made me thought about how I have treated my experiments after few successful trials, where I just wanted to collect as much data as possible to finish my project but forgot about my initial passion and motive. Since then, I have always kept that in mind, in case I lost myself again.

Upon completion of this thesis, I can finally call myself a qualified researcher and I would like to express my sincere gratitude to MyBrain15 by Ministry Of Higher Education for offering the scholarship sustaining my PhD study. Not to mention the Faculty of Engineering, University of Nottingham Malaysia Campus for waiving the tuition fees. It has been a great help, and if not because of the financial support I will never had the chance to pursue my study.

When I first consulted my main supervisor, Dr Chin Jit Kai on the research project, he told me that, I should know my research better than him at the end of the day. This eventually becomes my motivation to maintain my learning curve throughout. I am truly grateful on his advice and guidance, which always motivates me to strive better. Apart

from my main supervisor, I would also like to thank my co-supervisors: Dr Lee Lai Yee and Dr Koh Kai Seng, offering useful advice and suggestions whenever needed. They have all supervised and guided me well as a mentor and friend. I would also like to acknowledge Dr Yong REN (UNNC) for contributing his knowledge on simulation to help me better understand the fluid dynamics. Throughout my studies, I have received kind support and assistance from the UNMC laboratory staff and faculty staff– Mr Andrew Yakin Sinit, Mr Ahmad Fareez Mohd Rawi, Mr Muhamd Asyraf Samsudin, Ms. Siti Zaharatul Asyiqin, Ms. Galoh Munawwarah Osman and Ms. Yogeswary Arumugam, which I truly appreciate.

Now to all my PhD seniors/ colleagues/ friends in both UNMC and UNNC who have supported, encouraged, provide useful advice and brought me joy. Their existence were what made this journey meaningful and I cherish every moment spending with them – Dr. Wai Siong Chai, Dr. Kalaimani Markandan, Dr. Chel Gee Ooi, Dr. Joanna Su Yuin Chia, Dr. Patrick WC Ho, Dr. Chun Hsion Lim, Dr. Fah Keen Chong, Ms.Yuh Xiu Liew, Ms. Jessica Lay See Lim, Dr. Min Hui Yap, Dr. Lele Zhang, Dr Feicheng Wang, Dr Bin Dong, Dr Honglei Zhang, Dr. Tingting Ying, Mr Jiawei Zhang, Ms. Huajun He, Ms. Hui Yi Leong, Mr. Chung Hong Tan, Mr. Qi Yan Siew, Mr. Billie Yan Zhang Hiew, Mr. Jing Yang Tan, Mr. Jiawei Zuo, Mr. Han Leong Lim and the others whom were not mentioned.

Special thanks to Mr. Eugene Kan Tak King for grammar correction and sentence restructure during my thesis writing period.

Lastly, I would like to dedicate this thesis to my family – Mr. Voon Leong Lim, Ms. Siew Hah Tho, Ms. Chang Cheng Lim, Mr. Kia Kin Cheok, Ms. Siew Eng Tho, Ms. Ee Lein Cheok and family, Mr. Shen Keat Cheok and Ms. Ee San Cheok for never stopping me from pursuing my dream, no matter how ridiculous they seem to be.

TABLE OF CONTENTS

LIST OF FIGURES

LIST OF TABLES

LIST OF SYMBOLS AND ABBREVIATIONS

2D	:	two-dimensional
3D	:	three-dimensional
Ca	:	capillary number
CV	:	coefficient of variance
CVD	:	chemical vapour deposition
DI	:	deionised
O/W	:	oil-in-water
O/W/O	:	oil-in-water-in-oil
PDMS	:	polydimethylsiloxane
PGHD	:	PDMS – glass capillary hybrid microfluidic device
PLA	:	polylactic acid
PMMA	:	polymethylmenthacrylate
PTFE	:	polytetrafluoroethylene
Q_c	:	volumetric flow rate of the continuous phase
Q_d	:	volumetric flow rate of the dispersed phase
SOP	:	standard operating procedure
W/O	:	water-in-oil
W/O/W	:	water-in-oil-in-water
We	:	weber number
γ	:	interfacial tension
φ	:	flow ratio
v_{sp}	:	superficial velocity

CHAPTER 1: INTRODUCTION

1.1 Definitions of Microfluidics

Microfluidics define the science and engineering of a small-scale fluid system. It is a study of design, fabrication and operation of a system conducting fluids in microscopic channels of widths or diameters ranging from 10 – 500 micrometres (μm). The use of micron-scale capillaries was first introduced by Ganan-Calvo [1] and was established when Thorsen *et al.* [2] demonstrated the use of a simple T-junction microfluidic device to control the flow of immiscible liquids, forming monodisperse droplets. The manipulation of discrete fluid packets in micro-droplets provide benefits in large reduction of reagent volume, size of sample and the equipment [3]. This opened a completely new wave of interest in microfluidic systems in a broad range of fields such as biochemical, engineering and pharmaceutical benefits from the advantages of small and precise.

Droplet-based microfluidics, one subcategory of microfluidics focuses on the discrete volumes creation with the use of immiscible phases and perform many reactions under confined spatial and temporal control. Highly monodisperse droplets can be generated and manipulated in terms of droplet fusion [4], droplet fission [5], mixing in droplets [6] and droplet sorting [7]. They are applied for irregular particles [8], double emulsions [9], microcapsules [10, 11] and microbubbles[12]–[14]. Created particles were used in a diverse range of applications such as synthesis of biomolecules, drug delivery and diagnostic testing [15].

1.2 Project Background and Motivations

Emulsion was defined as the dispersion of liquid droplet into an immiscible fluid which can be produced in bulk by mixing the two with the addition of surfactants. Double

emulsion, was first discovered by William Seifriz [16] in 1925, known as a more complex nested system of droplets, produced via the two-stage emulsification method [17] to encapsulate the emulsion droplets by introducing another immiscible fluid. Emulsion droplets and double emulsion droplets can be differentiated in two groups: water-in-oil (W/O) emulsion or oil-in-water (O/W) emulsion and water-in-oil-in-water (W/O/W) double emulsion or oil-in-water-in-oil (O/W/O) double emulsion. The difference between W/O emulsion and O/W emulsion falls on the captives' ingredients: W/O emulsion encapsulate water-based ingredients whereas O/W emulsion encapsulate oil-based ingredients. Large quantities of emulsions and double emulsions can be generated in bulk but produce polydisperse internal and external droplets since the individual droplet formation is not regulated. The polydispersity of the droplets limited its application in field required ordered structures [18]. Hence, intensive studies have been carried out to produce highly monodispersed droplets [19].

Compared to the conventional bulk methods, microfluidic techniques provide a powerful platform enables the creation of highly controllable emulsion droplets with precise controlled in size, shape and composition. This precision allows the synthesis of functional micro-droplets and micro-particles which can be tailored as templates to a vast range of applications in chemical and biological field. The core-shell structure of the micro-droplets made them ideally suitable in protecting the captured active ingredients such as pharmaceutical drugs, nutrients and enzymes then act as a carrier until the desired released site. On top of the great potential in drug discovery and genomics [20], micro-encapsulated droplets also known as a great tool in biomedical research and single-cell studies where the polymer particles exploit the binding of biological molecules useful for sensing and separation of biological molecules [21].

The huge potential lies within the double emulsion droplets urged researchers to develop flexible platforms to generate highly monodispersed encapsulated droplets with diverse structures. Recent technology shows establishment on glass capillary microfluidic device due to its robustness and chemical compatibility as compared to the polydimethylsiloxane (PDMS) microfluidic devices. However, the production of glass capillary microfluidic device is labour intensive as it requires manual assembly and high cost due to the equipment required i.e. micro-pipette puller and micro-forge [22, 23]. In addition, the glass capillary microfluidic devices offer only coaxial flow limiting the design flexibility. In contrast, PDMS microfluidic devices offer low cost fabrication and allow mass production from a single master mould. Although its organic solvents incompatibility narrows the chemical applications, the gas permeability allowing the culture of live cells is highly desirable for biological assays [20].

The crucial factor when dealing with droplet formation and encapsulation in micro-channel devices, is the role of the fluids wetting properties with respect to the channel wall. This is because the wetting properties determine whether the injected fluid will flow continuously in the main channel or intermittently adhere to the channel wall [24]. Fluid with similar wetting properties to the channel wall normally act as the continuous phase, shearing the dispersed immiscible fluid to form droplets. For example, W/O emulsion droplets can only be produced under a hydrophobic surface environment and vice versa to prevent the wetting of microchannel surface leading to simultaneous two-phase flow. Hence, the intrinsic surface properties of both glass capillary tube and PDMS has become the biggest obstruction to be overcome, where the problem was mostly adapted by implementing surface modification either by chemical or physical such as chemical vapour deposition (CVD), plasma treatment [2], silanisation and siliconisation [3], [25].

Two-chips configuration was used to produce double emulsion droplets, where the surface properties can be simply modified by using two devices with different materials. However, the connection between the two-chips disturbs the fluid velocity and lead to uncontrollable encapsulation [26]. As the microfluidic devices advanced from two-chips to one-chip configuration [27], the surface treatment becomes more tedious involving localised surface modification in a single chip [26, 28]–[31] as reported in most of the written papers. Besides, the involvement of expensive chemicals, the short recovery period and the lengthy procedure further complex the fabrication process. In most of the reported droplet encapsulation work, detailed description on the fluid delivery sequence and stabilisation period was never reported, where authors only indicate qualitative steady-state droplets for results analysis and discussion. The simple and straightforward instructions, however, was limited especially for a novice in the field of microfluidic. In addition, different starting protocols resulted in different flow mechanism of the encapsulation process.

1.3 Research Scope and Novelty

In this research work, the physical advantages of both glass capillary tube and PDMS were exploited to design and fabricate a PDMS – Glass Capillary Hybrid Microfluidic Device (PGHD), able to generate monodispersed W/O/W double emulsion droplets. Figure 1-1 shows the structure of this thesis.

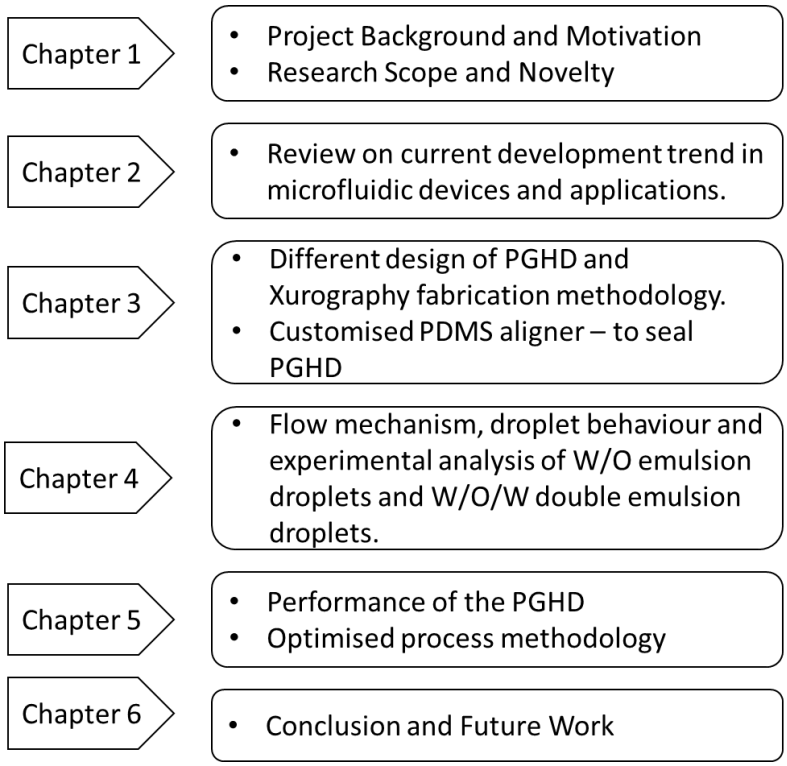

Figure 1-1. Thesis Structure.

The problem statement can be concluded:

(1) Current double emulsion platform required localised surface modification, involving expensive chemicals and complicated the fabrication process, producing only temporary effect.
(2) Most encapsulation work do not report on the fluid delivery sequence and stabilisation period, resulting a research gap especially to novice who wished to apply microfluidic technique to their field.

The aim of this PhD studies is to fabricate a low-cost hybrid microfluidic device, with design flexibility and allows systematic production of monodisperse W/O/W double emulsion droplets. With that, the project objectives are:

(1) To design a custom made PDMS aligner for alignment and sealing of PGHD.

(2) To develop standard operating procedure (SOP) enable definite start-up with reference to the device material, generalising the applicability of microfluidic device.

(3) To study the liquid-liquid droplets interaction and behaviour in a hybrid surface environment, as a template for future modification.

The novelty of the work can be summarised as follow:

(1) Development of PGHD with the ability to generate monodispersed W/O/W double emulsion droplets without the need of chemical surface treatment.

(2) Development of PDMS aligner and SOP for alignment and sealing purpose of double PDMS layer.

CHAPTER 2: LITERATURE REVIEW

2.1 Physics of Multiphase Flows in Microfluidics

Understanding the fundamental of multiphase flow physics at microscale is essential to interpret the operation of microfluidic systems. In this section, the basic flow physics of the multiphase micro-droplets including the dimensionless parameters involved in flow characterisation will be discussed. The geometrical confinement and the system operation mechanism will be presented and discussed for better illustration in latter explanation of the experimental work. The droplets were generated in a confined micro-channel with multiphase flow, hence it is essential to understand the capillarity between the immiscible fluids.

2.1.1 Interfacial Tension, γ and Laplace Pressure

Capillarity studies the interfaces between two immiscible liquids. The interfaces are deformable and tend to minimise the surface energy by changing their shape. In condensed state, liquid is presented as molecules bonded by attractive electromagnetic forces.

$$\boldsymbol{\gamma = \frac{F}{L}} \qquad \textbf{Equation 1}$$

where F = force [mN]; L = length [m]

Interfacial tension, γ is the force that holds the surface of two phases together. Differ from a molecule in the middle of a bulk of liquid, the molecule at the interface expose half of its surface to a molecule of other fluid. This exposure decreases the cohesive interactions of the surface molecule causing imbalanced attraction force and hence induced the surface to contract and expose the smallest possible surface area. Hence, defining γ as the energy required to increase the surface area by one unit, expressed in

units of mN/m. Alternatively, γ can be defined as a force per unit length to describe the interfacial interaction between a liquid and a solid [32] (Equation 1).

When a liquid droplet is immersed into another immiscible fluid at stationary state, the pressure inside the droplet is different from the outside due to the presence of hydrostatic pressure across the interface caused by the surface tension. For example, if the oil is dispersed into the water in bulk, two immiscible phases can be observed. Due to the imbalance adhesion force explained previously, the oil will adopt to droplets resulted in O/W emulsion droplets when shake vigorously. Without addition of the surfactant, the liquid will return to its original state of two immiscible phases after some time. This is because the inner pressure of a smaller droplet is higher. Hence, the overpressure causes unstable thermodynamic leading to the Ostwald's ripening phenomenon. The displacement of the O/W interface requires work done by the pressure and capillary force. The increase of the hydrostatic pressure, Δp upon traversing the boundary can be described by the Young Laplace equation (Equation 2).

$$\Delta \boldsymbol{p} = \boldsymbol{\gamma} \left(\frac{\mathbf{1}}{\boldsymbol{R_1}} + \frac{\mathbf{1}}{\boldsymbol{R_2}} \right) \qquad \textbf{Equation 2}$$

where R_1 and R_2 = radii of curvature of the surface.

The interfacial tension between the two immiscible fluids can be measured with the pendant drop method. In this work, the interfacial tension of W/O emulsion droplet and O/W emulsion droplet was measured by a standard goniometer (250 – F1, ramé – hart instrumental co, Succasunna, NJ, USA) using the pendant drop and inverted pendant drop method. The pendant drop is a droplet suspended from a needle in a bulk liquid with a light bulb shape resulted from the relationship between the interfacial tension and gravity. As the droplet slowly detached from the needle, the shape of the droplet was traced by the DROPimage software to measure the necessary parameter such as dimension of

droplets according to the user-defined time step. The equilibrium state of the pendant drop can be described by Equation 3.

$$\gamma C = \rho g z \qquad \textbf{Equation 3}$$

where C = curvature of the droplet's surface, ρ = density of the droplet [g/m^3]

Since the hydrostatic pressure depends on the height, the curvature of the droplet interface changes in the vertical direction with time and eventually breaks loose when the weight exceeds the capillary force based on Tate's law. The degree of deviation is known as the ratio between the weight of the droplet and interfacial tension, and hence the interfacial tension can be calculated from the droplet shape if density difference of the immiscible phase is known.

2.1.2 Flow Parameter and Dimensionless Number

2.1.3 Superficial Velocity, v_{sp}

Superficial velocity, v_{sp} was calculated with the assumption of fully filled channel area by a specific fluid. In this work, the superficial velocity was calculated for the continuous phase of the PGHD since it directly affects the droplet formation/ encapsulation process using Equation 4.

$$v_{sp} = \frac{Q}{A} \qquad \textbf{Equation 4}$$

where Q = volumetric flow rate [m^3/s]; A = cross-sectional area [m^2].

2.1.4 Dimensionless Number

Conventionally in macro scale fluid system, Reynolds number (*Re*) was used as an important parameter to determine the importance of inertial force over the viscous force. However, when the fluid system was scaled down into a small micro scale fluid system,

Re is very small (*Re*<<1), it is meaningless to determine the flow condition. Instead, the interfacial tension between fluids become essential and hence, Capillary (*Ca*) number (Equation 5) was more applicable to determine the dominance of interfacial tension and viscous forces in a microfluidic system.

$$Ca = \frac{\mu \vartheta_{sp}}{\gamma} \qquad \textbf{Equation 5}$$

where ν_{sp} = superficial velocity of the continuous phase [m/s]; μ = viscosity of the continuous phase [kg/m.s]; γ = interfacial tension of the dispersed phase in the continuous phase [N/m]

Since both interfacial tension and fluid viscosity are important at micrometre scale, *Ca* become an essential dimensionless number to determine the dominance of either force according to the flow condition. At low *Ca*, the interfacial tension is stronger than the viscous stress and vice versa. Alternative to the comprehensive equation (Equation 5), *Ca* can be derived from the ratio of viscous stress to capillary stress, exemplified by a droplet. As a droplet with diameter, *d* in a shear flow over a distance *L*, with the speed changes from 0 to ν, the shear rate can be approximated by ν/L while the shear stress by $\mu\nu/L$. Combining with the Laplace pressured defined as $4\gamma/d$, the *Ca* can be redefined as $Ca = \frac{\mu \nu d}{4\gamma L}$ and used to assess the size of the droplets generated by shearing in bulk techniques [33](Figure 2-1). The determination of microfluidics flow regime by the *Ca* will be discussed in Section 2.1.6.

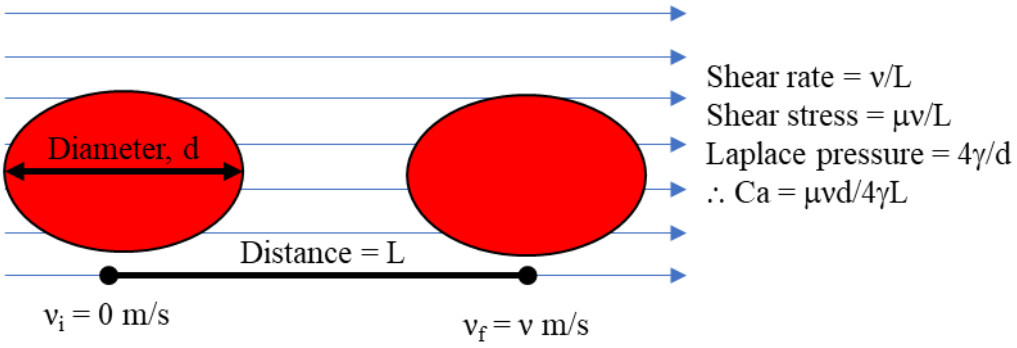

Figure 2-1. Schematic derivation for *Ca* = viscous stress/ capillary stress

In general, double emulsion droplets were generated under low flow rate value in which the regime is dominated by the viscous effects. However, some research groups [34, 35] apply a faster flow rate in their system to further characterise the fluid flow and droplet behaviour, hence requires Weber (*We*) number (Equation 6) to measure the relative importance of the fluid's inertial and interfacial forces.

$$We = \frac{\rho v^2 L}{\gamma} \qquad \textbf{Equation 6}$$

where ρ = fluid density [kg/m^3]; v = fluid velocity [m/s]; L = characteristic length of flow system [m]; γ = interfacial tension[N/m]

2.1.5 Coefficient of Variance (*CV*)

Coefficient of variance (*CV*) is an important parameter used to define the monodispersity of the droplets and can be calculated by Equation 7. The acceptance of monodispersity falls at 5% for normal particle size [36]. In terms of microfluidic, *CV* < 10% was accepted as monodisperse [27]. However, following the advancement of technology, certain research groups have been able to generate monodispersed double emulsion droplets with a *CV* range of 3-5% [18, 29, 36]. For example, Chu *et al.* [18] reported *CV* values for all their experiments were less than 2.3% and 1.6% for diameters of internal droplets and double emulsions droplets. On top of that, Abate and Weitz [29]

reported *CV* of 2% for double emulsions droplets while Takeuchi *et al.* [37] reported CV of 2.5% and 4.1% after polymerisation.

$$\boldsymbol{CV = \frac{\sigma}{\bar{x}} \times 100\%} \qquad \textbf{Equation 7}$$

where σ = standard deviation of the ranged data; $\bar{x}$ = mean of the ranged data.

2.1.6 Flow Regimes

The droplet generation processes can happen in different flow regime as reported by De Menech *et al.* [38] i.e. squeezing ($Ca_{crit} < 2\times10^{-3}$), dripping ($1\times10^{-2} < Ca_{crit} < 3\times10^{-1}$) and jetting ($Ca_{crit} > 3\times10^{-1}$). Since jetting regime occurs at higher flow rates, squeezing and dripping regime were more applicable and can be determined by both *Ca* and flow ratio, φ (Equation 8).

$$\boldsymbol{\varphi = \frac{Q_d}{Q_c}} \qquad \textbf{Equation 8}$$

where Q_d = volumetric flow rate of the dispersed phase [µL/min]; Q_c = volumetric flow rate of the continuous phase [µL/min]

Generally, *Ca* is the most important parameter to quantify the flow regime in micro-channels. In squeezing regime, the *Ca* value is very small ($Ca_{crit} < 2\times10^{-3}$). At this point, the breakup process in the squeezing regime is dominated by the build-up pressure in the upstream as an emerging dispersed phase blocks the main flow channel forming a plug at the junction corner. When the length of the emerging droplet is equivalent to the width of the main channel, the continuous fluid starts to squeeze the droplets forming a plug (Table 2-1). Both experimental and numerical studies [38, 39] show that the final droplet volume is a consequence of a two-stage droplet growth: (1) Droplet grows to a critical volume, V_c until the force exerted on the interface is balanced. (2) Droplets continues to grow for a time, t_n for necking due to the continuous injection of the dispersed phase. The

phenomenon above leads to the prediction of final droplet volume, *V* using the scaling law (Equation 9) [39]. Applicable to Equation 10 [40] as well.

$$\boldsymbol{V = V_c + t_n Q_d} \qquad \textbf{Equation 9}$$

where V = final droplet volume; V_c = critical volume; t_n = time for necking; Q_d = dispersed phase flow rate. Hence, V_c depends solely on *Ca* and t_n.

$$\boldsymbol{V = V_{c,ref} Ca^m + t_n Ca^n Q_d} \qquad \textbf{Equation 10}$$

where $V_{c,\,ref}$ and $t_{n,\,ref}$ = values at $Ca = 1$; t_n approaches 0; exponent m and n = -0.75 (depend on the device geometry)

While most of the experimental studies show the dominant force in squeezing regime is caused by the pressure built-up, Garstecki *et al.*[41] suggested the detachment begins when the emerged droplet fills the main channel and continues to grow due to the continuous injection of the dispersed phase. Assuming the squeezing rate is proportional to the average velocity of the continuous phase and plug fills at a rate proportional to Q_d, the length of the droplet can be defined by Equation 11 [42].

$$\boldsymbol{\frac{L}{w_c} = 1 + \alpha\left(\frac{Q_d}{Q_c}\right)} \qquad \textbf{Equation 11}$$

where L = length of the droplet; w_c = channel width; α = fitting parameter of order one

The scaling law shows that droplets generation under the squeezing regime will always have a longer droplet length than the channel width and is solely dependent to the flow ratio, φ. Therefore, the droplet size increases with an increase in φ, resulted a comparable larger droplet size compared to dripping regime. This effect slowly diminishes as the *Ca* increases and transitioned to dripping regime. Liu and Zhang [43] on the other hand suggested that droplet size strongly depends on *Ca* in squeezing regime, consistent to

their experimental observations. This verified Equation 11 in predicting the droplet size with various flow rate ratios when *Ca* is fixed at squeezing regime. Equation 10 should be used when *Ca* is manipulated.

At the dripping regime ($1\times10^{-2} < Ca_{crit} < 3\times10^{-1}$), the dispersed phase experience shear force from the continuous fluid when it first emerged into the main channel and the pressure force build-up due to the partial blockage of the main channel. The detachment point of the droplet occurs at the downstream of the main channel. The effect of the φ is no longer significant as compared to the squeezing regime. However, the detachment point gradually moves downstream until a stable jet is formed as the φ increases. Droplet size is inversely proportional to *Ca*, forming smaller droplets in this regime. Jetting regime occurs at high flow rates of continuous and dispersed phase, hence the droplets are generated due to the natural growth of interfacial instability and the viscous forces exerted by the continuous phase fluid [44]. This resulted in small and spherical droplets.

Besides the three common flow regimes: squeezing, dripping and jetting, Xu *et. al*. [45] proposed a transient regime ($2\times10^{-3} < Ca_{crit} < 1\times10^{-2}$) which falls between squeezing and dripping regime. According to their studies, the droplet size of the flow regime can be summarised such that at (1) squeezing regime, the length of dispersed droplet, l is larger than 2 times of the channel width, w ($l > 2w$); (2) dripping regime, ($l < w$) and (3) transient regime, ($w < l < 2w$). This is because, at transient regime, the droplets break-up dynamics is dominated by both the pressure built-up (squeezing regime dominance force) and shear and interfacial forces (dripping regime dominance force). Their assumption on the plug length in transient regime can be presented by Equation 12.

$$\frac{l}{w} - \varepsilon = k\left(\frac{Q_d}{Q_c}\right)^{\alpha}\left(\frac{1}{Ca_c}\right)^{\beta} \qquad \textbf{Equation 12}$$

where ε and k = fitting parameters, α and β = ratio of the squeezing and dripping mechanisms

The model was fit with their previous experimental data and extended to Equation 13 (T-junction geometry [46]–[48]) and Equation 14 (cross-junction geometry [49]) respectively.

$$\frac{l}{w} = 0.75\left(\frac{Q_d}{Q_c}\right)^{\frac{1}{3}}\left(\frac{1}{Ca_c}\right)^{\frac{1}{5}} \qquad \textbf{Equation 13}$$

$$\frac{l}{w} = 1.59\left(\frac{Q_d}{Q_c}\right)^{\frac{1}{5}}\left(\frac{1}{Ca_c}\right)^{\frac{1}{5}} \qquad \textbf{Equation 14}$$

Where $Ca_c = Ca$ of continuous phase

The extended model shows accurate approximation on the droplet size in transient regime. However, the fitting parameters and mechanism ratio is highly dependable on the channel geometry, wetting properties and working system. Hence, pose limitations and require improvement by taking the channel geometry and wetting properties into consideration. The characteristics of the flow regime is summarised in Table 2-1.

Table 2-1. Summary of Flow Regime

Flow Regime	*Ca* range	Droplet break-up dominance force	Droplet Size
Squeezing	$Ca_{crit} < 2\times10^{-3}$	Pressure built-up from the upstream main channel.	$l > 2w$
Transient	$2\times10^{-3} < Ca_{crit} < 1\times10^{-2}$	Pressure built-up and shear force exerted by continuous phase.	$w < l < 2w$
Dripping	$1\times10^{-2} < Ca_{crit} < 3\times10^{-1}$	Shear force exerted by continuous phase.	$l < w$
Jetting	$3\times10^{-1} < Ca_{crit}$	Rayleigh-Plateau Instability [50] and viscous force exerted by the continuous phase [44].	equivalent to diameter of liquid thread, d
Squeezing	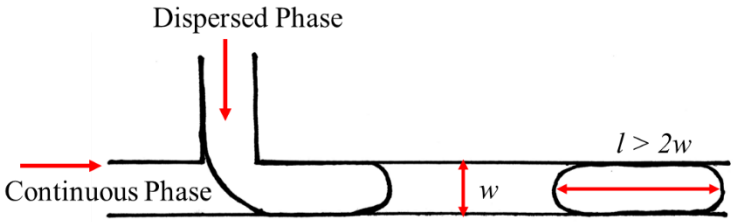		
Transient	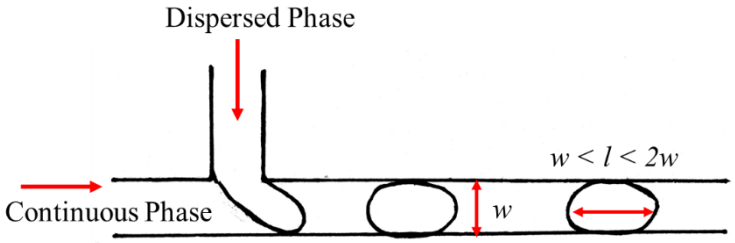		
Dripping	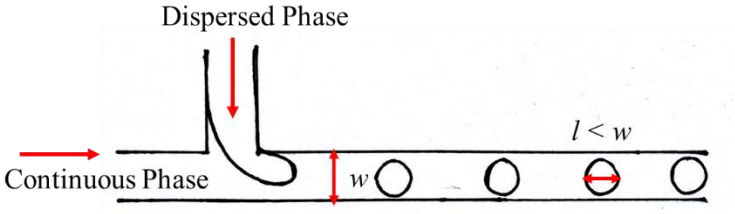		
Jetting	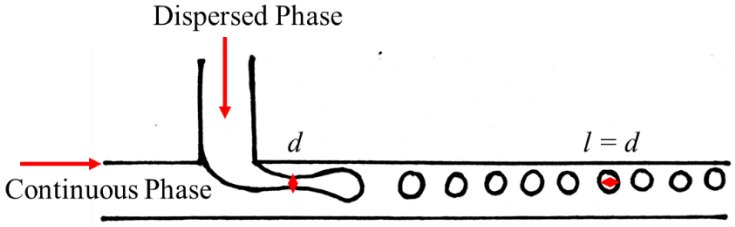		

2.2 Materials and Microfabrication Technique

Development of microfluidic devices originated from photolithography and the associated technology i.e. integrated circuit (IC) fabrication technique, well established in the micro-electromechanical systems (MEMS) manufacturing sector where silicon was used as the base substrate material [51]. Examples of the application for MEMS are micro-sensors, actuators and control functions [52]. Microfluidic technology falls under the branch of MEMS, handling fluids in microliters environments. Microfluidic technology realised a vast range of miniaturised analytical devices, commonly associated with lab-on-chip (LOC) systems or micro-total-analysis system (μTAS), providing platforms for various biomedical, biochemical and chemical analytical applications. The well-established silicon processing lead to the rapid evolution of microfluidic technologies, however, its optically opaque limited the applications. Hence, glass and polymeric materials [53], [54] such as polymethylmenthacrylate (PMMA), polystyrene (PS) and PDMS have been used to fabricate the microfluidic device.

In this section, the microfabrication techniques including the materials used will be briefly introduced. Comparison work will be carried out for Xurography technique since it is the technique used in this research work.

2.2.1 Standard Photolithography

The first analytical miniaturised device, gas chromatographic analyser, fabricated on a silicon wafer was presented in the 1970s [55]. However, most of the methods used in μTAS manufacturing were only developed between the 70s – 80s in the silicon microprocessors industry. This emergence of microfabrication technologies led to the first-generation of microfluidic chips prepared by silica or glass [56, 57] under the standard photolithography technique, then polymeric materials in the microfluidic sector.

The fabrication process for silicon-based microfluidic devices involve substrate cleaning, photolithography, metal deposition and wet/ dry etching [58, 59].

Photolithography (Figure 2-2) is one of the steps in fabrication used to transfer a pattern from a photo mask to the light-sensitive chemical photo resist applied on the silicon wafer via the exposure to ultraviolet (UV) light. The photoresist was developed to generate a mask for etching and removed by a developer solution i.e. propylene-glycol-mono-methyl-ether-acetate (PGMEA). The micro-channels were then sealed with a flat substrate through a fusion bonding process [60]. In terms of materials, both glass and silicon are resistant to organic solvents, possess high thermal conductivity, electroosmotic mobility, and solvent compatible leading to advantage in different applications.

The major application of glass chips is capillary electrophoresis with other important applications such as on-chip reactions [61], droplet formation [62], solvent extraction and in situ fabrication [61]. However, the hardness of the materials limit their application in microfluidics. On top of that, glass chip device involves high fabrication cost and hazardous chemicals i.e. hydrogen fluoride. The bonding of the substrates is also difficult as it requires high temperature and pressure under clean environment.

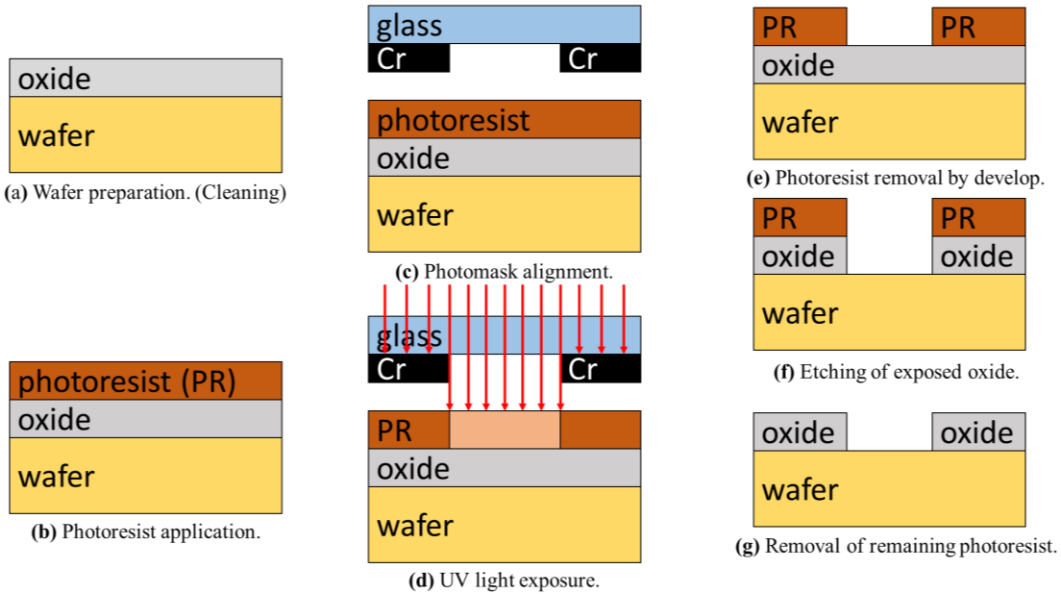

Figure 2-2. Schematic diagram of Photolithography process by developer

2.2.2 Soft Lithography

The development of rapid prototyping enables a shorter fabrication cycle and hence expanded and established in microfluidic field [63]. Soft lithography enables facile reproduction utilising the master mould to fabricate both two-dimensional (2D) elastomeric channels and three-dimensional (3D) microfluidic systems via crossing channels [64] and membrane sandwich [65]. Once the master mould was fabricated via photolithography method, an elastomeric organic polymer such as PDMS is casted onto the master mould to transfer the pattern through moulding or printing. The flexibility of the PDMS replicas allow patterning on non-planar structures through micro-moulding [66] or micro-contact printing [67].

Although the molecular structure of PDMS resulted in organic solvents incompatibility restricting its chemical applications. PDMS is still known as the most popular elastomer in microfluidics [68, 69] due to its gas permeability, enabling long-term cell culture in sealed micro-channels and provides a well-controllable micro-environment. In contrast to glass and silica, PDMS microfluidic devices are [70]–[72] templates and its low surface tension (19-21 mN/m) [73] facilitates the peeling from

templates once cured. The sealing of PDMS to other substrates can be done both reversible and irreversible [74] providing additional advantages.

2.2.3 Xurography

Comparing to the existing masking technologies for glass etching, Xurography is known as the fastest technique as it involves fewest step and does not require rigorous cleaning procedure. Xurography, a fabrication technique that create microstructures with the conventional cutting plotter was first introduced by Bartholomeusz *et al.* [75]. The cutting plotter is a tool, often used in the graphic art industry to cut designs on the adhesive backed films for large retail sign. After the design was plotted, the undesired film will be weeded, leaving the desired part transferred to a substrate using application tape (Figure 2-3). Cutting plotter FC5100A-75 from Graphtec with addressable resolution of 10 µm was used to present patterning on various film materials where the conventional only up to 25 µm. The optimal material dependent settings and the minimum feature sizes for each material were obtained.

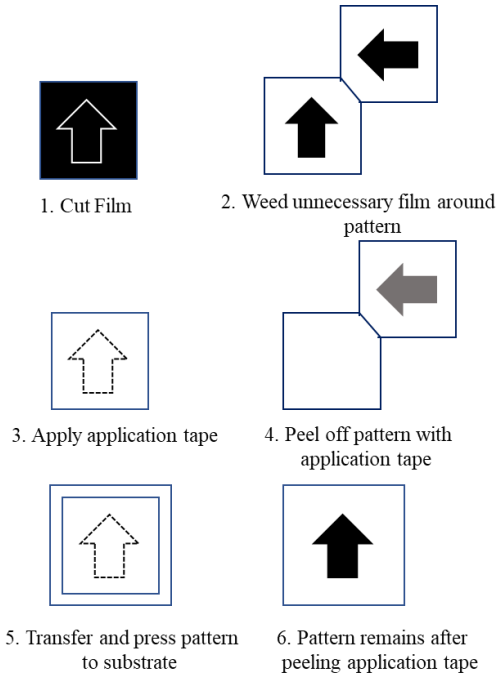

Figure 2-3. Schematic illustration of the pattern transfer procedure. (Redrawn for illustration)

To achieve the highest resolution, the plotter was set to function at its slowest speed and acceleration. Their findings show feature size is limited by tension in the material, blade sharpness, cutting speed and material properties such as Young's modulus and Poisson's ratio [76]–[78]. Mechanics study of slitting polymer films show normal stress, σ_{xx} is greatest when near to the edge of blade and resisted by the shear stress, τ_{yx} at the interface of the film's adhesive and release liner. Hence, thinner, softer material with low Poisson's ratio and high yield shear stress, $\tau_{yx\text{-}max}$ enables production of smaller features. Bartholomeusz *et al*. demonstrated poor accuracy in microchannel below 150 µm, with an average of 20% error from the targeted dimension. Further study by Bartholomeusz *et al.* shows feasibility of Xurography in applications such as shadow mask, electroplating, micro-moulding in PDMS and laminated microfluidic structures in 2D and 3D.

Following to the method developed by Bartholomeusz *et al.*[75], Yuen and Gloral [79] demonstrated the Xurographic technique with a desktop digital craft cutter from QuicKutz to plot their design onto a 50 µm thick double-sided pressure sensitive adhesive (PSA) tape. To further investigate the cutting quality and limitation of the craft cutter, they have designed a serpentine microchannel width ranging from 200 µm to 700 µm. Findings showed that the craft cutter has a better resolution in the horizontal cutting direction, whereas cut quality is better in the vertical cutting direction. They also showed consistent cutting of the craft cutter at the same location for 200 µm micro-channels. This finding is important as until current, most of the reports still show inconsistent cutting with the decrement of channel width. Yuen and Gloral [79] reported the key to high-quality clean cut for small features i.e. 200 µm, is the removal of the top plastic protective layer before the PSA layer to avoid the picking up of the cut PSA debris by the blade. From then, various studies and applications have been demonstrated by different research groups summarised in Table 2-2.

Overall, Xurography technique has been reported as a rapid and low-cost fabrication versatile to different materials and applications as mentioned above. Most of the reported work claimed reduction in cutting accuracy as micro-channel width reduced, however, the relatively low resolution was still reliable in most of the applications.

Table 2-2. Summary of Xurography technique done by various research group

Research Group	Cutter Plotter (Model)	Plotting Media (thickness)	Microchannel Design (Device Materials)	Plotter findings	Applications
Do *et al.*[80]	Graphtec cutter plotter (CE5000-40-CRP)	Cyclic olefin polymer (COP) sheet (1mm)	5mm single line to test cutting force; Serpentine and cross-junction geometry (3D COP)	Both channel width and written depth increases linearly with the cutting force.	Bubble free filling microfluidic chamber; Chaotic micromixer; Disposable capillary electrophoresis chip
Javier *et al.*[81]	Graphtec plotter razor cutter (FC800)	PS films (100 µm) and mylar films (200 µm) with double sided tape (40 µm) as adhesive layers	Y-junction geometry (PS sealed on glass slide)	N/A	Dynamic cell assays purposed diffusion-based gradient generator
Santana *et al.*[82]	Roland cutting plotter (GX-24) Resolution: 100 µm	3M Scotchcal D3000 vinyl adhesives (0.99mm)	Cross-junction geometry (Glass – wet etching)	1. Produced square shape structures with 106±8 mm in width. 2. Plotted width > designed width (standard deviation = 7.8, 3.4 and 4.7% for width 106, 165 and 219 µm respectively) 3. High linearity (R^2=0.998) indicates high precision plotting	Electrophoresis

Islam *et al.*[83]	Graphtec cutter plotter (CE6000-40)	Double sided pressure-sensitive adhesive (PSA) film comprised of polyester (PET) film (127 µm)	Straight, curved, square serpentines and zigzag channel. (Acrylic)	1. Cut accuracy is independent to the blade angle (30° and 45°) when channel width > 700 µm. 2. 30° blade shows better performance for channel width < 700 µm. 3. Percentage error for 200 µm width decreases from 26.5% to 9.09% using 30° blade. 4. Plotter gained more controlled movement providing better resolution at horizontal direction. (Consistent with Ref [79])	Microfluidic gradient generator
Pinto *et al.*[84]	GCC cutting plotter (Jaguar II)	Adhesive paper (100 µm)	Diverging and converging bifurcation channel and flow-focusing geometry (PDMS)	1. Minimum dimension of channel width = 150 µm limited by Xurography. 2. Percentage error of approximately 3, 5 and 10% for channel width 200, 300 and 500 µm.	Biomedical microfluidic devices for blood flow analysis
Cosson *et al.*[85]	Graphtec cutter plotter (CE5000-40-CRP)	PDMS layer on double-sided adhesive (100 µm)	Serpentine channel (PDMS)	1. Cutting resolution was affected by the PDMS curing ratio: structures of 100 µm were reliable at 5:1 curing ratio and damaged at 10: 1 curing ratio. 2. Cutting accuracy decreased significantly with smaller feature size. 3. Channel width below 100 µm could not be cut.	Cell culture

2.2.4 Glass Capillary (GC)

The fabrication technique of assembling the glass capillary tube on a glass plate was first introduced in 2005 by Utada *et al.* [9] to generate and encapsulate the droplets specifically. The device was prepared by tapering the cylindrical glass capillary to the desired diameters by a micro-pipette puller and a micro-forge. The tapered glass capillary tube was nested within a square glass tube with same inner diameter as the outer diameter of the cylindrical glass capillary tube. This was to achieve good alignment between the glass capillary tubes to form a coaxial geometry. The capillary tubes were sealed with transparent epoxy resin and fixed onto a glass plate. Once the microfluidic device was assembled, the innermost fluid was pumped through the tapered cylindrical capillary tube while the middle fluid was pumped through the outer coaxial region to form a coaxial flow at the exit of the tapered tube. The outermost fluid was pumped from the opposite direction (counter-current) to force the fluids and droplets to the exit orifice. The outer fluid can also be pumped co-currently to the scaled microfluidic device.

Glass capillary tube microfluidic device has been well established [22, 86], with advantages such as chemically inert to organic solvent and easy modification on surface wettability. The droplets encapsulation can be controlled and structured easily by simply modifying the number of inner tube. However, glass capillary tube microfluidic device required high capital cost to start with and the complex fabrication process which require manual operation limited its mass productivity. Hence, researchers continue to search for simple and rapid micro-fabrication techniques.

2.2.5 Short Summary

Historically, the microfluidics work was inspired by the semiconductor industry and hence the first generation of microfluidic device were fabricated by glass or silicon with wet or dry etching method [59]. Standard photolithography technique was used to make the masks to allow glass or silica etching. Soft lithography technique took place later to replace the silica and glass with elastomer, specifically PDMS [63]. The technique allows easy replicates of microfluidic device with master mould. Xurography technique was later introduced as an alternative rapid prototyping method. Although this technique has a relatively lower resolution than the standard lithography method, it enabled a vast range of applications as reported, accessible to most of the novice research group in microfluidic. Glass capillary tube microfluidic device aroused in 2005 then established until recent. The advantages and disadvantages of each devices are summarised in Table 2-3 below.

Table 2-3. Summary of Microfabrication Technique

Fabrication Technique	Device Material	Equipment and Materials	Advantages	Disadvantages
Standard Photo-lithography	Glass and Silicon	Silicon wafer, photoresist, spin coater, UV light source	1. Enable etching of integrated circuit with single beam of UV light. 2. Produce controlled size and shape of entire substrate	1. Requires clean room facility. 2. Requires completely flat substrate when patterning [87]
Soft Lithography	Soft polymer eg. PMMA, PS, PDMS	Silicon wafer, photoresist, spin coater, UV light source	1. Comparable low cost to photolithography. 2. Can be applied on both planar and non-planar surfaces. 3. High resolution.	1. Requires clean room facility. 2. Channel depth depends on UV light exposure. 3. Expensive equipment compare to Xurography
Xurography	PDMS, acrylic, glass	Cutter plotter, vinyl film	1. Lowest cost among all techniques. 2. Requires only commercial equipment. 3. Does not require special skill to operate. 4. Enable constant channel depth	1. Comparable low resolution. 2. Inconsistent cutting quality at small channel width.
Glass Capillary	Glass capillary	Micro-forge, micro-puller	1. Highly scalable to form multiple emulsions droplets. 2. Enable controllable droplets structure by manipulating number of capillary tubes.	1. Requires clean room facility. 2. Requires expensive equipment. 3. Labour intensive and not suitable for mass production.

2.3 Overview of Microfluidic Systems

In general, elastomeric microfluidic devices, utilised T-junction [13, 88]–[90] and flow-focusing [2, 91]–[93] geometry for droplet generation [92, 93] and encapsulation [29, 37, 95]. Alternative to PDMS microfluidic device, glass capillary microfluidic device introduced coaxial flow, enabling droplets generation and encapsulation through co-current or counter-current flow. Microfluidic devices varied from patterning coverslips on microscopic glass piece [30], insertion of needles into plastic tubing [95] and 3D printed micro-capillary design [96] offering simple and versatile fabrication technique. The development of the singled-material and hybrid microfluidic system will be reviewed in this section. The injection of immiscible fluid into the microfluidic device was done independently according to their wetting properties, i.e. hydrophobic and hydrophilic leading to the necessity of surface treatment for certain devices. Therefore, the surface treatment method will also be discussed briefly and with detail in the sub-section. The droplets were mostly characterised by the diameter size and the *CV* value.

In 2004, Okushima *et al.* [27] introduced a novel method for preparation of monodisperse double emulsion droplets using a two-step method of droplet formation in a cascading T-junction geometry (Figure 2-4a). They proposed two configurations i.e. one-chip type with hydrophobic and hydrophilic junction on the same chip and two-chip type with junctions on separate chips. The single-chip channel was made on Pyrex glass by repeated isotropic etching with junction treated with silane-coupling agent for hydrophobic modification. The two-chip modules were fabricated on quartz glass using machining tools and Pyrex glass by isotropic etching. The diameter of the W/O/W double emulsion droplets formed at the one-chip module were 83 μm (*CV* = 2.7%). The two-chip module, on the other hand, produce monodisperse W/O/W droplets with *CV* below 7%, however, the inner droplets ruptured when flowing from the first chip to the second chip.

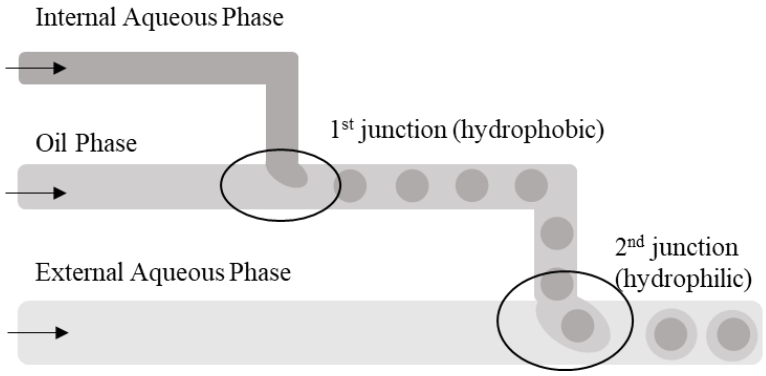

Figure 2-4. Two-steps method using cascade T-junctions to prepare W/O/W double emulsion. (Redrawn for illustration)

Okushima *et al.* further demonstrated different type of double emulsion droplets by changing the wetting and geometrical properties of the micro-channels. Hence, concluding the one-chip concept is useful when precise control of encapsulation is required while two-chip approach provides greater flexibility in generating diverse double emulsion droplets.

In the same year, Zheng *et al.*[97] presented a hybrid microfluidic device coupling glass capillary with PDMS micro-channels to allow long-term storage of the generated droplets. The droplets were generated in the PDMS micro-channels then transported into the capillary tube connected at the outlet of the PDMS micro-channel. The flow was stopped when the capillary was filled with the droplets of desired composition, then disconnected and sealed with wax for long-term storage. The captured droplets then undergo micro-batch and vapour diffusion techniques for protein crystallization.

In 2005, Takeuchi *et al.* [37] described a microfluidic axisymmetric flow-focusing device (AFFD) that produces Nylon-coated micro-capsules with comparatively narrow size distribution i.e. CV<5%. The AFFD confined droplets in the central axis of a microfluidic channel to protect the droplets from shear caused by the adhesion to outlet channel walls. This characteristic avoids the usual drawbacks in preparing polymer-coated micro-capsules, i.e. contact of discontinuous phase with channel wall and leaking

at the interface between PDMS layers under high flow rates and pressures [74]. Takeuchi *et al.* reported on the limitations in eliminating the surface wetting problems due to the chemical inhibition, hence difficulty in choosing surfactants. Besides, silanization can only provide a temporary surface treatment.

Hence, the wetting properties was solved geometrically by ensuring complete shield of inner aqueous phase from the channel wall by the continuous phase. The fabrication of AFFD involves a whole piece of PDMS with optical fibres serves as the master to produce seamless channel. Two glass capillaries were inserted as the inlet for dispersed phase and outlet for the droplets. The inlet continuous phase was formed by drilling holes into the channel and connected with polyethylene (PE) tubing. The configuration of AFFD is similar to the glass capillary microfluidic device (discussed in next paragraph) except the channel confinement throughout the whole device.

Glass capillary microfluidic device first advent in 2005, introduced by Utada *et al.* [9] to generate monodispersed double emulsion droplets in a single step while precisely control the outer and inner droplet size as well as the number of encapsulated droplets. Using the capillary device, they managed to produce a stream of double emulsions containing a single internal droplet. The thickness of the shell can be controlled to form extremely thin shells with the ratio of shell thickness to outer droplet radius as low as 3% or increase to 40% producing a thicker shell. On top of that, they produced double emulsions with various number and size of the internal droplets. Since the fluid was no longer suppressed by the device dimension, the inner fluid is completely shielded from the outer fluid allowing the dispersed phase to flow in either hydrophilic or hydrophobic fluids without the necessity of surface modification. However, the droplet formation

frequency is limited to 100 – 5000 Hz and requires operation of parallel device to increase the production rate.

Chu *et al.* [18] reported a similar technique but with higher scalability by introducing a transition tube between the injection tube and collection tube to produce a two-step emulsification. In both emulsification steps, droplets formed immediately at the exit of the tapered capillary indicating the dripping mechanism. This separation of two-step emulsification allows precise control on the number of innermost droplets by adjusting the device dimension and the inner, middle and outer fluid flow rates. Their experiments show monodispersed internal droplets and double emulsion droplets with *CV* value less than 2.3 and 1.6% respectively. The coaxial structure of the capillary microfluidic device enables the use of same device for W/O/W and O/W/O double emulsion droplets without surface modification on the wettability. The introduced technique allows easy extension on the microfluidic device to generate hierarchical level of multiple emulsion droplets i.e. triple emulsions by increasing the number of transition tube. Large deformation of droplets, however, was reported as the droplets flow through the tapered regions of the capillaries.

Abate and Weitz [29] presented a simple PDMS microfluidic system to create hierarchical level multiple emulsion droplet useful in synthesizing particles with structured interiors. They utilised linear arrays of pinned-jet flow focusing (PJFF) geometry with alternating wettability to stabilise the droplet formation, particularly at low flow rates, enabling the generation of monodispersed droplets. The wetting properties of the channel wall was spatially controlled by the coating of photo-reactive sol-gel and heated to make the channel hydrophobic by default. The hydrophilic polyacrylic acid (PAA) was then grafted onto desired junction by ultraviolet (UV) light-initiated

polymerisation. Using this system, the size distribution of the droplets generated were well maintained at $CV < 2\%$.

Thiele *et al.* [98] reported the fabrication of polymersomes, a type of artificial vesicles, using double emulsion droplets in glass-coated PDMS microfluidic device. Typical formation of polymersomes rely on the undirected self-assembly of the copolymers leading to broad size distributions and low encapsulation efficiency [99]–[101]. Using double emulsion droplets as template, the assembly of the copolymers were directed during the evaporation of the organic solvent in which the copolymer is dissolved, providing additional control over the interactions between the block copolymers. To avoid disruption of the droplets generation, the ability to inject additional solvents during the operation is desired to allow in-situ removal of copolymer precipitates. This limited the usage of glass capillary microfluidic device due to the non-customisable channel design, instead, the flexible PDMS microfluidic device is more suitable. However, PDMS is well known with its low chemical resistance and swells upon contacting the organic solvents. Hence, in this study, they coated the PDMS device with a sol-gel to produce a durable glasslike layer tailoring the surface properties and increased the resistance of the channel walls.

The microfluidic device forms double emulsion templates of approximately 100-150 µm diameter with polymersome diameter ranging from 50-100 µm. The development of this microfluidic device shows feasible application of stamped microfluidic device involving chemical solvent and allows mass production. The performance of the sol-gel coated microfluidic device was then compared with the conventional microfluidic device. Results showed that sol-gel coated microfluidic device formed diblock copolymer-stabilised W/O/W double emulsion droplets. To maintain the stability, the osmolarity of

the inner and outer phase was balanced by the addition of glucose and polyvinyl alcohol (PVA). The non-Newtonian nature of the PVA solution developed a tail at the middle phase connecting the double emulsion droplets at the initial phase. On the other hand, conventional microfluidic device formed deblock polymer stabilised W/O/W double emulsion droplets from premixed chloroform and toluene. As the chloroform starts to evaporate, the diblock polymer forms precipitates fouling the device and lead to unstable interfaces at the shell of the double emulsion droplets.

In 2011, Wang *et al.* [86] described a hierarchical and scalable microfluidic device made from three basic building blocks, i.e. drop maker, connector and liquid extractor. The microfluidic device allows easy generation of multiple emulsion droplets with precise control on number, ratio and size of the co-encapsulated droplets at each level utilising similar concept from Chu *et al.* but more compact. The extended microfluidic device allowed controlled production of sextuple-component triple emulsions with different structures, and droplet size. The diameter of the inner droplets was maintained in the range of 160-170 μm while the diameter of double emulsion droplets was reported approximately 350-380 μm according to different flow rate ratio.

Since then, different microfluidic devices with the simple and low-cost fabrication method have been developed. Deng *et al.* [30] proposed a microfluidic device fabricated with patterned coverslips and microscope glass slides with the aid of glass cutter. The glass slides were cleaned with piranha solution for an hour before bonded onto a glass slide with a UV-curable adhesive. The channel was confined with a new cover slip on top leaving the inlets and outlets connected to the syringe needle by epoxy resin. The surface wettability properties are spatially modified by self-assembled monolayer (SAM) chemistry and flow confinement methods which involved aqueous solution of HF or

NaOH. The mean diameter of the droplet produced is 228.2 μm with *CV* of 0.86%. The author, however, did not disclosed on the cutting control and alignment precision of the coverslips.

Nurumbetov *et al*. [102] later demonstrated a simpler and straight forward system to generate the double emulsion droplets and polymer microcapsules with only syringe needle, polyvinyl chloride (PVC) tubing, two glass capillaries and epoxy glue involved. The material mentioned was used to construct a co-flow and "obstructed" T-junction. The device was used to fabricate polymer capsules with poly (isobornyl acrylate) acts as the shell structure. The droplet size produced maintain within a range of 280-420 μm as a function of penetration depth of the capillary tip into the glass tube. In 2016, Li *et al.* [95] introduced as 3D integrated needle-based microfluidic devices. The device was assembled using readily available component such as stainless-steel dispensing needles, polypropylene (PP) male luer fittings, transparent PP cross-links, transparent PP tee-links, transparent PE tubing and transparent silicone tubing. The droplet size was controllable by changing the size of the dispensing needle. The experimental work reported the diameter of the droplets using different needle gauge i.e. 20-18G, 23-19G, 27-22G and 34-30G as 824.23 μm (*CV* = 2.74%), 747.34 μm (*CV* = 0.71%), 387.07 μm (*CV* = 1.80%) and 86.47 μm (*CV* = 1.24%).

Morgan *et al.* [96] presented simple 3D printed microfluidic devices with polylactic acid (PLA) filament using flow-focusing junction. The modules are connected by interlocking the rounded studs of the male block into the female blocks without any form of adhesion required. Droplets with consistent diameter of 504 μm ± 18 μm were produced within a frequency range of 1-10.4 Hz. Li *et al.* [103] proposed a local modification method to make the hydrophilic PMMA microfluidic devices hydrophobic

at the desired location for the double emulsion droplet generation. The liquid PDMS filled and displaced at the desired microchannel location using air stream to coat a thin layer of PDMS onto the channel wall. The modified PMMA device with double cross-junctions was used to generate the monodisperse W/O/W double emulsion droplets. The average diameter of the inner droplet is 258.7 μm with *CV* value 1.9% whereas the double emulsion droplets is 417.5 μm with *CV* value of 1.0%.

Review showed that researcher never cease to discover or modify new fabrication method to generate the double emulsion droplets suitable to the desired applications. The different microfluidic devices with their applications are summarised at the Table 2-4 below for better illustration.

Table 2-4. Summary of the microfluidic device system reported by various research group.

(The droplet size and *CV* value only included double emulsion droplets. W/O emulsion were noted as not applicable (N/A))

Device Material		**Double emulsion droplet size [μm]; *CV* [%]**	**Surfactants (lipophilic; hydrophilic)**	**Flow rate [μL/hr] (inner: middle: outer)**	**Surface treatment method**	**Research Group**	**Applications**
Polymer-based	PDMS	65; 2	used but not mentioned	200: 400: 600	photoreactive sol-gel coating with UV polymerization	Abate and Weitz (2009)	synthesizing particles with structured interiors
	PLA filament	N/A	NR	100: 300	N/A	Morgan *et al.* (2016)	stem cell encapsulation
	PMMA	417.5; 1	used but not mentioned	60: 120: 300	PDMS coating	Li *et al.* (2018)	cell culture and analysis
	glass coated PDMS	100-150; NR	NR	300: 1000: 500: 3500	photoreactive sol-gel; graft patches of hydrophilic PAA with spatially patterned UV light	Thiele *et al.* (2010)	polymersomes
Glass-based	Pyrex glass with quartz glass	83.4; 2.8	lecithin; sodium dodecyl sulfate (SDS)	5: 20: 1400	silane-coupling agent	Okushima *et al.* (2004)	analysis of confined chemical reactions
	Microscope glass slides and coverslips	250-450; 0.86	polyglycerol polyricinoleate (PGPR 90); Pluronic F-127	300: 500: 800-12000	SAM chemistry and flow confinement method	Deng *et al.* (2011)	microreactor

Device Material		Double emulsion droplet size [μm]; *CV* [%]	Surfactants (lipophilic; hydrophilic)	Flow rate [μL/hr] (inner: middle: outer)	Surface treatment method	Research Group	Applications
GC-based	glass capillary	52.5-500; NR	N/A	800: 200: 2500	coaxial geometry	Utada *et al.* (2005)	polymerosomes/ polymer vesicles
	glass capillary	approx. 246; 1.6	NR	350: 2000: 5000	coaxial geometry	Chu *et al.* (2007)	pharmaceuticals, drugs delivery
Hybrid	PDMS + glass capillary	N/A	Not Reported (NR)	NR	N/A	Zheng *et al.* (2004)	protein crystallization
	PDMS + optical fibre and glass capillary	153; 2.5 (before polymerisation) 168; 4.1 (after polymerisation)	Span-80; NR	100-500: 1000-2000: 10,000-20,000	3D geometry	Takeuchi *et al.* (2005)	nylon-coated microcapsules with superparamagnetic particles encapsulated
Tubing assembled	PVC tube + glass capillary	282-418; NR	NR; polyvinyl alcohol (PVA) solution	NR	"obstructed" T-junction by modifying needle placement	Nurumbetov *et al.* (2012)	polymer microcapsules
	stainless steel dispensing needle + fittings	86.47-824.23; 0.71-2.74	NR; Pluronic F108	60: 360: 10800	immersion in octadecyltrichlorosilane (OTS) solution	Li *et al.* (2016)	N/A
	drop maker building blocks	350-380; NR	NR	NR	coaxial geometry	Wang *et al.* (2011)	N/A

2.3.1 Surface Modification Technique

Regardless of the device material used, the type of droplets produced were determined by the wetting property of the channel wall. Therefore, surface modification is required to produce higher degree emulsions i.e. double emulsions and triple emulsions. Various surface modification techniques have been introduced during the heyday of PDMS microfluidic devices. Some of the technique such as oxygen plasma treatment and sol-gel glass coating method have been used until present. Oxygen plasma treatment utilised ionised oxygen to functionalise the outer surface of PDMS and is known as the most efficient modification method due to its short treatment time and easy operation [25]. However, plasma treated PDMS surface also undergo hydrophobic recovery within a very short timeframe i.e. few minutes [104]. Therefore, plasma treatment is often used by the researchers as a method to bond and seal the PDMS layers instead [29, 98].

Sol-gel coating, on the other hand, is a polymerisation process based on the phase transition of a liquid state [105]. This method has been utilised by several research groups as reported previously [29, 98]. To spatially pattern the wettability, the microfluidic device was first coated with a photoreactive sol-gel [106]. The sol-gel is intrinsically hydrophobic but can be made hydrophilic with the help of photolithographic techniques. Patches of hydrophilic PAA was then grafted onto the interface by filling the coated channels with PAA monomer solution and polymerised with UV light exposure. The polymerisation process was initiated by the photoinitiator silanes embedded in the sol-gel which released radicals under the exposure of UV lighting. Apart from surface modification, this coating method allows the transformation of low chemical resistant PDMS into a chemically inert microfluidic device as demonstrated by Thiele *et al.*[98].

The conventional technique used to modify the polymer surface mentioned above requires extra usage of chemicals and equipment while adding extra fabrication steps prolonged the duration. The researchers later utilised the advantages of the geometry design to replace the surface modification method. Such geometry was first introduced by Takeuchi *et al.* then adapted into the glass capillary microfluidic device by several groups as reported in Table 2-4. In 2012, Rotem *et al.* [94] introduced a non-planar device which utilised the difference in height dimension to remove the wettability constraints imposed by the planar geometry and demonstrated the geometry on device fabricated from PDMS and Apex glass respectively. However, in their report, the PDMS and glass devices were still treated with both oxygen plasma and coated with silane solution respectively to render more hydrophilic and hydrophobic.

In short, wetting properties of the device material is essential and unavoidable when multiphase droplets formation is involved. Various surface modification technique from using specific geometry design, chemical coating to physical deposition have been reported. The conventional surface treatment technique requires expensive chemicals and additional equipment with complicated spatially patterning and temporary effect. On the other hand, hybrid microfluidic device has been introduced for other application such as removal and storage of output particles but never for surface modification purpose. Utilising the intrinsic surface properties of the different materials, the potential of the hybrid microfluidic device can be further explored.

CHAPTER 3: DESIGN AND FABRICATION OF HYBRID MICROFLUIDIC DEVICES

3.1 Initial Inspiration of the Hybrid Microfluidic Device

As reviewed previously in Chapter 2, the biggest restriction of the glass capillary device is the non-flexible geometry restricting applications that require additional inlets or outlets in between the formation process. Also, constraint by its laborious and costly fabrication process in mass production. PDMS device, on the other hand, can be easily reproduced through the stamping technique but limited application due to its low chemical resistance properties. Therefore, incorporating the advantages of the materials and their intrinsic surface properties lead to an alternative means of hybrid microfluidic device to generate double emulsion droplets.

The initial inspiration of this research project was to reproduce monodisperse gas-filled micro-particles, demonstrated by Duncanson *et al.*[107], as the template to generate core-shell W/O/W structured micro-reactor. However, due to the limited laboratory resources, a hybrid microfluidic device incorporating a glass capillary tube into the PDMS structure was developed and established to replace the reported glass capillary microfluidic device. On top of that, diluted dyed water was used to represent the gas-forming inner aqueous phase and demonstrate the droplet formation mechanism before the system was established for microreactor application.

The fabrication materials were chosen based on their advantages of high availability and well establishment. To fully utilise the intrinsic properties of each materials, PDMS was used as the primary material to ease mass production while enabling flexible modification in channel geometry and providing hydrophobic environment for the formation of W/O emulsion. The insertion of glass capillary tube allows permanent

surface properties alteration i.e. hydrophilic environment at the downstream of the device to further enhance the formation of W/O/W droplets. Since PDMS is intrinsically hydrophobic whereas glass capillary tube is intrinsically hydrophilic, this arrangement allows the hybrid microfluidic device to bypass chemical surface modification permanently.

In this chapter, the final optimised design of the microchannel geometry was used to first illustrate the fabrication methodology (Section3.3) and process analysis (Section 3.4.1 and 3.4.2). The development and optimisation of the microchannel design will be discussed in Section3.4.3. The experimental SOP was then optimised.

3.2 Microchannel Geometry Design of the PDMS – Glass Capillary Hybrid Microfluidic Device (PGHD)

The design of the microchannel geometry was constrained by 4 main factors: (1) the number of syringe pumps available (2) PGHD required at least two independent inlets to deliver the distinct inner aqueous phase (3) the single chip microfluidic device needs to be separated into two parts for glass capillary tube insertion (4) dimension of the downstream channel were restricted by the outer diameter of the glass capillary tube i.e. 1mm.

PGHD was made of two PDMS layers with the glass capillary tube sandwiched. The upstream of the hybrid microfluidic device provides hydrophobic surface for the W/O droplets formation while the downstream of the hybrid microfluidic device altered the surface environment with the presence of the glass capillary tube to enhance the capability of W/O/W droplets encapsulation (Figure 3-1).

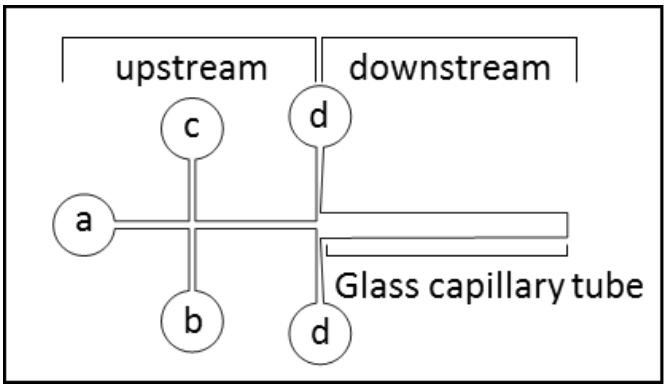

Figure 3-1. Schematic diagram of PGHD – A2 (final design)

3.3 Fabrication Methodology of PGHD

The master mould of the PGHD was fabricated via the modified Xurography process [108]. The design of the microchannel geometry was drawn using conventional drawing software then sent to the cutting plotter (CE6000-60, Graphtec, Yokohama, Japan) and plotted onto a 200mm adhesive vinyl film (Oracal Intermediate Cal 651, Orafol, Oranienburg, Germany) (Figure 3-2a). The adhesive vinyl film with cut design were aligned and stacked to achieve the desired thickness i.e. 1000mm (Figure 3-2b). The aligned vinyl film was transferred to a blank PDMS slab and adhered onto a paper mould (Figure 3-2c).

The epoxy resins and hardener (CP362 A/B, Oriental Option Sdn Bhd, Penang, Malaysia) were prepared at a ratio of 2:1 (w/w) and poured into the paper mould to be cured overnight at room temperature (25°C) (Figure 3-2d). PDMS pre-polymer (Sylgard 184, Dow Corning, Midland, MI, USA) prepared at a ratio of 10:1 (w/w) were poured into the master mould and left for partial curing (Figure 3-2d). The partial cured PDMS layers were peeled from the master mould and aligned via a custom-made PDMS aligner (Figure 3-2e). The double layer aligned PDMS layers was heated 2 hours at 80°C for completion (Figure 3-2f).

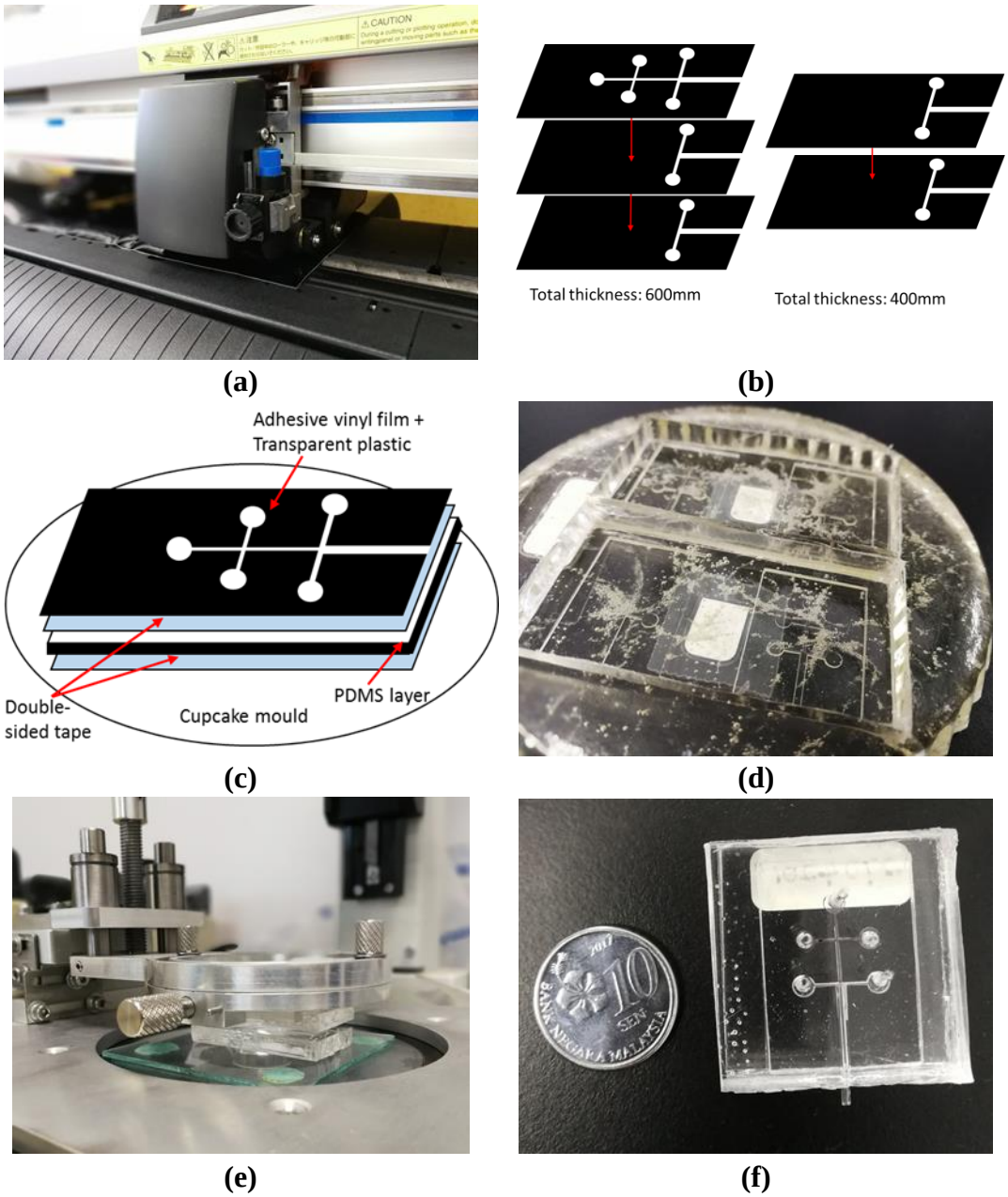

Figure 3-2. Fabrication of the PGHD. (a) Vinyl film cutting. (b) Vinyl film design layering. (c) Layering for epoxy mould fabrication. (d) Fabrication of PDMS layers. (e) Alignment and sealing of the PGHD. (f) Completed PGHD with RM 0.10 for comparisons.

3.4 Performance Analysis

The performance of the modified Xurography technique and experiment technique was tested according to the process flow chart summarised in Figure 3-3 then optimised accordingly. The optimisation process can be divided into geometry design, fabrication methodology and experiment methodology.

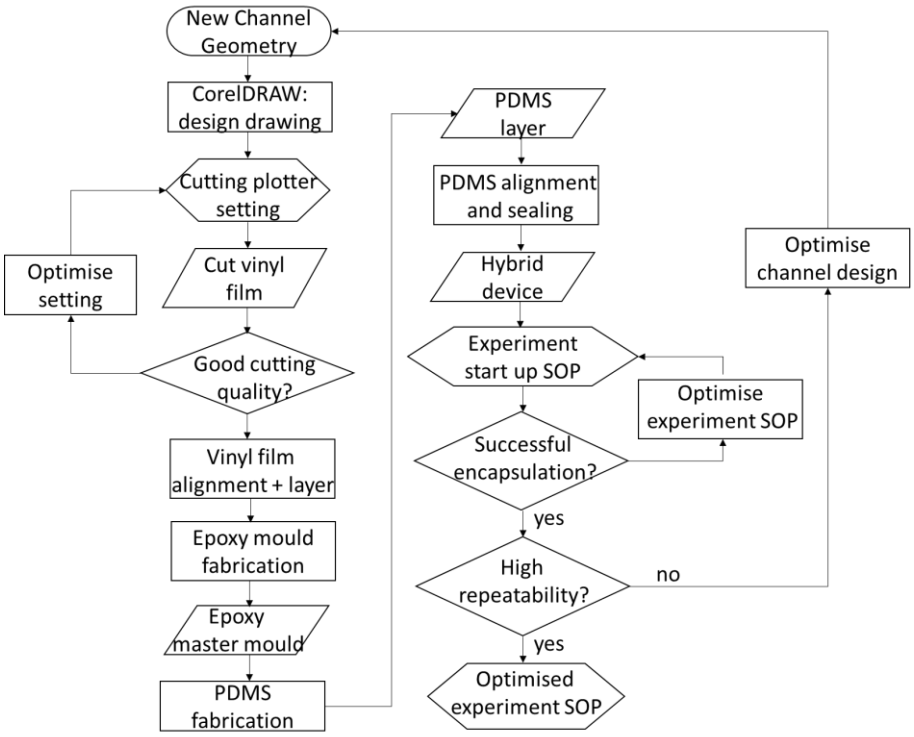

Figure 3-3. Overall process flow in developing the PGHD.

To avoid unnecessary waste, the cutting plotter optimisation was first carried out with a simple cross-junction geometry before fine-tuning according to the final design. The channel height of the device was fix at 0.2mm at the upstream and 1mm at the downstream for the accommodation of the glass capillary tube. To achieve different channel height in a single piece of device, the desired design was cut on a pre-adhered two layers vinyl film then aligned to produce desired height. Assurance of sharp edge corner cutting and the consistency in alignment and sealing of the microfluidic device would be the final goal in this research scope.

3.4.1 Process Analysis: Cutting Plotter Optimisation

Figure 3-4 below summarised the optimisation of the cutting plotter in a flow chart for better illustration.

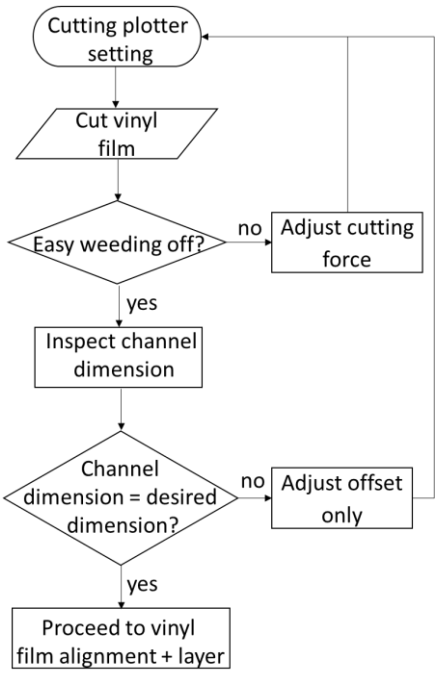

Figure 3-4. Process flow for cutting plotter optimisation.

Plotting quality can be directly affected by cutting force, offset value and cutting direction etc [108]. The cutter blade (CB09UB, Graphtec, Tokyo, Japan) was used to optimise the plotting on a 200 μm thickness of vinyl film. The blade length was first adjusted and fixed to the optimum length using the built-in function by setting the desired cutting thickness.

Pinto *et al.* [84] previously compared the geometrical quality of the master mould with the corresponding microchannel geometry using three sets of channel widths, i.e., 200, 300 and 500 μm and showed largest inconsistencies in the channel width at 200 μm with approximately of 50 μm difference. Hence, the cutting quality was optimised and analysed on channel width ranging from 150 μm to 350 μm for comparison.

3.4.1.1 Cutting Force

The cutting force value specified the force applied to the blade by the cutting plotter and affects directly on the cutting quality. At optimal cutting force, smooth cutting line can be obtained where the cut design can be easily weed off. In this study, the cutting

force was altered within a range of value:10-20 (1.16N-2.32N, 1 is equivalent to 0.116N) whilst keeping other parameters at default to be fine-tuned later.

At the value of 10 (1.16N), the cut vinyl film has visible outline, but design was unable to be weeded off indicating undercut condition. Figure 3-5(a) shows the microscopic image of the undercut vinyl film at the value of 12 (1.39N). The design was shredded during the weeding process leaving a rough cutting line behind. Figure 3-5(b) shows the vinyl film cut at cutting value of 16 (1.86N). Weeding can be done easily with minimal force applied presenting a neat cutting line indicating optimal condition. When the force is higher than optimal, the design was weeded off by the blade during the cutting process. Vinyl film was teared slightly during overcutting. Occasionally, overcutting (Figure 3-5c) produced a clean cut with smoother channel compared to the optimised value however it is not favoured since the blade was forced to cut through the backing sheet and damaged easily.

(a) **(b)** **(c)**

Figure 3-5. (a) Undercut vinyl film at the cutting value of 12 (1.39N). (b) Vinyl film with the optimal cutting value of 16 (1.86N). (c) Overcut vinyl film at the cutting valueof 20 (2.32N). All scale bars represent 1000 µm.

3.4.1.2 Offset Adjustment and Optimisation

The blade of the cutting plotter was slanted in 45° resulting a distance between the centre line and the cutting point i.e. offset distance (Figure 3-6a). While plotting a design, the plotter commanded the blade to move according to the centre line instead of the tip of

the blade. Since the cutting point of the blade lies behind the centre line, the offset value decides the channel dimension and sharp-edged cutting. Offset value was altered from value -2 to +2, keeping the optimised cutting force. The measurement of the channel width was done via ImageJ in 4 locations for each offset value tested, represented by the dotted line and numeric figures in Figure 3-6b, showing the cutting sequence and the cutting direction of the blade. The error percentage of each offset value was calculated by Equation 15 using the average width value (Figure 3-7).

$$error\ percentage = \frac{|actual\ width - desired\ width|}{desired\ width} \times 100\% \qquad \textbf{Equation 15}$$

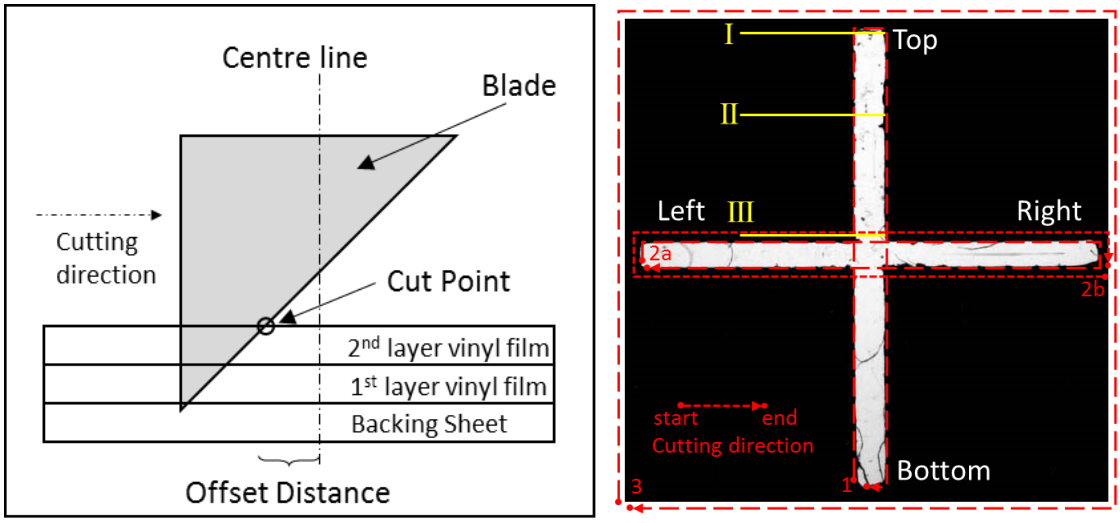

(a) **(b)**

Figure 3-6. (a) Schematic illustration of the cutting mechanism. (b) Measurement location of the vinyl film with the cutting direction.

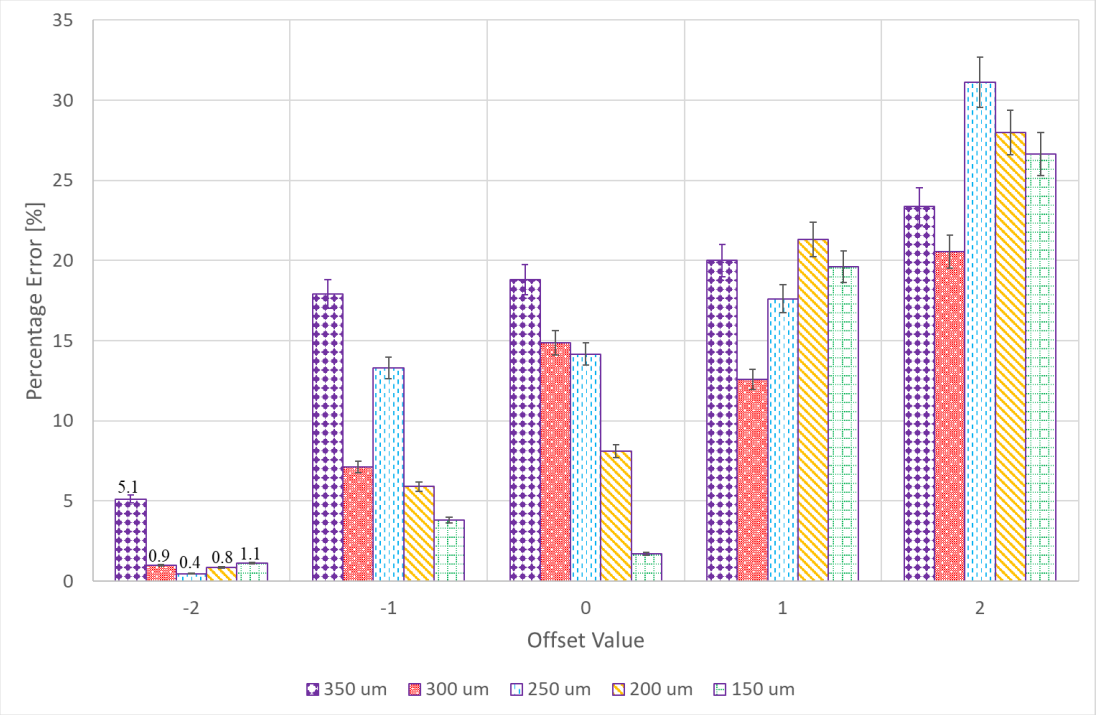

Figure 3-7. Error percentage of different offset value tested, with lowest at -2, below the 5% acceptable range.

Overall, offset value -2 shows lowest error percentage for all channel width, where the measured channel width enlarged with increasing offset value, resulted from the increasing distance of the centre line sent beyond the corner. Figure 3-8 below shows the effect of cutting direction towards the cutting width. Patterns of different channel width but identical plotter setting were cut in a row with two cutting directions: the first piece of the row was plotted according route 2a while the remaining pieces were plotted according to route 2b. The cutting direction affects the channel width produced i.e. slightly larger left channel width than the right channel depending on the starting point. However, the plotter did not cut the pattern in sequence, instead, started with the second column, C2 based on its own algorithm (table in Figure 3-8). This explains the inconsistent geometry presentation for the identical channel width. This finding is useful as the cutting defects can be concealed by rotating the design before sending to the plotter and minimised the impact towards the channel.

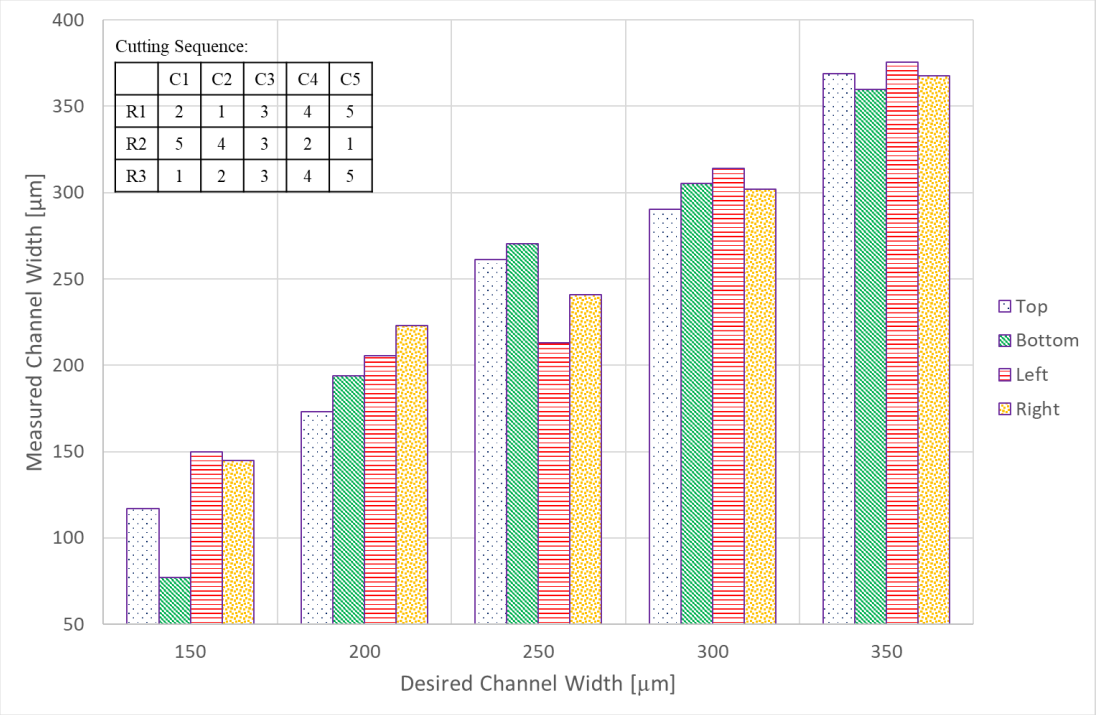

Figure 3-8. Measured channel width at different location indicating the effect of cutting direction (Cutting value = 16; offset = -2). The table shows the first three row (R1-R2) of the plotter cutting sequence where column 1-5 (C1-5) indicates arrangement of channel width in descending order (350 – 150 µm respectively).

Analysis shows consistent error for channel width 350 µm and 250 µm at offset value of -1, 0 and +1 indicating minimum adjustment by the plotter. For channel width 200 µm and 150 µm, the variation of the percentage error fluctuates with the offset value indicating the significance of the offset value to small channel width. Although the error also varies at 300 µm channel width, however the measured value was precise due to the wide channel.

For quantitative analysis, the measurement of the channel width was taken at 3 different positions (labelled I-III in Figure 3-6b), hence the scattered value at channel width of 250 µm and below. Position I have the narrowest width especially at small dimension (150 µm), resulted by the shorter distance cornering. The effect, however, was not significant since position I was connected to inlet or outlet reservoir eliminating the inconsistent channel width. Although the 150 µm channel was more difficult to be weeded due to its small dimension, the error percentage still falls under the acceptable range after

the optimisation showing better consistency and efficiency to reported work by Pinto *et al.* [84].

3.4.2 Process Analysis: PDMS Aligner

3.4.2.1 Overview and Objective of PDMS Aligner

PDMS aligner (Figure 3-9) is a custom – made portable device to increase the alignment precision between two PDMS layers.

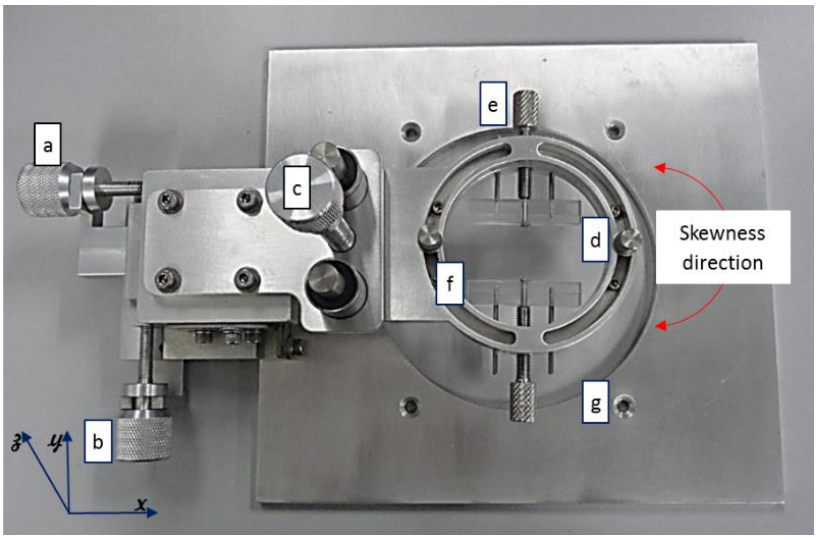

Figure 3-9. Portable PDMS aligner (Labels: (a) Left-right knot. (b) Up-down knot. (c) Top-bottom knot. (d) Skew adjustment knot. (e) PDMS-clip tightened knot. (f) PDMS clip. (g) Screw hole.).

The 4 main functional knots (labelled a-d) were designed to adjust the PDMS layer along *x*, *y*, *z* directions with skewness adjustment respectively when necessary. The precise alignment is essential especially at the downstream (double planar) of the PGHD. Before the introduction of PDMS aligner, the microfluidic device was aligned manually under the light inverted microscope increasing the possibility of misalignment, as it is highly dependent on the individual alignment skills (Figure 3-10).

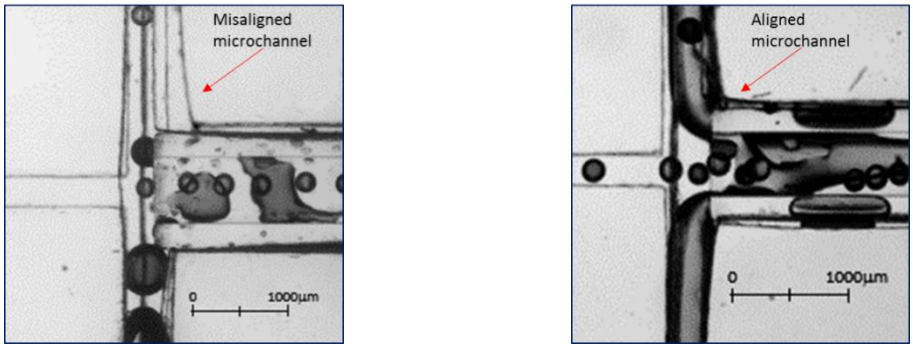

(a) **(b)**

Figure 3-10. (a) Misaligned microfluidic device with deformed cross-junction. (b) Microfluidic device with good alignment.

3.4.2.2 Standard Operating Procedure (SOP) of the PDMS Aligner

Figure 3-11 shows the digital image of PDMS aligner process at the right column with their respective view under the light inverted microscope at the left column. The alignment process can be summarised into 4 main steps: (1) Placement of the PDMS layers (Figure 3-11a – b), (2) Placement of the glass capillary tube (Figure 3-11c – d), (3) Adjustment and alignment of the PDMS layers (Figure 3-11e – f) and (4) Gas bubbles removal and sealing of the PDMS layers (Figure 3-11g – h). The PDMS layer alignment initiated by fixing the PDMS layer with more complex design on the microscopic stage (bottom layer) while the PDMS layer with a simpler design was clipped to the PDMS aligner (top layer) as shown in Figure 3-11b. This arrangement allows focus fixed on the bottom layer and double planar area where the glass capillary tube is fixed. The glass capillary control (Figure 3-11a) was designed as the benchmark to place the glass capillary tube and its necessity will be further discussed in Section 3.4.3

After placing the glass capillary tube, the top PDMS layer was lowered down until a blur geometry outline was observed (Figure 3-11e). At this stage, the top PDMS layer can be adjusted without disturbing the glass capillary tube, until both geometry outlines overlapped and aligned (Figure 3-11f). The top PDMS layer was then further lowered down towards the bottom PDMS layer and released by loosening the PDMS clip. The air

bubble was removed manually, then sent for heating to complete the sealing (Figure 3-11h).

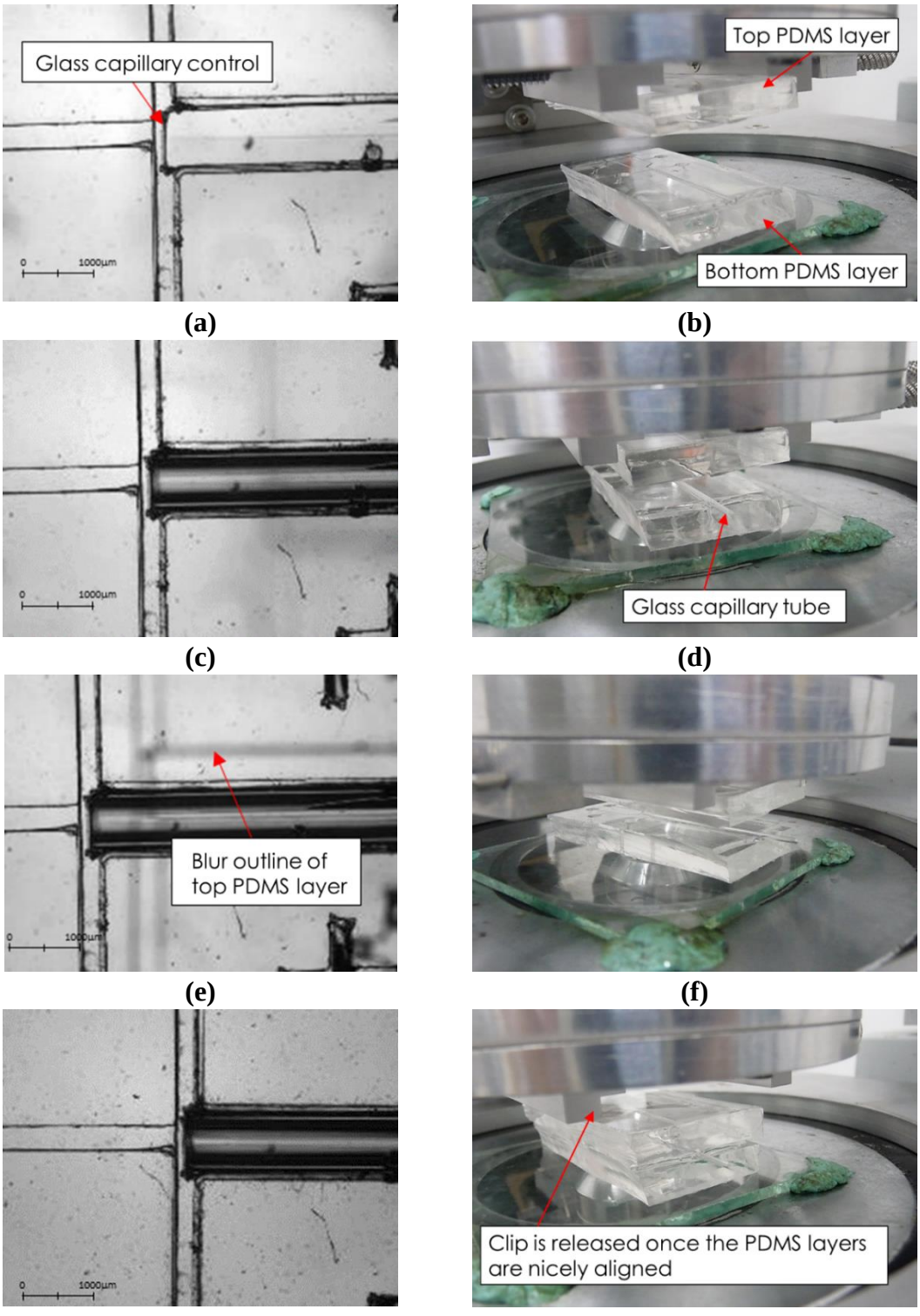

Figure 3-11. Digital image of the alignment process using the PDMS aligner with their respective microscopic view.

3.4.2.3 PDMS Aligner Results Analysis

This section compares the alignment efficiency and precision of the PGHD that was aligned manually and by aligner. To achieve quantitative analysis, 10 trials were carried out each for both manual and aligner alignment under the microscope. Five measurements were taken at different positions i.e. cooking oil channel (A1-A5 in Figure 3-12a), diluted red dye channel (B1-B5 in Figure 3-12b), diluted blue dye channel (C1-C5 in Figure 3-12b), diluted yellow dye channel (E1-E2 & F1-F2 in Figure 3-12b), including the distance between the glass capillary control and the outlet of the upstream, δ (D1-D5 in Figure 3-12b). δ was measured to ensure the precision in placing the glass capillary tube. The value of five measurements were averaged, then error percentage was calculated based on the desired dimension. Since the error percentage between the desired design and cut vinyl film is negligible (Section 3.4.1), the analysis in this section was directly compared with the desired channel dimension (Figure 3-13).

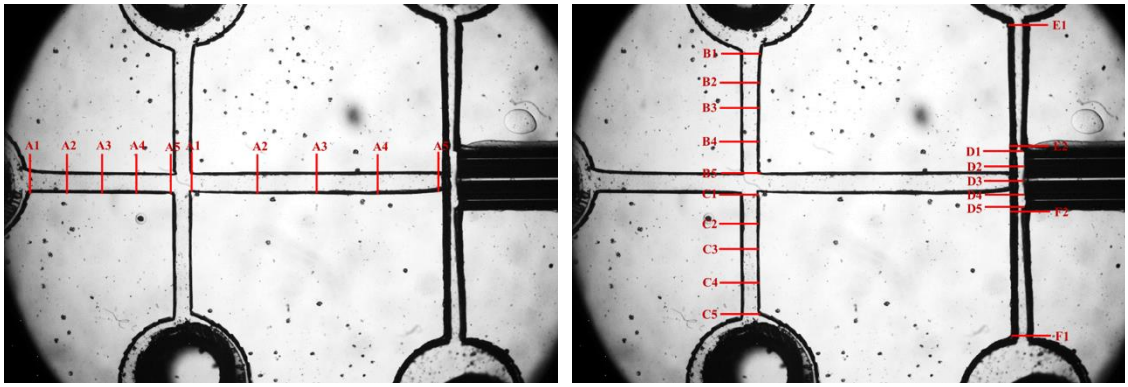

(a) **(b)**

Figure 3-12. (a) Image of aligned PGHD with measurement position of cooking oil channel labelled. The average value was calculated by the 10 readings measured. (b) Image of aligned PGHD with measurement position of diluted water channel and δ labelled. The label indicates different channel category: A= cooking oil channel; B= diluted red dye channel (Red); C= diluted blue dye channel (Blue); D= δ; E= diluted yellow dye channel 1 (Yellow1) and F= diluted yellow dye channel 2 (Yellow2).

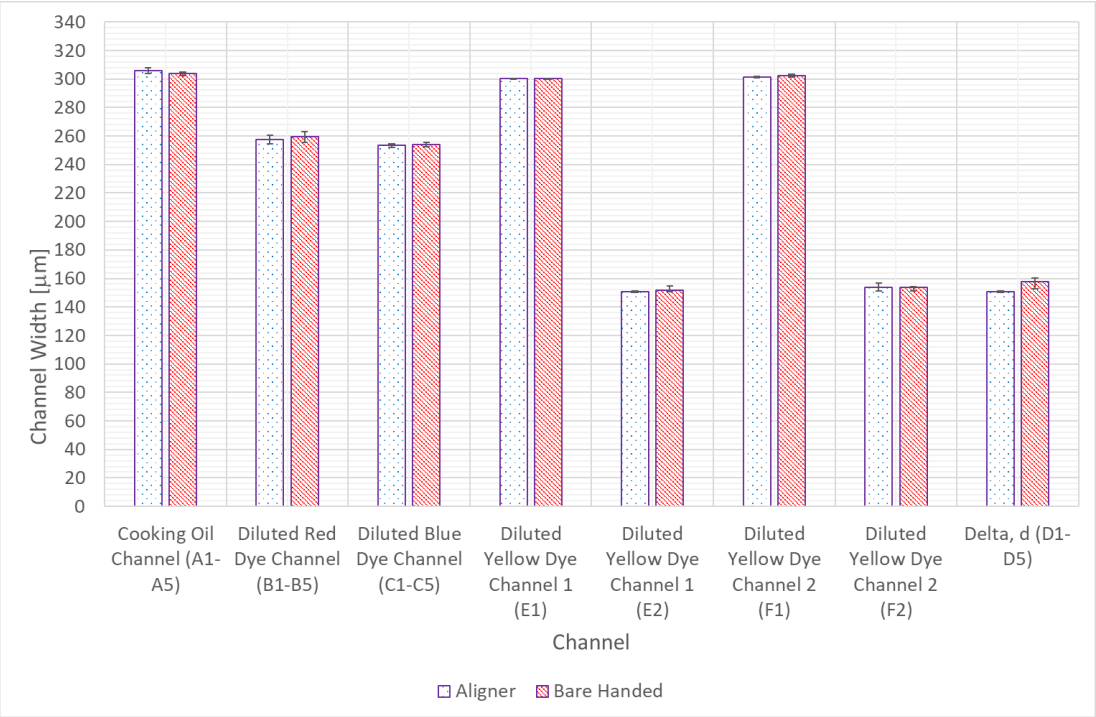

Figure 3-13. Comparisons of the channel width at each channel after aligned with both methods.

Generally, the average channel width for cooking oil, diluted red dye and diluted blue dye were similar for both aligner and manual alignment due to the single layer design. The channel width of the diluted red dye channel is slightly higher due to the plotter limitation mentioned in Section 3.4.1. The channel width is larger at position B1 and narrow towards position B5 due to the cutting direction (Figure 3-12b). Although the average diluted red dye channel width is slightly larger, the percentage error was still maintained below 5%. At downstream, the yellow diluted dye was tapered from 300 – 150 µm, therefore, no average value was taken. Instead, the measurement was done independently for each trial at the two locations. The detail design geometry of the PGHD will be further discussed in Section 3.4.3.

In general, the error percentage is lower when using the aligner especially at δ indicating the consistent precision in placing the glass capillary tube. By using the aligner, sealing and placement of glass capillary tube was easier as the process can be paused at certain height to slowly adjust the alignment. This is important due to the different focus

of the top PDMS layer at different height. If the glass capillary tube position is disturbed during the alignment process, the top PDMS layer can be lifted without affecting the aligned coordinates to adjust the glass capillary tube. In contrast, the top PDMS layer must be peeled off and realigned for manual alignment. In overall, longer duration is required when using an aligner (112 seconds). This is because the adjustment knot is based on µm interval hence better precision compare to manual alignment (40 seconds).

3.4.3 Design Analysis: Microchannel Geometry of the PGHD

The design criteria and objective of the PGHD have been introduced in Section 3.1 and 3.2. In brief, the channel design of the PGHD was modified accordingly to achieve simple and systematic experimental start-up and enable encapsulation. The overall process flow of optimisation in refining the function of the PGHD was summarised in Figure 3-14. The channel geometry design was modified and optimised based on a crucial factor - the repeatability of the fabrication and experiment.

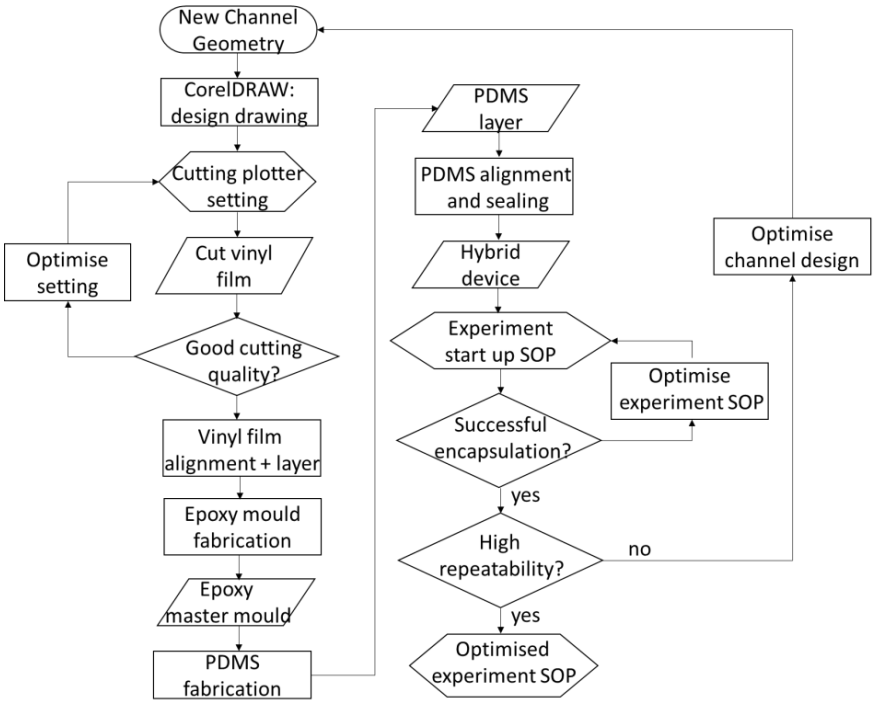

Figure 3-14. Overall process flow summary.

The aim of the PGHD was to produce monodispersed double emulsion droplets efficiently for future industrial mass production with low cost input. The device design was justified based on the experimental success rate, device's efficiency and repeatability. The device was designed, fabricated and then tested with various flow ratio set, to analyse its functionality for better optimisation, including the channel geometry and experimental SOP. The droplet size, sequence and number of encapsulation was optimised via flow manipulation at the later stage. Figure 3-15 tabulated the variation of the channel design. The design aspect will be discussed from that instant point of view under each subsection.

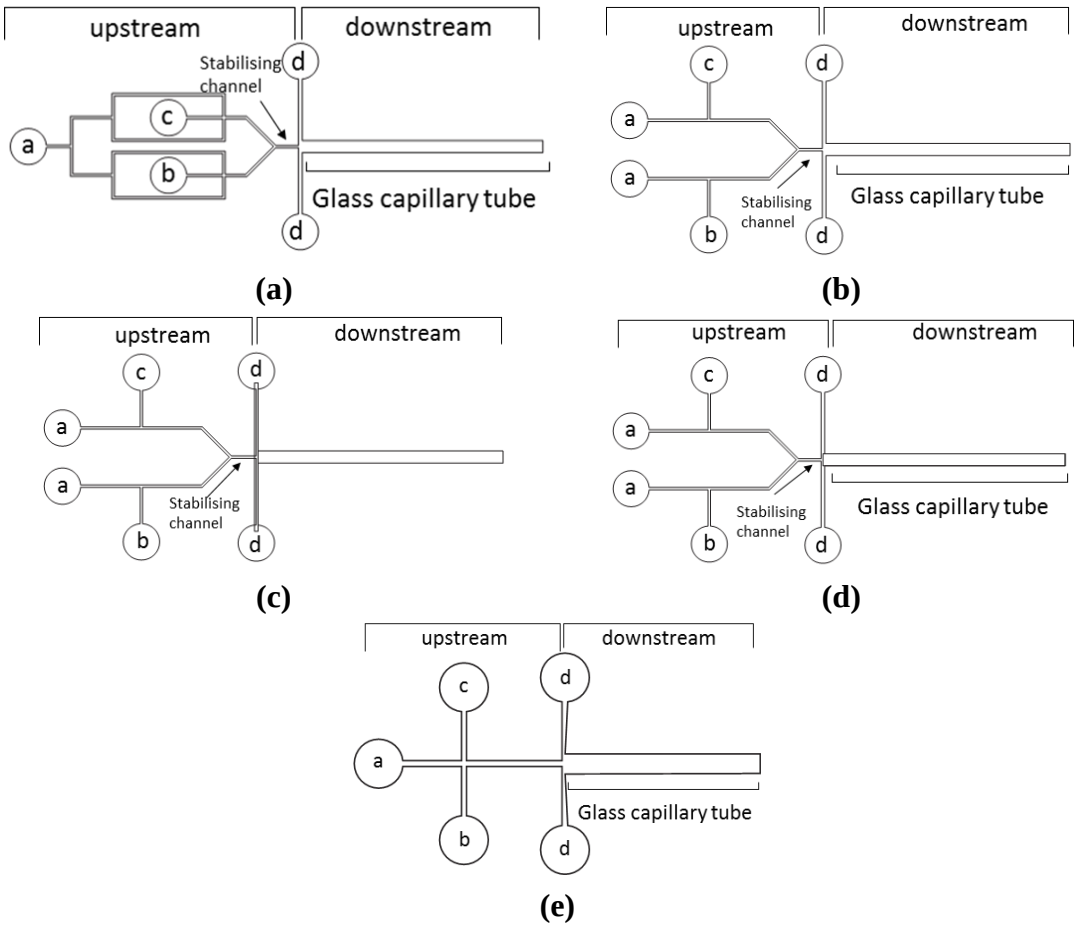

Figure 3-15: Schematic diagram of the channel geometry design. (Labels: a. cooking oil inlet. b. diluted blue dye inlet. c. diluted red dye inlet. d. diluted yellow dye inlet). (a) Design A – Preliminary design. (b) Design A1 – Extension of Design A without control. (c) Design A1-1 – Extension of Design A1 with control. (d) Design A1-2 – Extension of Design A1 with control. (e) Design A2

3.4.3.1 Design A – Preliminary Design

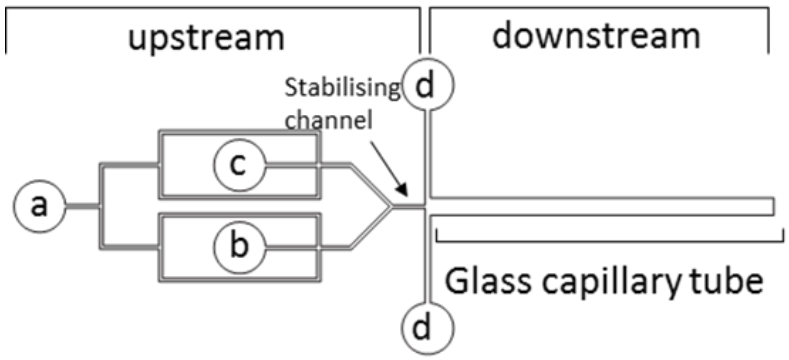

Figure 3-16. Schematic diagram of Design A (a. cooking oil inlet, b. diluted blue dye inlet, c. diluted red dye inlet, d. diluted yellow dye inlet)

Initial design of the PGHD (Figure 3-16) utilised the flow focusing technique at the upstream and downstream for droplet generation and encapsulation. This assured identical shear stress applied from the continuous phase towards the dispersed phase to produce smaller-sized monodispersed droplets. At the initial stage of the research work, the available syringe pumps were NE-1000, NE-4000 and KDS-200 with only 5 syringe holders in total, limiting the number of inlets. To overcome the limitations, the channel of cooking oil in Design A was bifurcated into 4 sub-channels. While conservation of energy stated identical liquid flow at each bifurcated channel, Design A, however, shows uneven flow at every bifurcated channel due to the blockage caused by the air bubbles. Hence, fluid did not flow smoothly into each channel as expected during the start up. Instead, the fluid tends to flow into a path with lesser resistance leaving the blocked channel unpurged. The experiment start-up process was prolonged while the PGHD unsealed easily due to the pressure built-up inside the device.

3.4.3.2 Design A1 – Extension of Design A without control

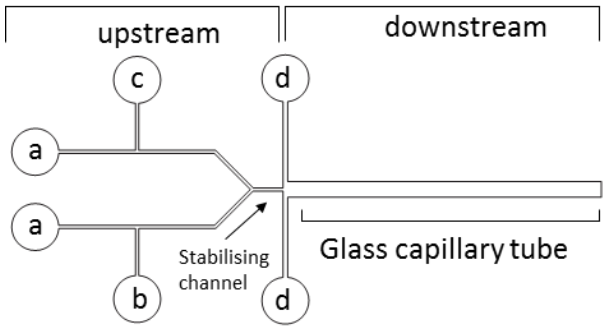

Figure 3-17. Schematic diagram of Design A1 (a. cooking oil inlet, b. diluted blue dye inlet, c. diluted red dye inlet, d. diluted yellow dye inlet)

Design A1 (Figure 3-17) was simplified from Design A. At this stage, the syringe pumps used was NE-4000 and two KDS-200 with a total of six syringes holders. The number of cooking oil inlet was increased, utilising two independent T-junction geometries to generate droplets at the upstream, eliminating bifurcating channel. The width of the stabilising channel was increased to slow down the flow of the inner droplets before entering the glass capillary tube. The stabilising channel function as a transition stage, to converge and slow down the inner droplets, preventing collision at the entrance of glass capillary tube. The simplified upstream design increased the success rate of the droplet generation and improve the experiment initiation time. However, manual control was required during the experiment start-up to avoid backflow into the reservoir whereas the droplet encapsulation was still random and unpredictable.

The position of glass capillary tube was initially aligned with the inlet of the collection channel. However, due to the immature fabrication skill at the initial stage, the location of the glass capillary randomly varies between the distances from 0δ to 1.5δ, affected by the sealing force and device expansion caused by overheating (Figure 3-18). Experimental work carried out using PGHD with different glass capillary positions shows successful encapsulation occurs mostly when the glass capillary tube was positioned near to 0.5δ. Hence the optimised Design A1a with glass capillary control.

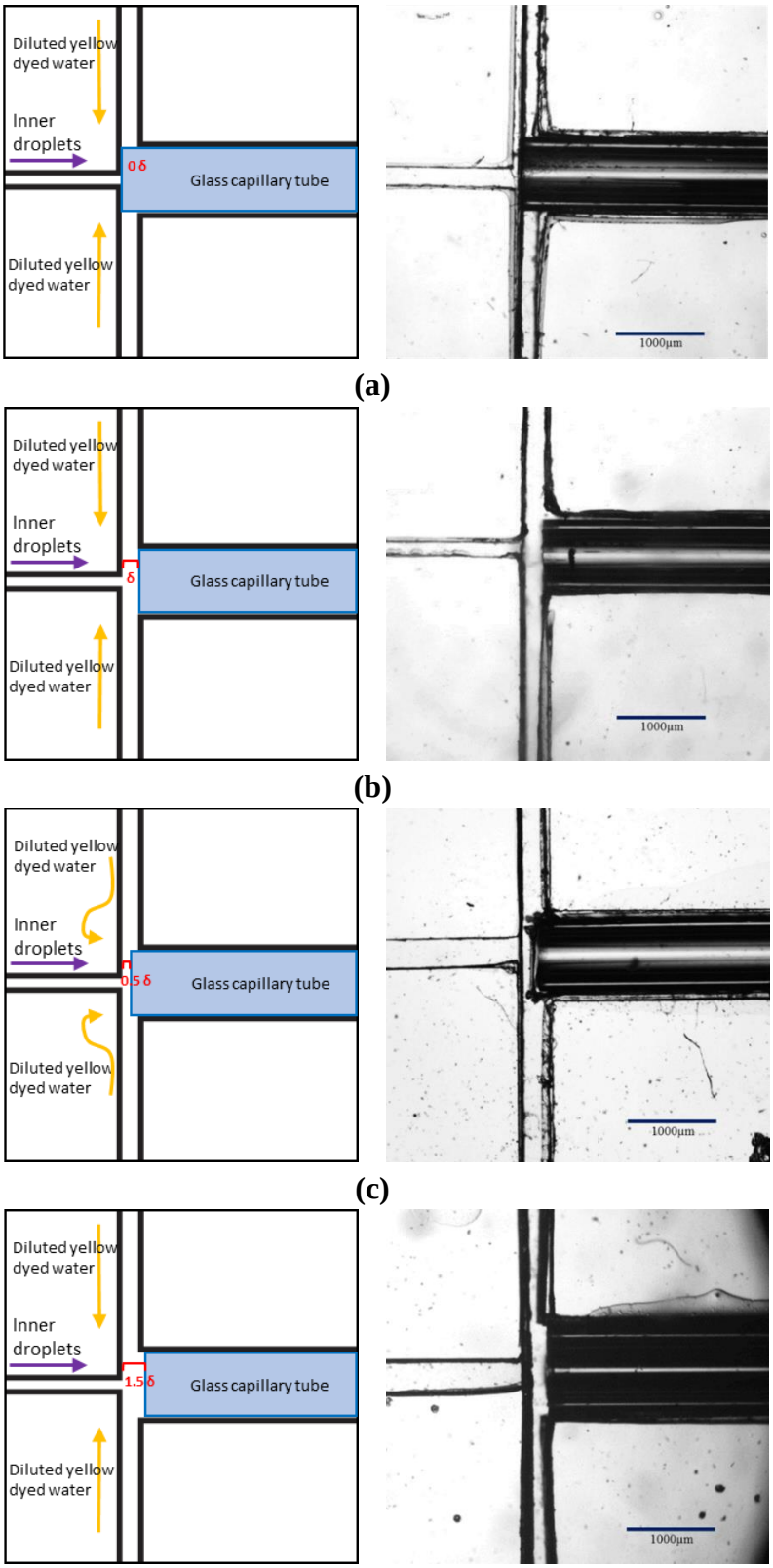

Figure 3-18. (a) Glass capillary tube positioned at 0δ. (b) Glass capillary tube positioned at δ. (c) Glass capillary tube positioned at 0.5δ. (d) Glass capillary tube positioned at 1.5δ. The yellow arrow indicates the flow direction of the diluted yellow dye while the purple arrow indicates the flow direction of the W/O emulsions droplets towards the glass capillary tube.

3.4.3.3 Design A1a – Extension of Design A1 with control

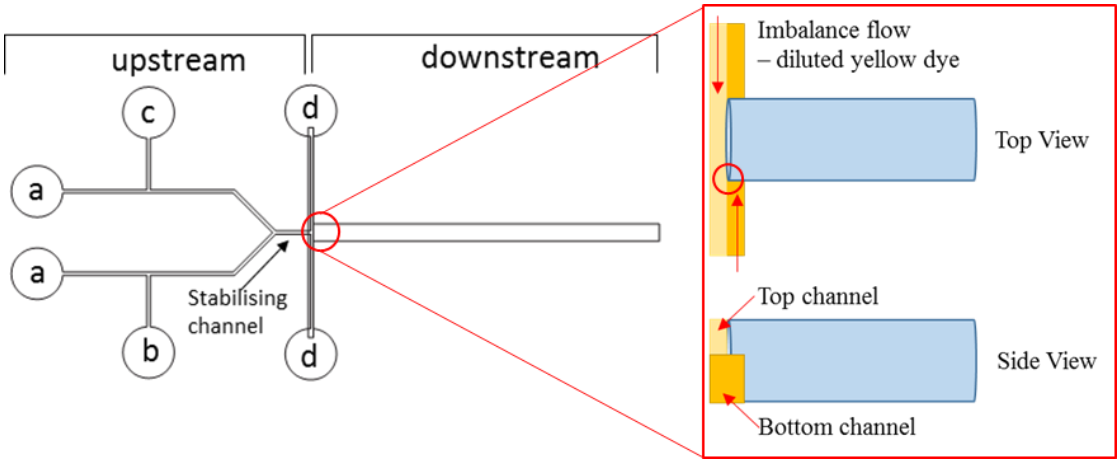

Figure 3-19. Schematic diagram of Design A1a (a. cooking oil inlet, b. diluted blue dye inlet, c. diluted red dye inlet, d. diluted yellow dye inlet)

Design A1a (Figure 3-19) is the initial design with control for the position of glass capillary tube. The channel width of the diluted yellow dye was reduced to 0.15mm for top layer while maintaining 0.3mm at the bottom layer. However, this design caused imbalance flow of the diluted yellow dye into the glass capillary tube. The location of glass capillary tube caused an extra opposition force as indicated by the red circle in Figure 3-19 top view. This imbalance flow resulted a circulated motion at the entrance of the glass capillary tube. The flow circulation resulting the collision of the inner droplets at the entrance of the glass capillary tube, hence empty encapsulation.

3.4.3.4 Design A1b – Extension of Design A1a with control

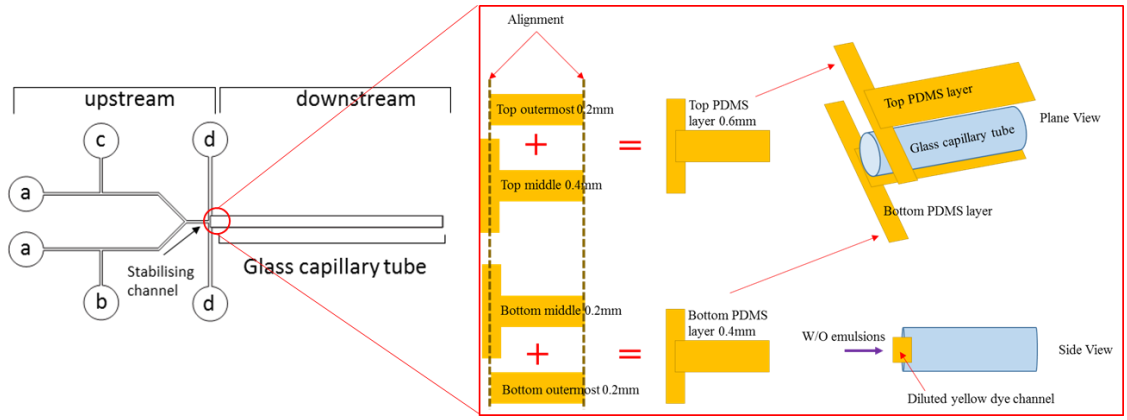

Figure 3-20. Schematic diagram of Design A1b (a. cooking oil inlet, b. diluted blue dye inlet, c. diluted red dye inlet, d. diluted yellow dye inlet)

Design A1b (Figure 3-20) was an optimised version of Design A1a. Instead of modifying the diluted yellow dye channel width, the height of the channel was reduced to 0.6 mm. The controlled channel with 0.2 mm height was placed at the outermost layer to accommodate the glass capillary tube as shown in Figure 3-20. The plane view shows how the glass capillary tube was sandwiched in between the two PDMS layers while the side view shows how the diluted yellow dye is now focus at the middle layer of the glass capillary tube to create a balance flow encapsulating the W/O emulsions, without being disturbed by the controlled layer. Hence, the inner droplets no longer collide with each other and the success rate of encapsulation has been increased. Although the droplet formation and encapsulation have been ensured, the hybrid system is still inconsistent in terms of droplet breakup point and number of encapsulation.

The inner droplets were formed independently before the stabilisation channel. During the convergence, droplets paused before entering the stabilisation channel, pairing the red and blue droplets together with large spacing between each pair. Overtaking between the two droplets happen occasionally at the stabilising channel. Besides, the pairing was disturbed prior entering the glass capillary tube due to the enlarged channel and reduced velocity, leading to inconsistent number of inner droplets encapsulated. Different flow rate ratio has been manipulated to verify the encapsulation. The success rate of the encapsulation process increased but remains unpredictable due to the improper pumping sequence (Section 0).

3.4.3.5 Design A2 – Final Optimised Design

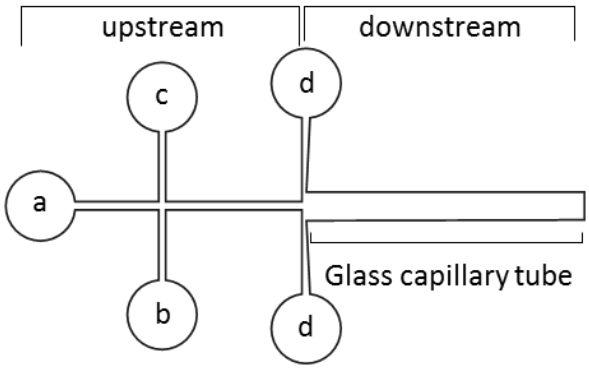

Figure 3-21. Schematic diagram of Design A2 (a. cooking oil inlet, b. diluted blue dye inlet, c. diluted red dye inlet, d. diluted yellow dye inlet)

Design A2 (Figure 3-21) was modified with reference from Okushima *et al.*[27], which briefly introduce the dual T-junction design with alternating red and blue inner aqueous droplets formation and distinct droplets encapsulation. Hence, the main reason of this modification was to optimise the inner droplet sequence. Previously, the upstream of the device were designed as independent inner droplet formation channel then converged by the stabilising channel before the encapsulation process. Design A2 simplified the upstream into a dual T-junction, eliminating the droplets convergence by the stabilising channel, generating consistent spacing between the inner droplets.

The channel dimension was modified accordingly: (1) cooking oil main channel increased to 0.30mm. (2) Diluted red and blue dye channel width increased to 0.25mm for better fabrication performance. (3) Overall upstream main channel length was reduced due to the elimination of the stabilising channel. (4) Length of the glass capillary tube was reduced and fixed at 1.5mm, taking Hagen-Poiseuille equation into account. (5) Diluted yellow dye channel was tapered to produce 0.3mm width at the reservoir and 0.15mm near the glass capillary tube entrance (3° slanting angle), serve as the position benchmark. The slanting channel reduces the error in alignment and stacking while directing the flow smoothly towards the glass capillary tube entrance. Besides,

eliminating the stagnant area near the glass capillary tube, possible cause of circular motion of inner droplets. The overall size of the PGHD was reduced half from approximately 5 cm to 2.5 cm in length.

Table 3-1 summarises the design criteria and performance of each PGHD. The encapsulation success rate is based on the encapsulation of two distinct inner droplets. Experiment repeatability described the repeatability of that respective design, if the encapsulation can be easily reproduced by another device of same design. The experiment start-up period includes the duration from pumping of inner fluid until the formation of encapsulation.

Table 3-1. Summary of the hybrid microfluidic channel design variation.

PGHD	Summary	Experiment Repeatability	Experiment start-up period
Design A	Bifurcated channel – pressure built-up in device	Low	>2hours
Design A1	Simplified Design A. Independent droplet formation. No control on glass capillary position.	Unpredictable	⩾1hour
Design A1a	First optimisation of Design A1. Distorted benchmark. Inner droplets collides – zero encapsulation	Medium	⩾1hour
Design A1b	Extension of Design A1-1 with optimised glass capillary tube location.	High	⩾45 minutes
Design A2	Dual T-junction eliminated stabilising channel. Overall device size reduced.	Very high	<15 minutes

3.4.4 Process Analysis: Standard Operating Procedure (SOP)

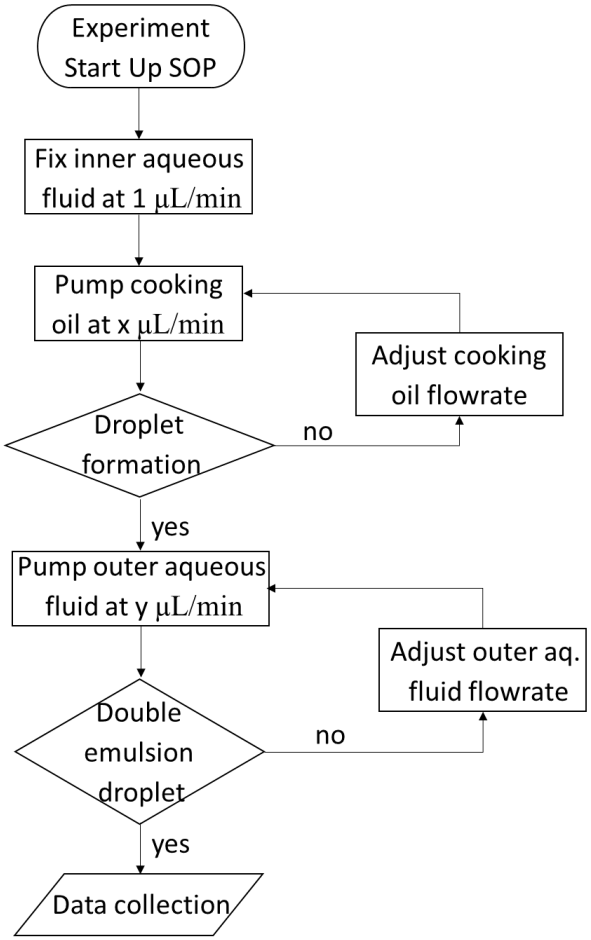

Figure 3-22. Experiment start-up SOP before optimisation.

Figure 3-22 shows the experiment start-up procedure (SOP) before optimisation. Proper SOP is essential to ensure the practicability of the PGHD. Before optimised, the encapsulation experiment was initiated by pumping the inner aqueous fluid at 1 µL/min then manipulate the cooking oil at *x* µL/min to achieve inner droplet formation. The hybrid system was left to stabilise the droplet formation for 30 min. The outer aqueous fluid was introduced after the formation of W/O emulsion, then allowed for an hour stabilisation period. The stabilisation of the hybrid system ensures the consistent droplet formation and encapsulation. This start-up procedure was applied for the Design A – A1b hybrid device and optimised at Design A2. This section introduces the flow phenomenon observed from the different start-up procedure which leads to the final optimised experimental SOP. The optimised SOP will be discussed further in Section 5.2.2.

During the preliminary stage of this research work, Design A was used to study the flow system. The inner aqueous fluid was fixed at 1 µL/min whereas the flow rate of the cooking oil was fixed at 12 µL/min where success formation of W/O emulsion is observed. The hybrid system was filled with air by default, hence, presence of air bubble. The air bubble resulted a lengthy start-up procedure during the purging at the bifurcating channel when liquid is pumped in. Assumption was made based on Bernoulli's principle where fluid flows from a higher pressure to lower pressure region, uniformly flow into each bifurcated channel. However, this statement was found to be invalid with the presence of the air bubble. Therefore, a pre-purging step was added as an extra procedure to eliminate the air bubble.

50% v/v diluted methanol was prepared for the pre-purging step. Before the start-up, diluted methanol was pumped into the device to purge the air out with a higher flow rate i.e. 1 mL/min for 1 min intermittently until the bubbles were removed. Theoretically, methanol falls under the category of low-solubility solvents, hence, compatible and do not swell the PDMS due to the high polar contributions [109]. However, visual inspection shows that long duration purging of methanol weakened the seal of the PDMS layer. The pre-purging method was unrealistic as the hybrid system unsealed easily due to (1) pressure built-up by the persistent air bubble, (2) weakened seal between the PDMS layer and (3) high flow rate bursting. These factors alone will not cause the PGHD to unseal when happened independently. On top of that, the air bubble still induced during the changing of syringes to replace the methanol with respective liquid i.e. cooking oil and diluted dyes. Hence, to reduce the possibility of unsealing, external force was applied to the device manually, simultaneously with 10 µL/min purging flow from each respective liquid. Generally, completely removal of air bubble requires 30-45 minutes. The system

was allowed at least 2 hours of stabilisation period to settle down from the previous high flow rate to the desired flow rate.

The flowing of organic phase into the aqueous phase channel was undesirable due to its similar hydrophobic properties with the PDMS channel wall. As the cooking oil flows into the diluted aqueous dye channel, it tends to adhere to the channel wall leaving a thin film of oil unable to be flushed when the diluted aqueous dye is pumped in (Figure 3-23a). This thin film of oil allows the cooking oil from the main channel to shear the aqueous phase at the middle of the diluted dye channel causing premature droplet breakage (Figure 3-23b), inducing instability into the system. Since the flow of the dispersed phase is lower than the continuous phase, the premature red droplets are resulted by the vigorous shear, hence polydispersed and small size. If the system was settled longer, the dispersed phase will slowly fill up the channel, but eventually premature break up happens again. The bifurcating channel increase the possibility of the contamination and hence eliminated.

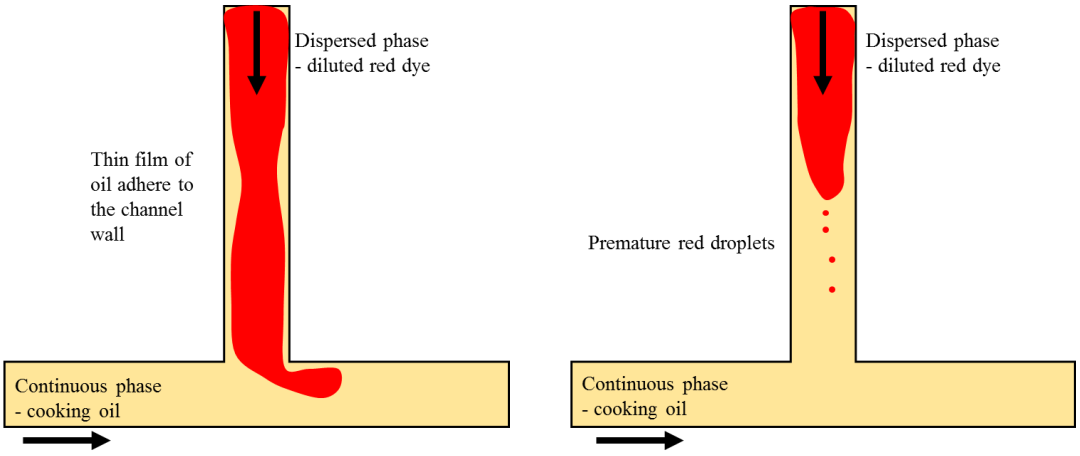

Figure 3-23. T-junction schematic diagram of diluted red dye channel. (a) Cooking oil contaminated the diluted dye channel and adhere to its channel wall, unable to flush away by the diluted red dye. (b) Cooking oil from the main channel attached to the thin film shearing the dispersed phase before it flows into the main channel producing premature droplets. The process repeats between (a) and (b) inducing instable droplet formation.

The mentioned phenomenon was observed in different design since the cooking oil tends to flow smoother in the PDMS device due to the hydrophobic adhesion. Therefore, to reduce the possibility of contamination, the inner fluid was pumped in before the tube of cooking oil is connected to the device. When Design A1 series was established, more flow experiments was conducted. The stabilisation period has been reduced to 1 hour after the first W/O/W encapsulation droplet was formed to obtain a more stable system for analysis. Although the monodispersity of the droplets increased with the duration of stabilisation period, the stabilisation period was fixed at 1 hour due to the capacity of the syringes. The success rate of the W/O/W double emulsion formation increased, however, still considered as randomised and uncontrollable. During the stabilisation period of W/O emulsion, the diluted yellow dye was not pumped into the device and hence the inner surface of the glass capillary tube was contaminated by the cooking oil from the W/O emulsion. Since glass capillary tube was known as hydrophilic surface, it was previously assumed that the cooking oil will be removed once the outer aqueous phase is pumped in due to the adhesion of similar surface properties.

The cooking oil however, was not removed smoothly after the outer aqueous phase was pumped in. Different phenomena were formed based on the situation: (1) the cooking oil formed a reservoir at the inlet of glass capillary and encapsulated by the outer aqueous phase forming W/O/W double emulsion (Figure 3-24a). The breakup point depends on the shearing of the outer aqueous phase washing off the adhered cooking oil (Figure 3-24b and c). (2) A layer of the outer aqueous phase was formed underneath the cooking oil thin film, forming a two-phase flow without encapsulation. The incoming cooking oil will contribute to both the outer layer and inner layer while the inner droplets either flow steadily in the inner layer of cooking oil towards the outlet (Figure 3-24e) or break and

mix with the diluted yellow dye (Figure 3-24d). (3) Mixture of inner and outer aqueous phase with cooking oil segment in between (Figure 3-24f).

To avoid the contamination of cooking oil onto the inner surface of glass capillary tube, the flow of inner phase and cooking oil was paused once they filled up the main channel while starting the outer aqueous phase. The outer aqueous phase was paused once the glass capillary tube was filled up, while the inner phase and cooking oil flow continued to form inner droplets. This is to ensure droplet formation before encapsulation while maintaining the continuous flow of outer aqueous phase to be sustained throughout the entire experiment. Refilling of syringes in the middle of experiment were undesirable since the system will be disrupted and reset. The pausing of flow did not eliminate the problem efficiently, because the effect does not take place immediately due to the inertial force and thus cooking oil continue to flow into the glass capillary tube. However, encapsulation was successful if the pausing effect took place in time. Hence, verify the importance of improving the start-up procedure to prevent early contamination of cooking oil.

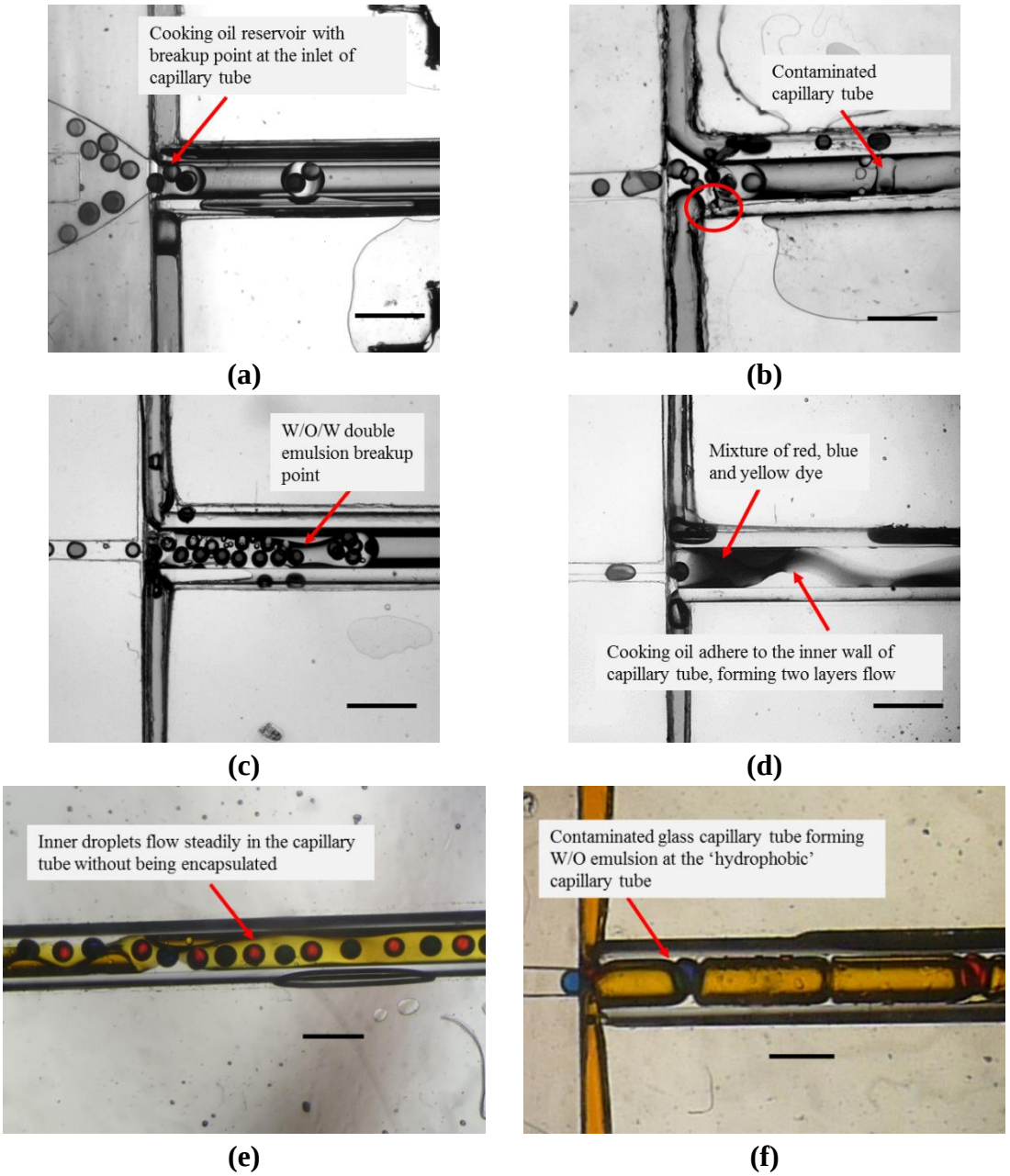

Figure 3-24. (a) Cooking oil forms reservoir at the inlet of the capillary tube, encapsulating the W/O emulsion when the capillary tube is not contaminated by the cooking oil. (b) Cooking oil contaminating the capillary tube, adhering to the inner wall, unable to be washed off by the diluted yellow dye. The red circle shows contaminated inlet leading to intermittent flow of diluted yellow dye. (c) W/O/W double emulsion breakup point towards the downstream where diluted yellow dye dominated the adhesion to inner capillary wall. (d) Capillary inner wall contaminated by the cooking oil. Diluted yellow dye unable to shear the cooking oil, instead channelling within the cooking oil forming two-phase liquid-oil flow. (e) The inner droplets flow steadily in the capillary tube without being encapsulated due to insufficient shear force. (f) Adhesion of cooking oil at the capillary tube altered the surface properties of the inner capillary wall into hydrophobic, hence forming W/O emulsion instead. All scale bar represents 1000 µm.

3.5 Short Summary

To conclude, the design of the PGHD has been improved and simplified to ensure the experimental practicability. Modified Xuragraphy method was used to fabricate the PGHD, where the cutting plotter setting have been optimised to achieved precision up till cutting width of 150 μm with 1.1% error. Based on the analysis shown in Figure 3-7, the final channel width of the PGHD was set at 250 μm (0.4% error) for the dispersed phase channel while the main channel was maintained at 300 μm (0.9% error). For glass capillary tube insertion at the downstream of the PGHD, the channel was designed 3D at the downstream and hence the necessity of sealing 2 PDMS layer. A custom-made portable aligner was designed for this purpose. The PDMS aligner was especially useful in placing the glass capillary tube with a 0.41% error, very much lower compared to the manual alignment i.e. 5.12%.

CHAPTER 4: DOUBLE ENCAPSULATION OF WATER-OIL DROPLETS

4.1 Experimental Objective

This chapter focused on the experimental materials, setup and analysis on the encapsulation experiment conducted by the PGHD of Design A – Design A1b (later mentioned as PGHD-A – PGHD-A1b). The final optimised design of the PGHD-A2 will be presented and discussed in Chapter 5. The W/O/W double emulsion was characterised by their droplet size, droplet sequence and number of encapsulation. The channel design was optimised to achieve alternating inner droplets and flow rate ratio was manipulated to obtain higher encapsulation rate of two distinct inner droplets. *CV* of the droplets was calculated to characterise the monodispersity of the W/O/W double emulsions. The flow physic was further characterised using dimensionless number.

4.2 Materials and Sample Preparation

Deionised (DI) water (18.2 MΩ-cm, Milli-Q, Millipore, Molsheim, France) was used as both inner and outer aqueous phase, blended cooking oil (μ 62.7 mPa.s) was used as the organic phase. The inner aqueous phase was prepared by adding 16.6% (*v*/*v*) and 9.0% (*v*/*v*) of Fortune-Red and True-Blue food colouring respectively into the DI water. The different colour and concentration make the inner droplets easily distinguishable under the view of the light inverted microscope. On the other hand, the outer aqueous phase was composed of a mixture of DI water with 11.8% (*v*/*v*) of Egg Yellow food colouring. To better study the flow and interface mechanism between the two fluids, the experiment was carried out without further addition of any chemical solvents including surfactants. The materials were all used as purchased.

4.3 Equipment and Experimental Setup

The W/O/W double emulsion experiment required the operation of three individual syringe pumps (Model KDS-200, KD Scientific Inc., Holliston, Ma, USA; NE-1000 and NE-4000, New Era Pump Systems Inc., Farmingdale, NY, USA). Both KDS-200 syringe pumps were used to regulate the flow of middle phase and outer phase fluid while the inner phase fluid was delivered via the NE-4000 syringe pump. For Design A, NE-1000 was used to deliver the middle phase fluid instead.

All the fluids were loaded individually into their respective inlets through polytetrafluoroethylene (PTFE) tubing with an outer diameter of 1/16" (Omnifit® Labware, Diba Industries Ltd., Cambridge, UK), delivered by syringe pumps (Model KDS-200, KD Scientific Inc., Holliston, MA, USA and NE-4000, New Era Pump Systems Inc., Farmingdale, NY, USA). The process of the droplet manipulation was recorded using a monochrome high-speed camera (Phantom Miro M110, Vision Research, Wayne, NJ, USA) mounted onto the light inverted microscope (Olympus IX51, Olympus Corporation, Tokyo, Japan), connected to a desktop (Figure 4-1). The recording duration for each video was 12.5s at a frame rate of 400 pps. The droplet images were extracted from the videos for size distribution analysis via an image analysis software—ImageJ (1.50i, National Institutes of Health, Bethesda, MD, USA). Experiments were repeated for result accuracy.

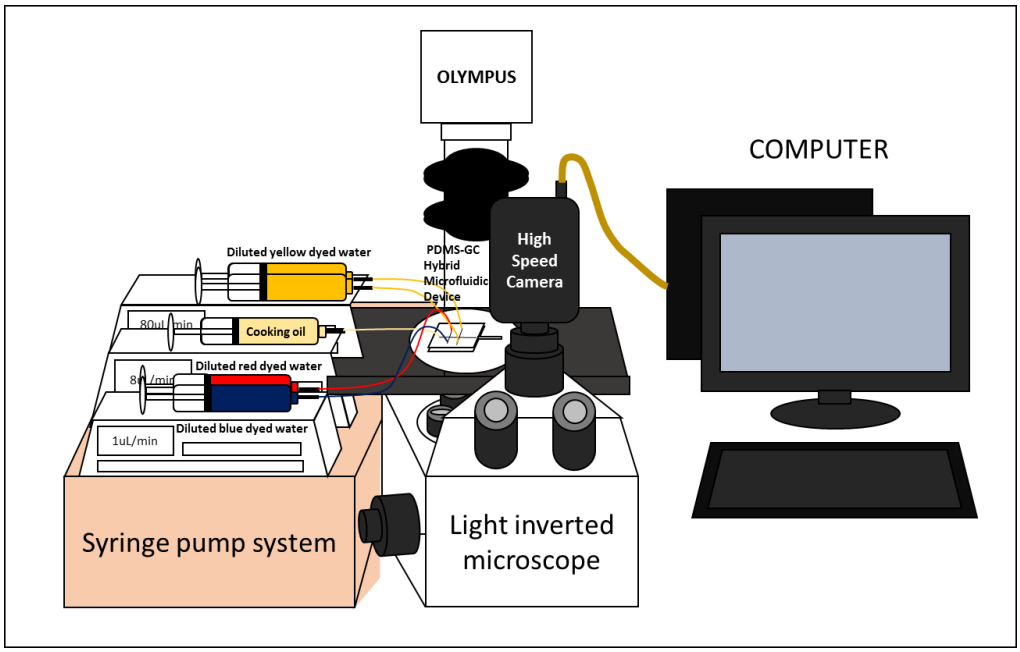

Figure 4-1. Schematic diagram for experimental setup

4.4 Measurement of Fluid Properties

This section summarised the properties of the fluid used in experiment, with DI water act as control for all aqueous dye. The subsection described the measurement method for each fluid properties and the equipment used. Table 4-1 summarised all the measured fluid properties.

Table 4-1. Summary of the fluid properties used in experiment analysis.

Fluid Properties @ 25˚C	**Contact Angle [°]**	**Viscosity, μ [mPa.s]**	**Density, ρ [g/cm^3]**	**Interfacial tension, γ [mN/m]**	
				cooking oil	**diluted yellow dye**
DI water	102.48	1.00 (theoretical)	1.0000	14.26	NA
Cooking oil	42.95	62.70	0.9092	-	11.03
Diluted red dye	102.45	1.60	0.9975	8.70	-
Diluted blue dye	97.87	1.50	0.9946	9.80	-
Diluted yellow dye	105.87	1.10	0.9992	9.70	-

4.4.1 Fluid Contact Angle Measurement

The contact angle for all the diluted dyes were measured on a blank PDMS layer using goniometer (250 – F1, ramé – hart instrumental co, Succasunna, NJ, USA). Each fluid was dropped gently on the surface of the blank PDMS layer to avoid deformation of the droplet. Blank DI water was used as a reference standard material to verify the effect of food dye towards the properties of DI water. The contact angle of the cooking oil on the PDMS layer was also measured as a comparison for the hydrophilicity and hydrophobicity of the fluids. The contact angle was measured as shown in Appendix A.1.

4.4.2 Fluid Viscosity Measurement

The viscosity of each fluid was measured with viscometer (DV-II+ Pro, Brookfield Engineering Laboratories, Inc., Middleboro, MA, USA) using the Cone/ Plate viscometer set-up. Cone Spindle CPE-41 was used for the Newtonian fluid measurement. The cone spindle was rotated 5 times before actual viscosity reading was taken. The viscosity of the Newtonian fluid was constant regardless of the different shear rates applied, thus a linear graph of the shear stress versus shear rate was obtained with the gradient calculated as the viscosity. The viscosity was measured as shown in Appendix A.2

4.4.3 Fluid Density Measurement

The density of each fluid was measured with the density meter (DMA 4500 M, Anton Paar, St Albans, United Kingdom). The density meter has a measuring range from 0 to 3 g/cm^3 with an accuracy up to 0.00005 g/cm^3. Each fluid was injected into the density meter individually for automatically measurement. The tube of the density meter was cleaned with ethanol and dried with air before and after a fluid was injected to prevent contamination. DI water was used as a reference standard material to ensure minimum effect of the food dye towards the properties of DI water.

4.4.4 Fluid Interfacial Tension Measurement

The interfacial tension of each fluid was measured by the ramé – hart goniometer. Surface tension – pendant method was chosen to measure the interfacial tension of the respective diluted dyes in the cooking oil and cooking oil in the diluted yellow dye. The aqueous fluid was injected into the organic external phase via syringes until a pendant shape droplet was observed and inverted pendant droplet for the organic fluid in the aqueous external phase. The total number of measurement was set to 10 with 5 seconds interval. The measurements were carried out 5 times for each fluid and the average value was calculated for result accuracy purposes.

4.5 Numerical Data of Experimental Parameter

4.5.1 Superficial Velocity, v_{sp}

Since the capillary tube acted as a collection tube for all fluid, the comparisons between v_{sp} and $v_{measured}$ was done at the downstream of the Design A during the preliminary work. The $v_{measured}$ can only be measured and calculated with the aid of the droplets as the indicator of the flow. The distance travelled of the droplets along the capillary tube at a fixed duration/ number of frames were measured then calculated with the formula $v_{measured} = distance\ travelled/time$. The hybrid microfluidic system was divided into two parts, i.e. upstream for droplet generation and downstream for droplet encapsulation. The v_{sp} of the continuous phase for both upstream and downstream i.e. cooking oil and diluted yellow dye was calculated and tabulated in Table 4-2 with the measured velocity, $v_{measured}$.

Table 4-2. Superficial velocity, v_{sp} versus measured velocity, $v_{measured}$ for Design A

Channel	Volumetric flow rate, Q		v_{sp}	$v_{measured}$	Percentage error
	[µL/min]	[mm³/s]	[mm/s]	[mm/s]	%
Cooking oil	12	0.2	5.00	-	-
Diluted red and blue dye	1	0.017	0.56	-	-
Diluted yellow dye	40	0.667	3.92	-	-
Capillary tube*	74	1.233	4.74	4.41	7.0
	90	1.500	5.78	4.96	14.0
	94	1.567	6.03	5.46	9.5
	98	1.633	6.28	5.74	8.6
	114	1.900	7.31	6.81	6.7
	134	2.233	8.59	8.09	5.8
*The flow rate of the capillary tube is equivalent to the total flow rate in the system with different loading of diluted yellow dye i.e. 30 µL/min, 38 µL/min, 40 µL/min, 50 µL/min and 60 µL/min.					

The percentage error was calculated based on the v_{sp}. In general, $v_{measured}$ has a lower value when compared to v_{sp} due to the pressure loss during the transport of fluid from the syringe pumps to the microfluidic device via PTFE tube. On top of that, syringe pumps are known to be a common source of flow rate fluctuations [110] and thus explained the error range of 5.8-14% indicating flow variation. The difference between the v_{sp} and $v_{measured}$ were mostly maintained constantly at ±0.5 except at total flow rate of 74 and 90µL/min (Table 4-2) due to the fluctuation. The constant difference validated the consistent performance of the syringe pumps and hence, the work involving calculation utilised v_{sp} to better quantify the experimental results.

4.5.2 Capillary Number (*Ca*), Flow Regime and Flow Ratio, φ

In this research work, *Ca* was used to determine the flow regime and characterise the flow at the downstream of the device where droplet encapsulation occurs. The *Ca*, *φ* and

the flow regime of the respective design were calculated. The encapsulation experiment was carried out with different flow rate ratio i.e. inner phase volumetric flow rate: middle phase volumetric flow rate: outer phase volumetric flow rate for different design.

Table 4-3. Ca_{total} of the droplet generation and encapsulation with the respective flow regime (Design A).

Device Upstream			
Flow rate ratio	***Ca***	**Flow Regime**	***φ*** **(Qd/Qc)**
1:12:38	3.17×10^{-2}	Dripping	2/12 = 0.167
1:12:40	3.17×10^{-2}	Dripping	2/12 = 0.167
1:12:42	3.17×10^{-2}	Dripping	2/12 = 0.167
1:12:50	3.17×10^{-2}	Dripping	2/12 = 0.167
1:12:60	3.17×10^{-2}	Dripping	2/12 = 0.167
Device Downstream			
Flow rate ratio	Ca_{total}	**Flow Regime**	φ_{total} **(Qd/Qc)**
1:12:38	3.22×10^{-2}	Squeezing	14/76 = 0.184
1:12:40	3.36×10^{-2}	Squeezing	14/80 = 0.175
1:12:42	3.50×10^{-2}	Squeezing	14/84 = 0.167
1:12:50	4.07×10^{-2}	Squeezing	14/100 = 0.140
1:12:60	4.79×10^{-2}	Squeezing	14/120 = 0.117

Figure 4-2a shows the droplet generation in the dripping regime with *Ca* of 3.17×10^{-2} and φ of 0.167 for Device A. The pinching of the inner droplets occurs at the downstream of the cross-junction corner due to the shear force from the middle phase continuous fluid and the build-up pressure due to the partial blockage at the main channel [111]. The inner droplets generated as plug due to the compressed channel height. Once the inner droplets flow into the glass capillary tube with larger height dimension, the droplet shape transforms from a 2D pancake shape to a 3D spherical droplet as shown in Figure 4-2b. The droplets encapsulated at the downstream in the squeezing regime. However, the pinching point move further downwards to the outlet of the glass capillary tube due to the

low Ca_{total}. The size of the W/O/W double emulsion droplets was constraint by the inner diameter of the glass capillary tube.

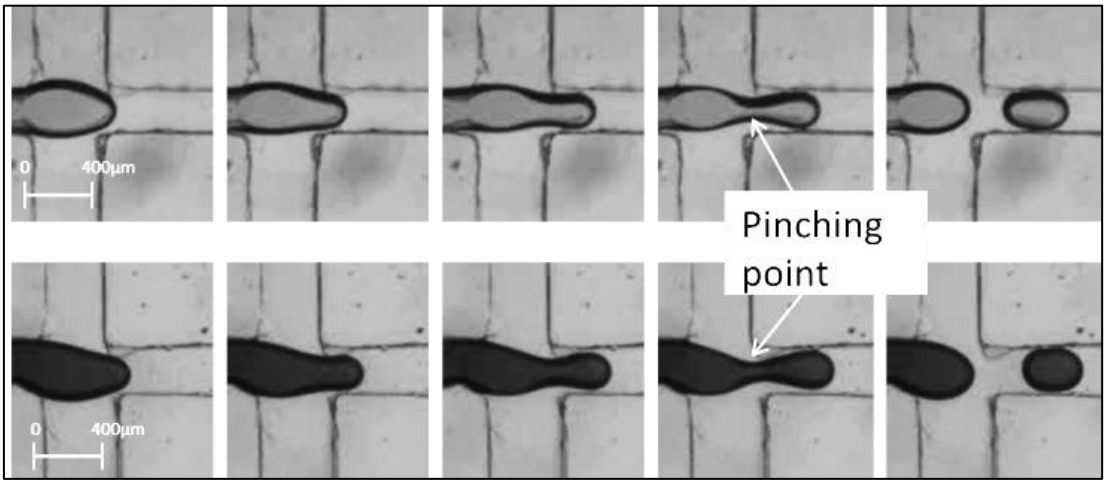

(a)

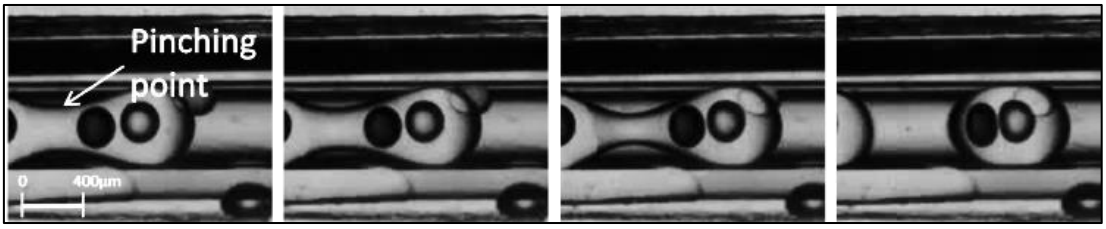

(b)

Figure 4-2. (a) Diluted red and blue dye breakup at the downstream of cross-junction corner due to the shearing of the middle continuous phase. Each image was taken at 50ms interval. (b) The W/O emulsion streams slowly fill up the glass capillary with pinching point occur towards the downstream of the device due to smaller $Ca_{total.}$

4.6 Image Analysis

4.6.1 Thresholding Method in Image Analysis

Image analysis extracts information from digital images obtained from the experimental work. The image processing method greatly affects the droplet analysis as it involves the measurement of the pixels – picture elements constructing the digital images. The pixels are usually organised in an ordered rectangular array, represented by M x N matrix with an intensity value that define its gradient. For an 8-bit grayscale image, the maximum value would be $2^8 = 256$, and hence, the lightest pixels yield 256 values,

producing a white pixel, whereas 0 value representing no intensity, referring to a black pixel.

Thresholding, a type of image segmentation method to create binary images from a grayscale image for information extraction, was used to process the droplet images captured by the monochrome high-speed camera. Ideally, the histogram of the pixel intensities distribution will present a deep and sharp valley between two peaks distinguishing the object of interest and background respectively. However, in real case, the distribution of the histogram shows flat and broad valley without a distinct thresholding value that clearly defines between both. Hence, selection of an adequate threshold is crucial to allow sharp differentiation between the concerned object and the background for accurate extraction. Image pre-processing such as cropping, and brightness adjustment is critical in this case to eliminate the background noise during the threshold selection.

To overcome the limitations of broad histogram distribution, several algorithms have been proposed to modify the histogram by utilising the information concerning the neighbouring pixels in the original picture. Some even deals with the grey-level histogram directly through parametric techniques, however, most of these proposed methods were unable to evaluate the "goodness" of threshold. Hence, Nobuyuki Otsu [112] derived an optimal thresholding method to establish an appropriate criterion for the optimum threshold evaluation. Following that, J. Kittler and J. Illingworth [113] derived an algorithm to solve the minimum error thresholding problem. Since then, Nobuyuki Otsu's thresholding and minimum error thresholding have been the most well-known and widely applied algorithm, often used as comparisons to other new proposed thresholding method.

In this research work, a “try-all” built-in function of the ImageJ was employed to allow one-step comparisons, then adapt the algorithm which provide a clear droplet outline. The default thresholding in ImageJ derived from a variation of the IsoData algorithm. The thresholding value was defined by the mean value of the average between the object and background, then refine through successive iterations. Before thresholding, the images extracted from the videos were processed to ensure constant brightness and contrast before analysing with ImageJ. Thresholding method rely on the lighting effect and intensity to differentiate the object from the background, hence image pre-processing is essential as it affects the measurement outcome. Since the image was taken from the microfluidic device directly from the microscopic stage, the region of interest (ROI) for upstream and downstream droplets were set constant to ensure consistent lighting from the microscope. Figure 4-3(a) shows the pre-processed image extracted from the video while Figure 4-3(b) – (e) shows the processed image for each respective droplet. As shown in Figure 4-3(a), the inner droplets were in plug shape (2D pancake shape) constraint by the channel height, then transformed to 3D spherical droplet when entering the glass capillary tube. Hence, for consistency and simplicity, the inner droplets were all measured at the upstream.

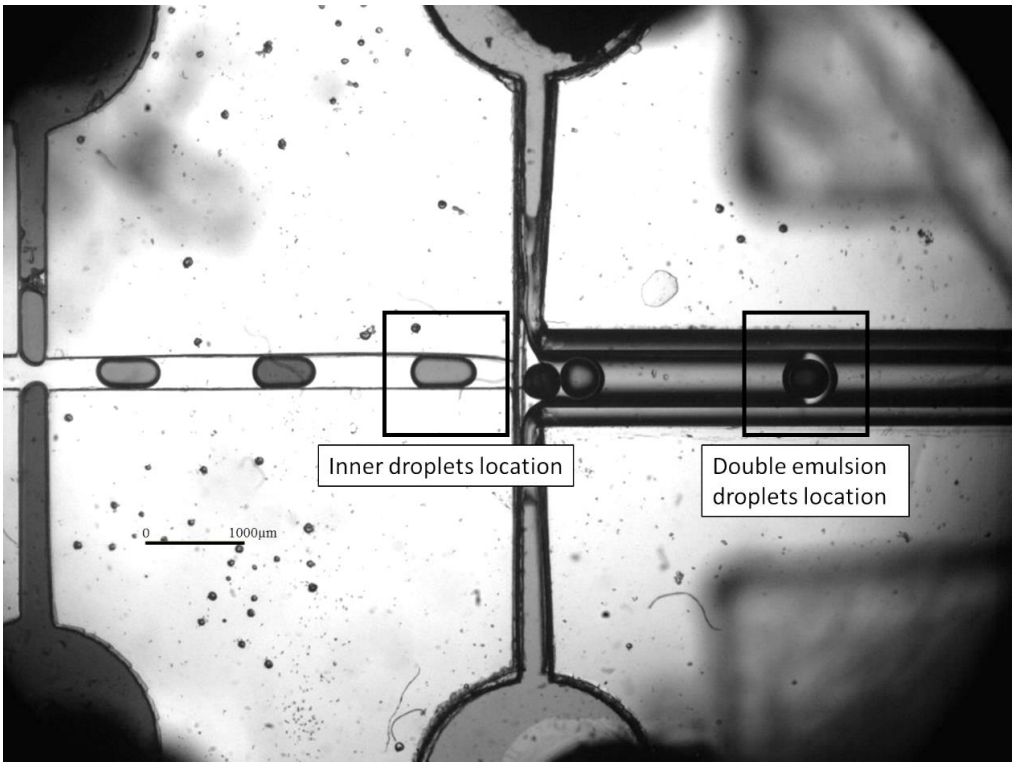

(a)

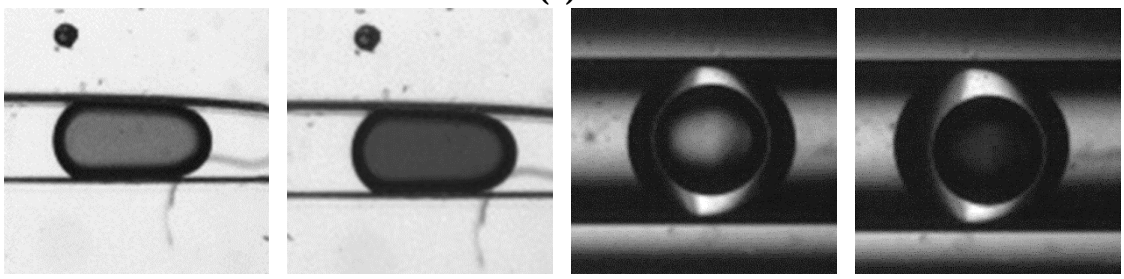

(b) **(c)** **(d)** **(e)**

Figure 4-3. (a) Pre-processed image extracted from the video. The location of the droplets was fixed in the region of interest (red box) before the video was paused for image extraction. This ensures consistent brightness and contrast of the droplets affected by the distance of light source. (b) Processed image of inner red droplet. (c) Processed image of inner blue droplet. (d) Processed image of downstream double emulsion droplet with inner red encapsulation. (e) Processed image of downstream double emulsion droplet with inner blue encapsulation.

To illustrate the importance of image processing, the output of the thresholded pre-processed (Figure 4-4a) and processed images (Figure 4-4b) were presented. Before individual droplets were cropped, the software could not identify clearly which is the object and which is the background, hence the rough interface at the droplets especially at the downstream. 'Triangle' algorithm even showed overbrightness due to unidentified object.

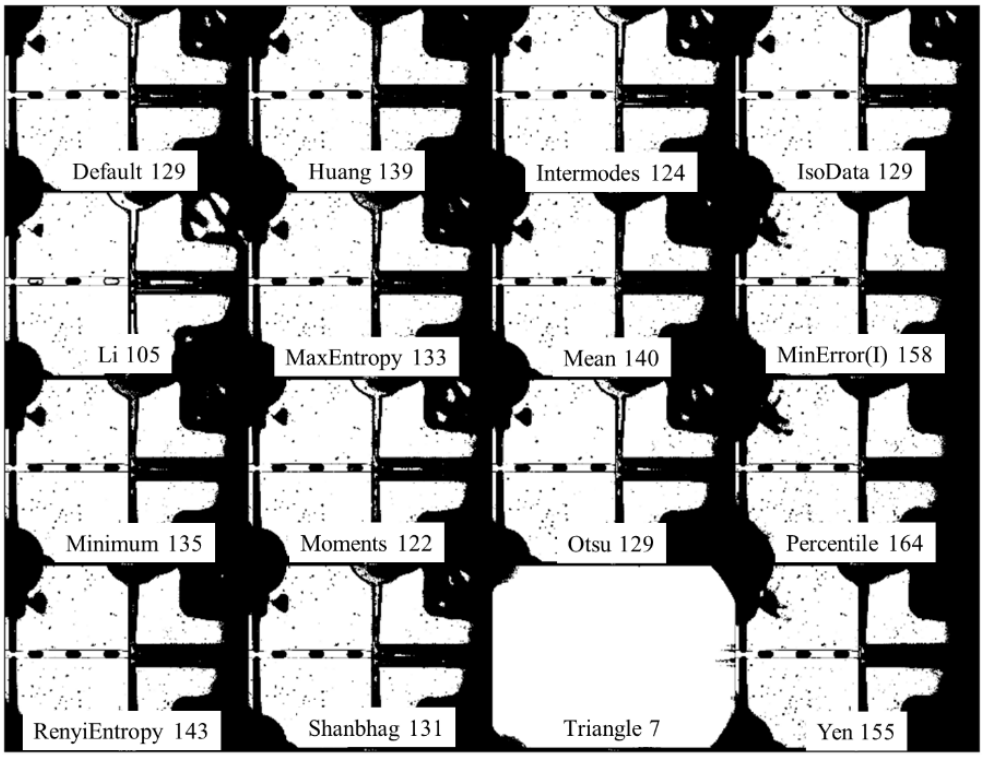

(a)

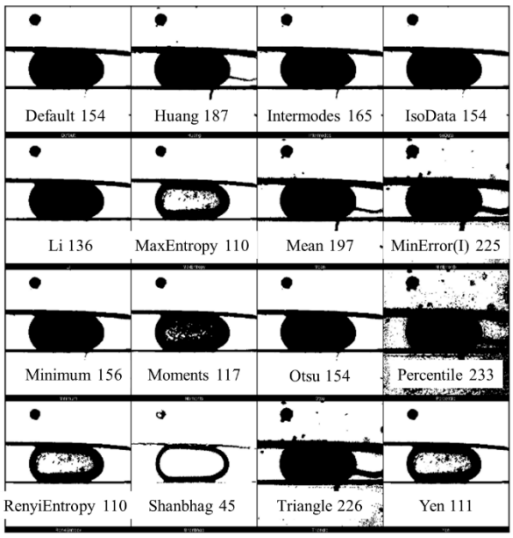

(b)

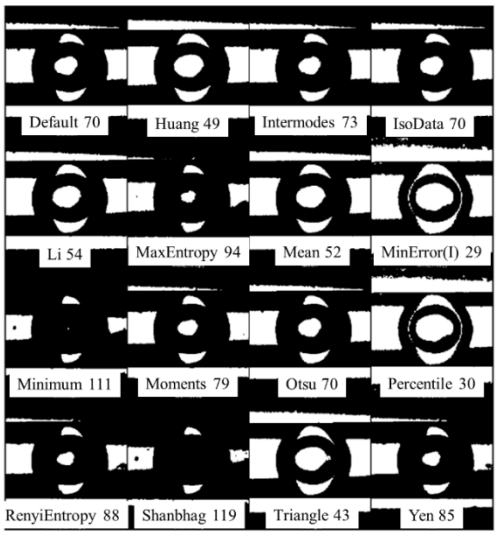

(d)

Figure 4-4. Montage of different thresholding methods with their selected threshold value. (a) Pre-processed image with a lot hardly distinguishable object and background due to the disturbance. (b) Processed image of inner red droplet. (c) Processed image of downstream double emulsion droplet with inner red encapsulation.

Figure 4-4b and Figure 4-4c shows the output of the processed images. Since the unwanted background was cropped, the identification of droplet as an object is clearer. At different algorithm, the defined thresholding value is different even for the same image. Since the best fit thresholding value were directly affected by the intensity of the

pixels, the consistency of the lighting was maintained by fixing the parameters related to lighting such as the brightness of the microscope lighting, the distance between the light source and the PGHD as well as the ROI. Through the “try all” function, the outputs with different threshold values can be obtained for clear comparisons which algorithm is more suitable in differentiating the object i.e. droplets and the background i.e. channel wall clearly. Referring to Figure 4-4b and Figure 4-4c, Shanbhag thresholding method (value = 45) was chosen to analyse the inner droplet whereas Triangle thresholding method (value = 43) was chosen to analyse the double emulsion droplet. The outline of the droplets was extracted using the “analyse particle” function in ImageJ.

The measurement of the droplet size depends on the area of each pixel and thus calibration was required to obtain the scale under different magnification. In this research work, the magnification of the objective lens used was 2X, whereas the magnification of the eye piece was 10X and hence the total magnification given was 20X, whereas, the images extracted from the high-speed camera remain alike to the magnification of the objective lens. Using the same magnification, and image of the calibration ruler was captured and measured to obtain the number of pixels in a known distance. The pixel to distance ratio (1:10) was input into the ImageJ software before the measurement and hence the remaining measurement were all presented in μm.

Before thresholding method was used, the diameter of the droplets was measured using the “straight-line” function in ImageJ. Therefore, only the maximum length of the droplets was measured as the diameter. Design A1 onwards, thresholding method replaced the straight-line measurement to measure the Feret diameter of the oblong droplet. Feret diameter measures the distance between two parallel tangents of the object at an arbitrary angle. In ImageJ, Feret diameter also known as the maximum calliper,

measuring the longest distance along the selection boundary. The shortest distance was displayed as minimum Feret. Measurement was done automatically by the software, avoiding the strong dependence on the individual judgement.

4.7 Preliminary Experimental Results (Design A)

The preliminary work aimed to demonstrate the practicability of the PGHD in a range of flow ratio. The observations and experimental data obtained were useful in understanding the flow and droplet behaviour to improve the design of the PGHD and the experimental SOP. As mentioned, Design A was carried out with pre-optimised SOP. The inner flow rate of the diluted red and blue dyes was fix at 1µL/min, whereas the middle continuous flow rate was tested with 12 µL/min assuming even flow i.e. 3 µL/min for each bifurcated channel. The inner and middle flow rate was fixed at 1 µL/min and 12 µL/min after the successful formation of the inner droplets. The outer aqueous flow rate manipulated within the range of 40 – 60 µL/min. Highest number of distinct droplets encapsulation was shown at 40 µL/min, hence, 38 µL/min and 42 µL/min were tested for further verification. The experimental data was analysed and presented as below.

4.7.1 Success Rate vs Flow rate and Capillary Number

By fixing the total upstream flow rate at 14 µL/min, the outer aqueous flow rate was manipulated between 40, 50 and 60 µL/min. Hence, the total flow rate of 94, 114 and 134 µL/min as shown in Figure 4-5. Referring to the initial inspiration i.e. to generate double emulsion droplets for microreactor purpose, success rate of the W/O/W droplets encapsulation was calculated based on the encapsulation of two distinct droplets (Equation 16). Figure 4-5 shows the success rate comparing between 1st and 2nd attempt.

$$\boldsymbol{Success\ Rate} = \frac{\boldsymbol{N_{RB}}}{\boldsymbol{N_{total}}} \times \mathbf{100\%} \qquad \textbf{Equation 16}$$

where N_{RB} = number of two distinct droplets encapsulation; N_{total} = total number of encapsulated droplets

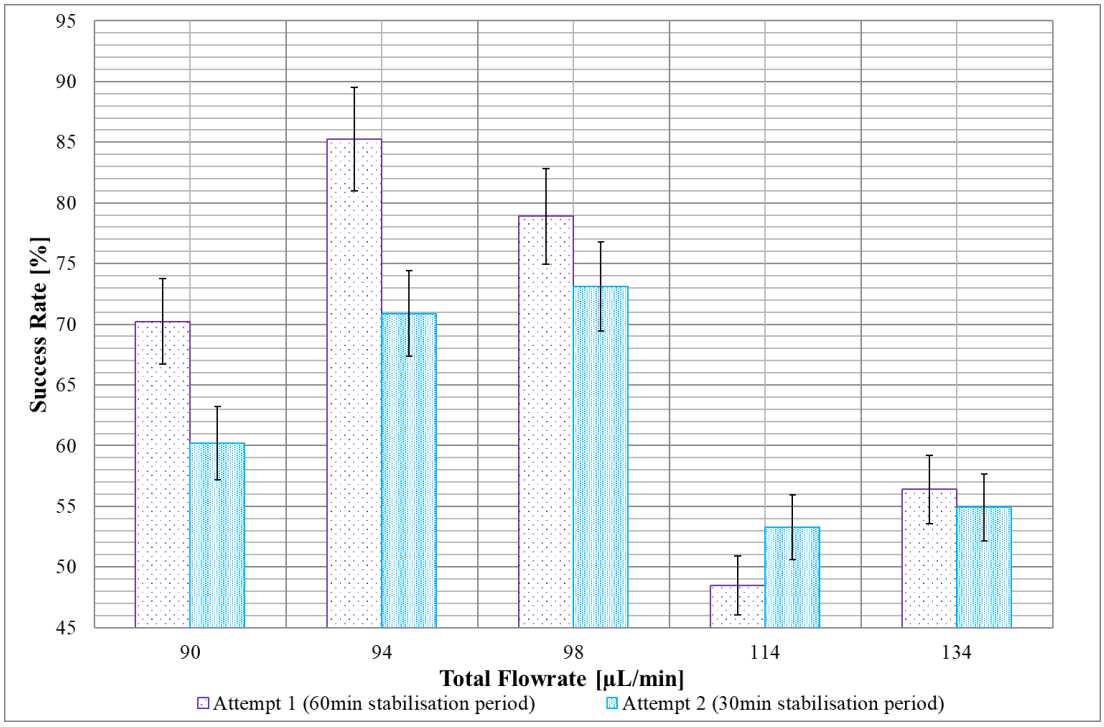

Figure 4-5. Graph of success rate versus total flow rate for Device A.

The success rate was highest at 40(94) µL/min then drastically reduced when the outer aqueous flowrate was increased to 50(114) µL/min. Since the upstream flow rate was remained constant, the increasing diluted yellow dye flow rate increases the shearing rate at the downstream. Hence, increasing the number of single droplet encapsulation. For further verification, the outer aqueous flow rate was set as 38(90) µL/min and 42(98) µL/min. The experiment was then carried out second time for all flowrate to see the repetition. However, before optimisation, the device failure rate was high due to the external factors such as channel blockage and glass capillary tube contamination.

The presence of bifurcating channels resulted pressure built-up in the device leading to leakage near the device inlet and liquid backflow. After several trials, the experiment

was conducted at a shorter stability period (30min). Despite the shorter stability period, the success rate shows similar trend between 1st and 2nd attempt except at 42(98) µL/min where the success rate was slightly higher compared to 40(94) µL/min during 2nd attempt. This can be affected by the insufficient stability period or the system instability, where the actual reasons remains unknown due to the insufficient experimental data. This, however shows the essentiality to improve the design and experimental procedure for higher repeatability of the PGHD.

Although 2nd attempt shows higher success rate at 42(98) µL/min, however, the stabilisation period was shorter. To conclude, the success rate of two distinct droplets encapsulation is highest when the outer aqueous phase was set at 40 µL/min. Hence the optimum flow rate ratio at 1: 12: 40 µL/min.

4.7.2 Size Distribution and Droplet Volume

The droplet length was measured using the straight-line function, hence images were all enlarged/ zoomed in to 150% until the pixels outline were clear for manual measurement. The measuring position were made consistent at the middle of the droplet where maximum distance of the droplets was measured. In addition to that, the sample droplets were extracted after the encapsulation process took place and stabilised in the glass capillary tube at a constant ROI with sample size of 40 droplets. Figure 4-6 below shows the size distribution curve of the W/O emulsion and W/O/W double emulsion droplets.

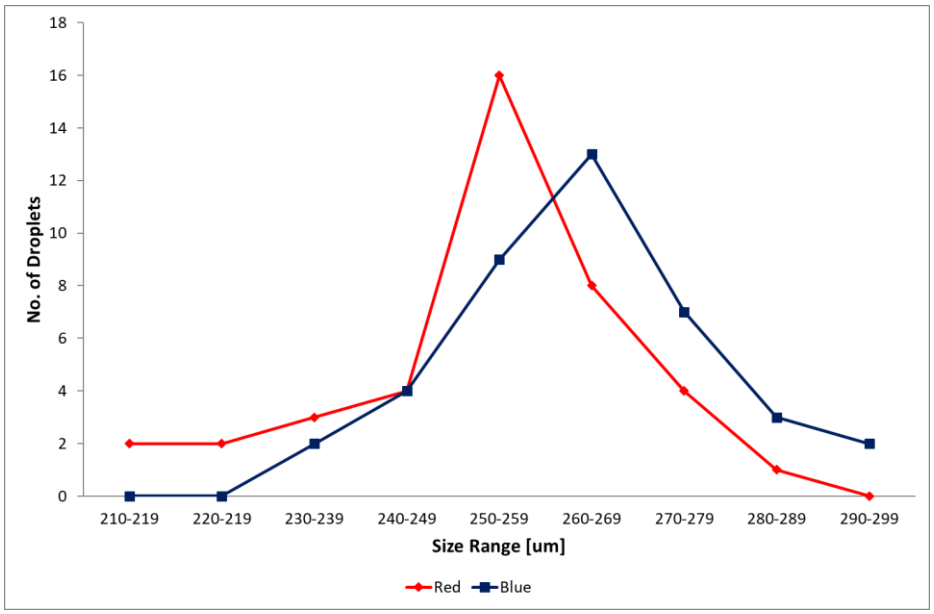

(a)

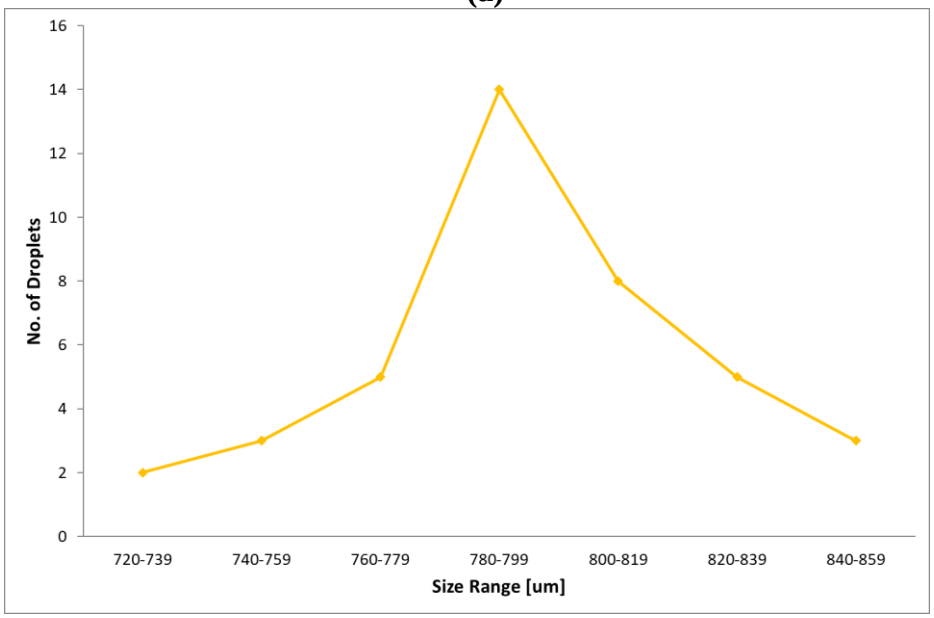

(b)

Figure 4-6. (a) Size distribution of inner red and blue droplets. (b) Size distribution of double emulsion droplet.

The bell-shaped droplet size distribution curve indicates normal distribution. The curve of inner blue droplets (Figure 4-6a) shift towards the right (larger droplet size), due to the inconsistent cooking oil flow from the bifurcated channel. Insufficient shear force caused by the pressure drop at 90° bend generates plug size droplets, even though the calculated *Ca* shows dripping regime at the upstream. The double emulsion droplets were generated in plug size, due to squeezing regime. Throughout the experimental work,

spinning of inner droplets was observed along the capillary tube due to the resulting acceleration of droplets during breaking.

4.7.3 Stability of Generated Double Emulsion

The stability of the generated double emulsion droplets was defined by the encapsulated inner droplets, if they coalescence with each other in the glass capillary tube. Since the length of the capillary tube is known, the residence time can be calculated using Equation 17. The analysis is essential to evaluate the necessity of the addition of surfactant. The calculated residence time for different flow rate was tabulated in Table 4-4.

$$t = \frac{L}{\vartheta_{measured}} \qquad \textbf{Equation 17}$$

where t = residence time [s]; L = length of the capillary tube [mm]; $\vartheta_{measured}$ = measured velocity [mm/s]

Table 4-4. Residence time of stable inner droplets at different flow rate.

Channel	Total Flow rate, Q		$\vartheta_{measured}$ [mm/s]	Residence time, t [s]
	[µL/min]	[mm^3/s]		
Capillary Tube	74	1.233	4.41	21.3
	90	1.500	4.96	18.9
	94	1.567	5.46	17.2
	98	1.633	5.74	16.4
	114	1.900	6.81	13.8
	134	2.233	8.09	11.6
*Length of the capillary tube = 9.4cm (94mm)				

The residence time is a reference of the minimum duration inner droplets stays steadily in the capillary tube, decreasing with increasing flow rate due to the higher velocity. The inner droplets remain stable at the collection plate unless external force applied to the petri dish (Figure 4-7). The main factor preventing the coalescence of the inner droplets

is the large shell area encapsulating the small inner droplets. Experimental observations show overlapping between the inner droplets as the double emulsion droplets travel, indicating the large shell volume. The coalescence of the inner droplets can be triggered when (1) both inner droplets were flowing at the same path line intersecting with each other; (2) shell volume reduction, either by increasing number or size of inner droplets; as observed in the later experimental work with different channel design.

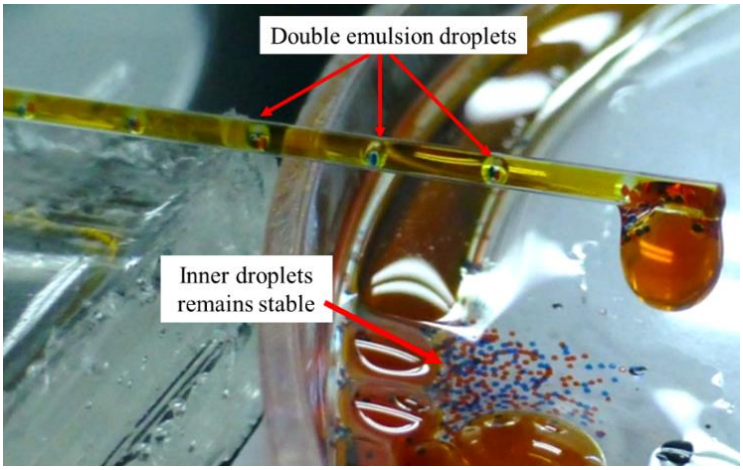

Figure 4-7. Image of double emulsion droplets travel in the glass capillary tube towards the petri dish.

4.8 Droplet Generation and Encapsulation in Design A1

Design A1 (Figure 4-8c) consists of two individual T-junction generating red (Figure 4-8a) and blue (Figure 4-8d) droplets independently, then converged by the stabilising channel (Figure 4-8b) and encapsulated in the glass capillary tube (Figure 4-8e).

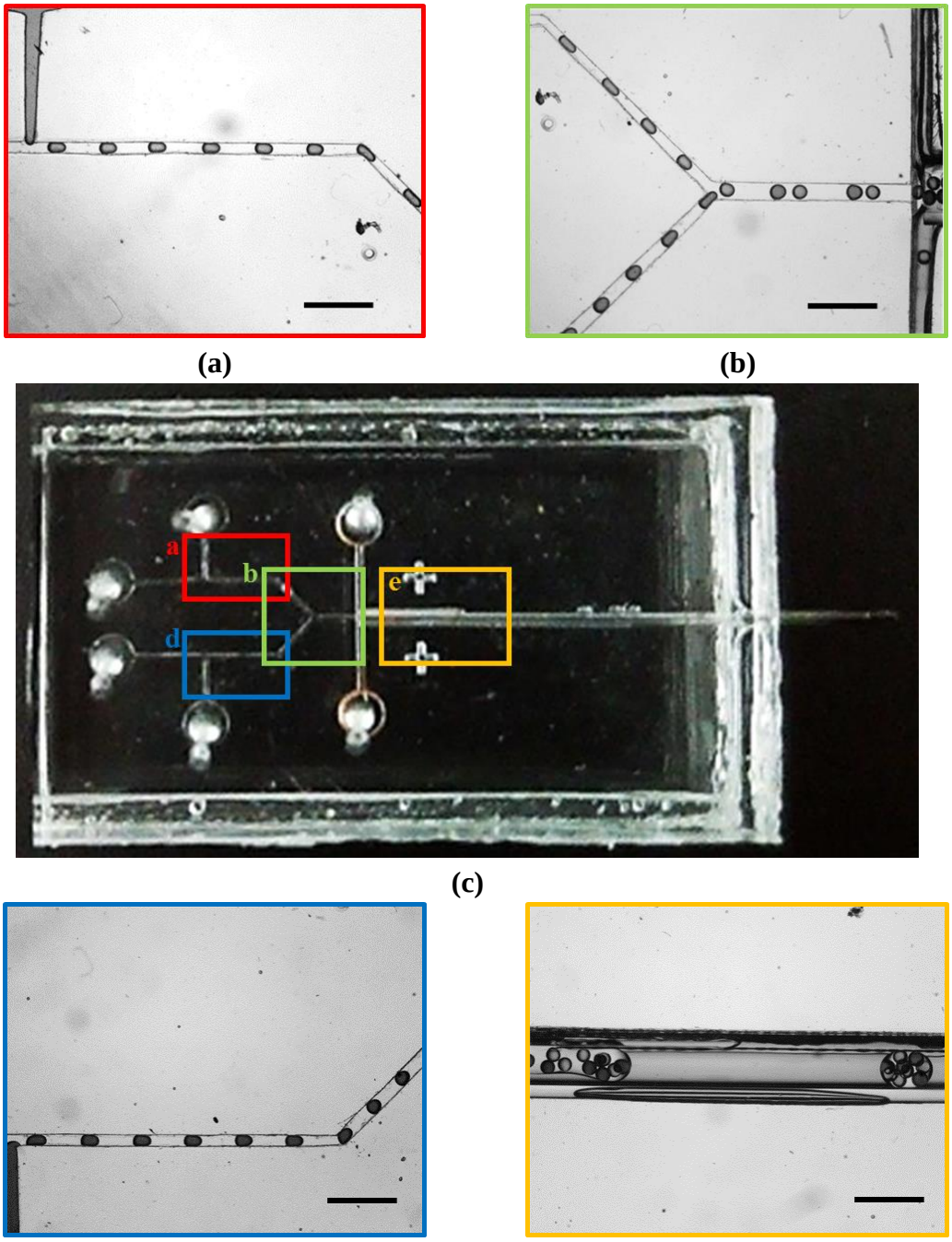

Figure 4-8. (a) Red droplets generated at T-junction. (b) Converged red and blue droplets at the stabilising channel. (c) PGHD-A1 with illustrated part. (d) Blue droplets generated at T-junction. (e) Double emulsion droplets generated at the glass capillary tube. All scale bars represent 1000 µm.

Figure 4-8 shows microscopic images of each droplets generated at their respective channel. The plug size inner droplets constraint by the microchannel dimension reduces into spherical shape when flowing into the wider stabilising channel. Experimental study

in Design A1 aimed to verify the microchannel geometry design, experimental parameter such as flow rate ratio and to understand the droplets flow mechanism for further optimisation. The experiments conducted can be categorised into three main groups, (1) to verify the geometry design; (2) to verify possible flow rate ratio for double emulsion droplet formation; (3) to verify the practicability of larger syringe volume allowed (Table 4-5). Each experimental work will be discussed further under Subsection 4.8.1 – 4.8.3.

Table 4-5: Summary of experiment objectives.

Experiment	Flow rate ratio [µL/min] (inner: middle: outer)	Syringe size [cc] (inner: middle: outer)	Aims
1	a. 1: 5: 40 b. 1: 5: 240	1: 5: 5	To verify the microchannel geometry design
2	1: 3: 40	1: 5: 5	To verify possible lower flow rate ratio for encapsulation
3	1: 3: 40	10: 10: 30	To verify the practicability of larger syringe volume.

4.8.1 Experiment 1 – Verification of microchannel geometry design

Two experiments were conducted using the same microfluidic device but different flow rate ratio. At 1st experiment, 1: 5: 40µL/min, the droplet encapsulation was successful during the stabilisation period. After the stabilisation period, the sealing at the reservoir of diluted blue dye starts to leak due to the improper placement of PTFE tube. The system was let settled, then restart with the same flow settings, but no evidence of encapsulation process after 1 ½ hour of stabilisation due to the pressure loss caused by the leakage at reservoir. The flow rate of the diluted yellow dye was increased to 240µL/min to built-up pressure at the downstream and achieve higher shear force. After 1 hour of stabilisation period, the system reached equilibrium, where double emulsion

droplets encapsulating only red droplets were observed. The diluted blue dye, unable to form inner droplets, accumulate at the reservoir and flows out from the damaged inlet (Figure 4-9a). At 2nd experiment, the breakup point was further from the glass capillary inlet due to the pressure loss at the upstream (Figure 4-9b). Experimental observations show practical device geometry design and hence Experiment2 was carried out to determine the possible flow rate ratio.

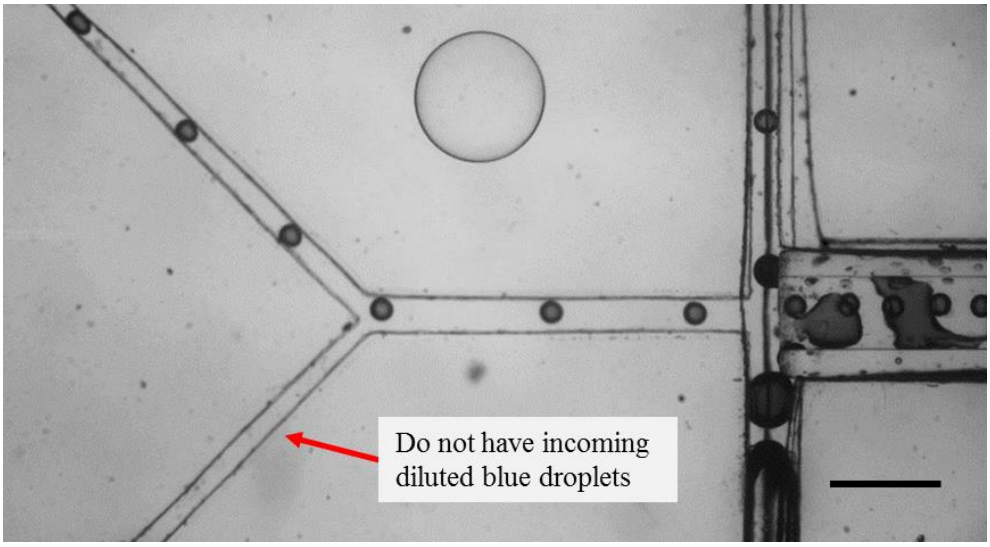

(a)

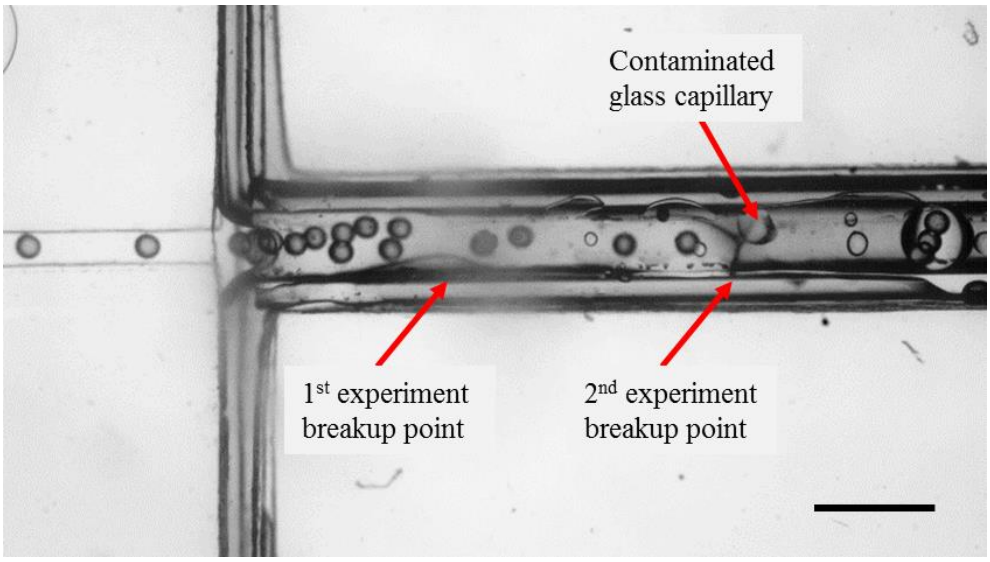

(b)

Figure 4-9. (a) Inner blue droplet unable to form due to the damaged diluted blue dye reservoir. (b) Breakup point for 1st experiment and 2nd experiment.

4.8.2 Experiment 2 – Verification on lower flow rate ratio for encapsulation

The cooking oil flow rate was decreased to 3µL/min with reference to Design A to verify possible lower flow rate. The total experiment duration including the stabilization period is approximately 2 ½ hours. Therefore, the syringe volume used in this experiment could not sustained throughout the experiment and required refilling in between. Slight change in the system was observed after the system was restore from refilling, despite the 1-hour stabilising period. Observations at pre-stabilised stages shows: (1) Occasional mixing of red and blue inner droplets at the stabilising channel. (2) Slightly longer plug when droplets first generated at the upstream. Besides, unstable flow was observed when syringe is approaching empty due to insufficient shear force and inconsistent pumping.

The feret diameter of the inner droplets was measured at the T-junction after it was generated and stabilised before entering the stabilising channel (Table 4-6). Supressed by the channel width, the plug size inner droplets relaxed into spherical shape when flow into the wider stabilising channel and maintained until it was encapsulated at the capillary tube. The size of the inner droplets was measured using the thresholding method whereas the double emulsion droplets generated in the capillary tube were measured using the straight-line method. This is because the encapsulation of multiple inner droplets further complicates the intensity range, limiting the thresholding value selection.

Table 4-6: The W/O emulsion and W/O/W double emulsion droplet size in their respective channel

Channel		**Average Feret Diameter/Length [µm]**	**Standard Deviation**	***CV* [%]**	**Sample Size [droplets]**
Red		212	8.53	4.0	20
Blue		204	5.29	2.6	20
Stabilising	Red	180	6.30	3.5	35
	Blue	188	9.39	5.0	35
Glass Capillary		780	13.33	1.7	25

At flow rate ratio of 1: 3: 40, the average size of the red and blue droplet are 212 µm and 204 µm respectively. The average size of the red and blue inner droplets reduced to 180 and 188 µm respectively when entering the stabilising channel due to the wider width of the stabilizing channel. The droplet size generated are smaller than Design A i.e. 266 µm. This is due to droplet shearing by independent cooking oil phase and no longer depend on the flow splitting ratio. The overall *CV* value were well below 5% indicating monodispersed except the inner blue droplets at the stabilising channelThe slightly higher polydispersity was caused by the instable flow when the liquid volume in the syringes are less than 1ml, explaining the high standard deviation value as well.

The unstable flow caused by the nearly empty syringes, leads to occasionally collision of the encapsulated inner droplets, which dispersed into the diluted yellow dye while flowing in the capillary tube (Figure 4-10). During the refilling, the whole system was paused. The flow inside the PGHD was not stagnant due to the pressure difference applied during the removal of syringes, resulting minor contamination in the capillary tube (Figure 4-11b). The air bubble induced during the refilling process leads to the segment break off, resetting the double emulsion droplets breakup distance (Figure 4-11), indicating the influence of the disturbance and importance of stabilising period.

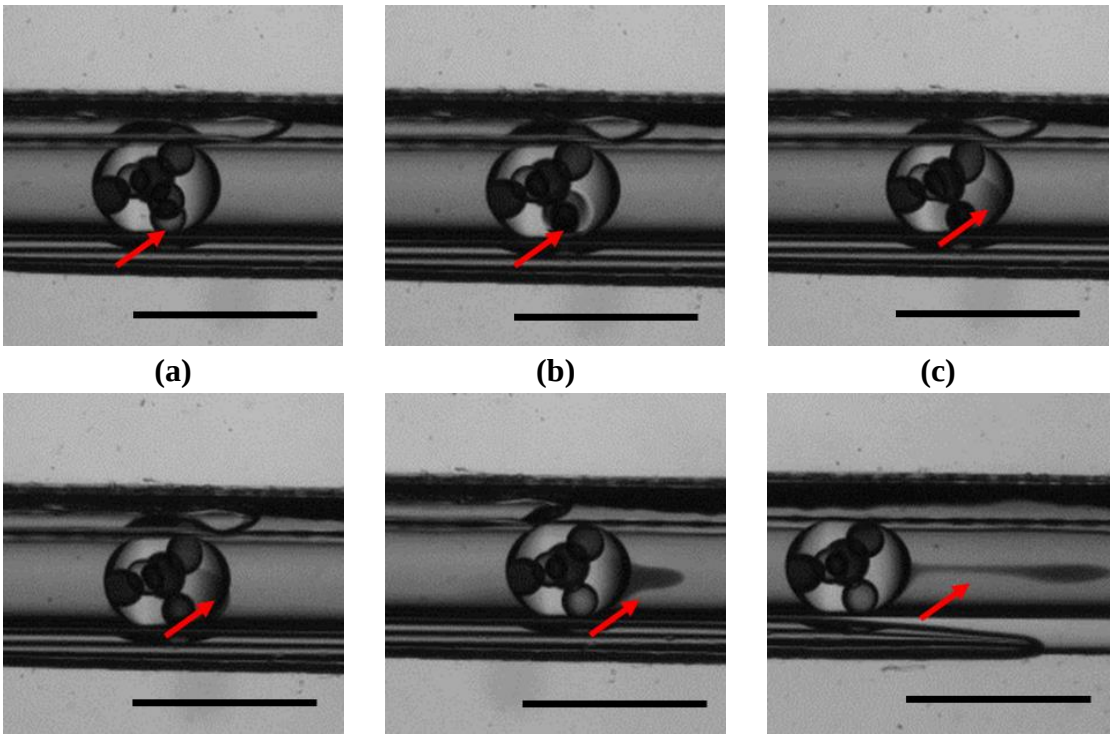

(a) (b) (c)

(d) (e) (f)

Figure 4-10. (a) Multi-encapsulated W/O/W double emulsion droplets before deformation. (b-f) Red inner droplets starts to deform and dispersed from the double emulsion droplets into the flowing diluted yellow dye. The remaining inner droplets remained encapsulated.

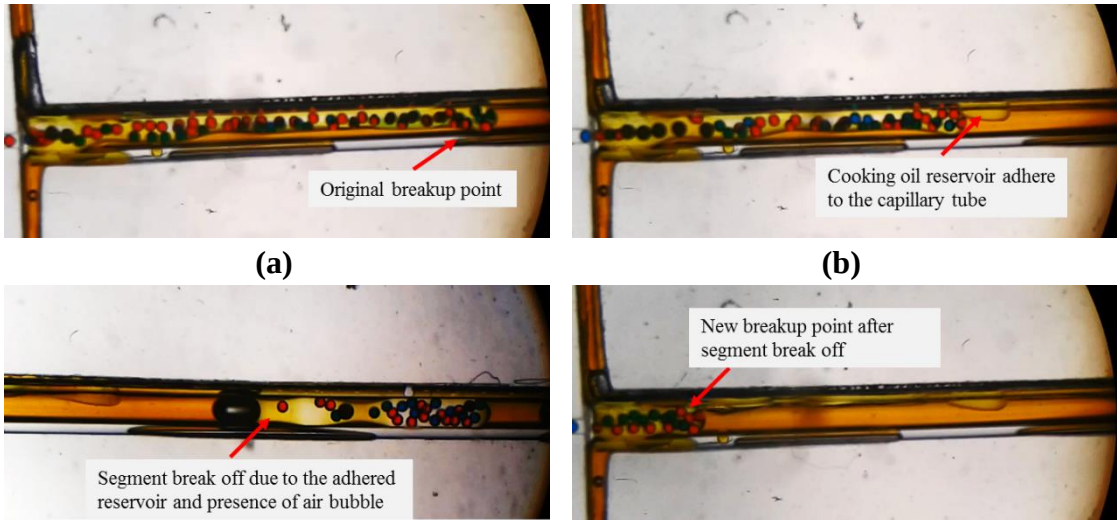

(a) (b)

(c) (d)

Figure 4-11(g) Original breakup point of the double emulsion droplets towards the downstream. (h-j) W/O/W segment break off due to the cooking oil reservoir and air bubble contributing a new breakup point.

The number of the encapsulated inner droplets were concluded in Figure 4-12 according to the sequence of three different videos taken. The average droplets encapsulated is 7-8 with standard deviation of 1.23. The inner blue droplets encapsulated

were generally lower than the inner red droplets, due to the unstable flow of the experiment. In addition, the recorded videos required an 8 minutes saving duration before the next video can be taken, hence possibility of miscount. The presence of mixed droplets in the experiment was considered as anomalous. Most of the time, red and blue droplets do not collide with each other although overlapping have occurred.

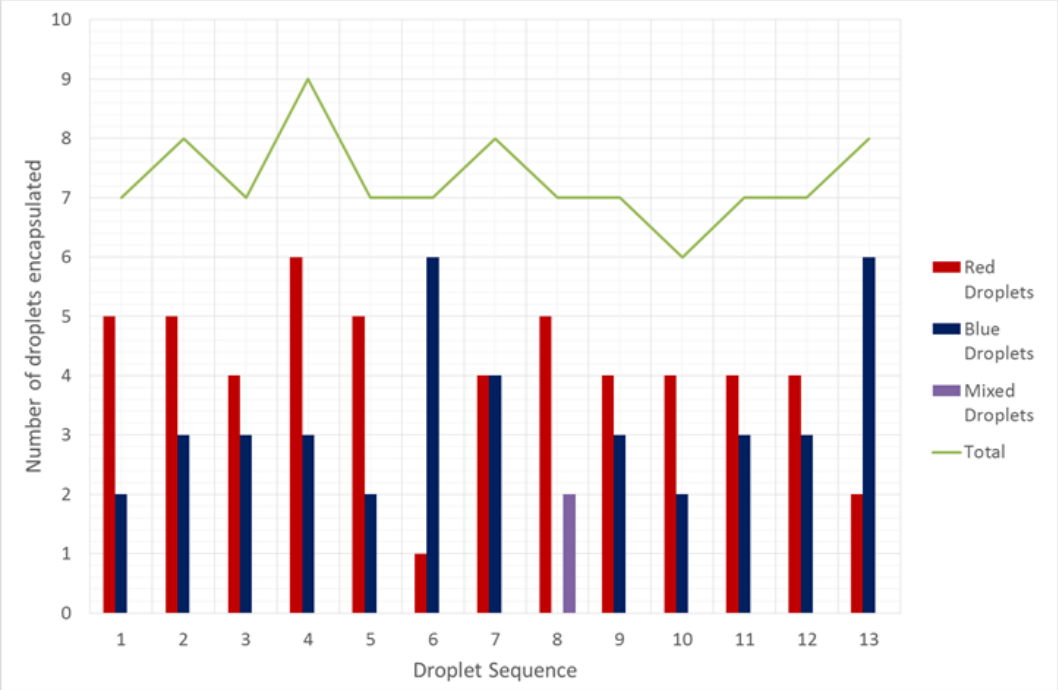

(a)

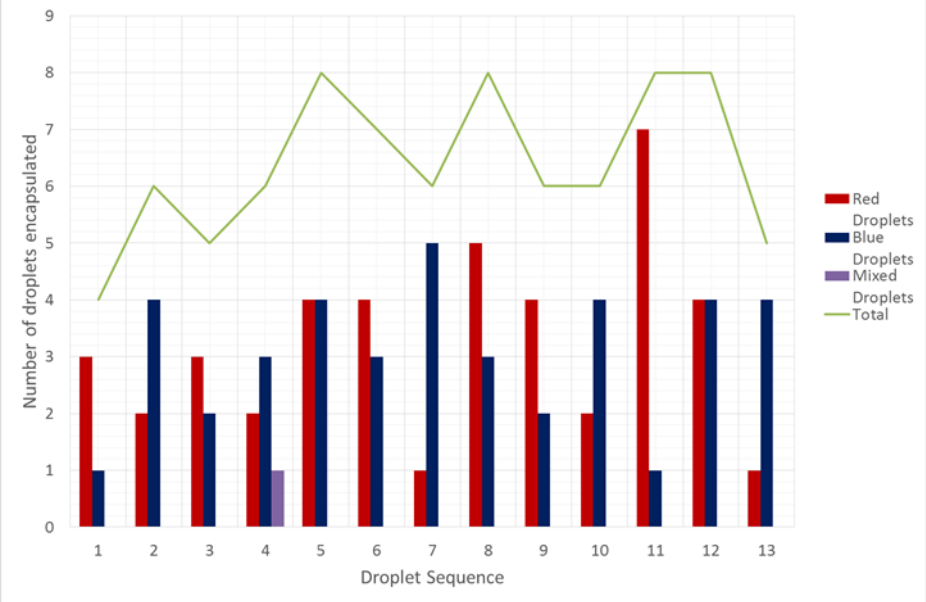

(b)

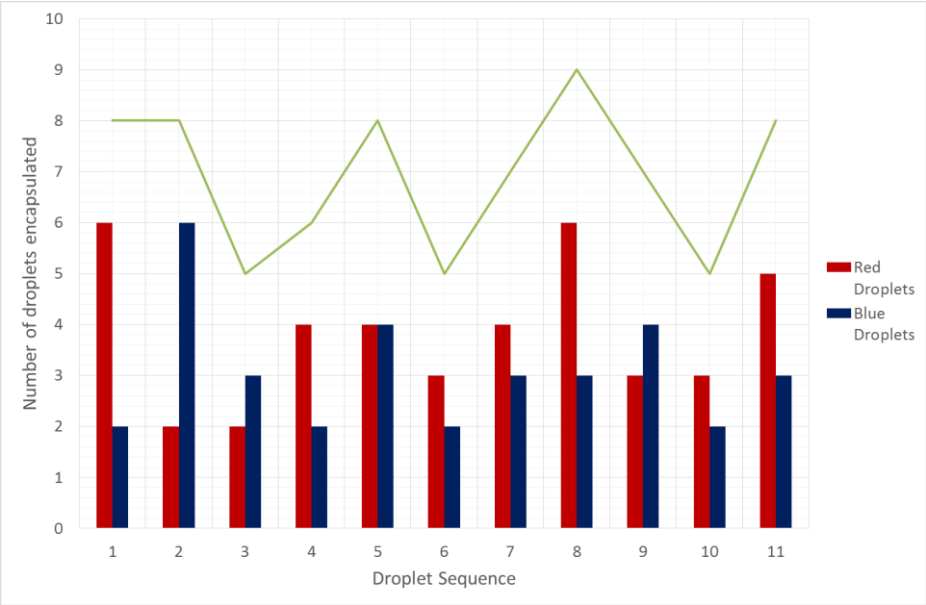

(c)

Figure 4-12. (a) Number of encapsulated droplets according to sequence – Video 1. (b) Number of encapsulated droplets according to sequence – Video 2. (c) Number of encapsulated droplets according to sequence – Video 3.

4.8.3 Experiment 3 – Practicability of large syringe volume

Previous experiments show disturbance caused by the syringe refilling, therefore the syringes used in this experiment were changed to the following specifications: diluted red dye, diluted blue dye and cooking oil syringes were upgraded to 10 mL, whereas the diluted yellow dye syringes were upgraded to 30 mL to avoid refilling in between the experiment, minimising interruption to the system. The flow rate ratio used is 1: 3: 40, the measured droplet size was tabulated in Table 4-7. The experimental data was compared with Experiment 2 (Figure 4-13).

Table 4-7: The droplet size in their respective channel

Channel		Average Feret Diameter/Length [μm]	Standard Deviation	*CV* [%]	Sample Size [droplets]
Red		217	9.70	4.5	20
Blue		218	9.67	4.4	20
Stabilizing	Red	177	8.5	4.8	35
	Blue	182	6.87	3.8	35
Glass Capillary		774	15.65	2.0	25

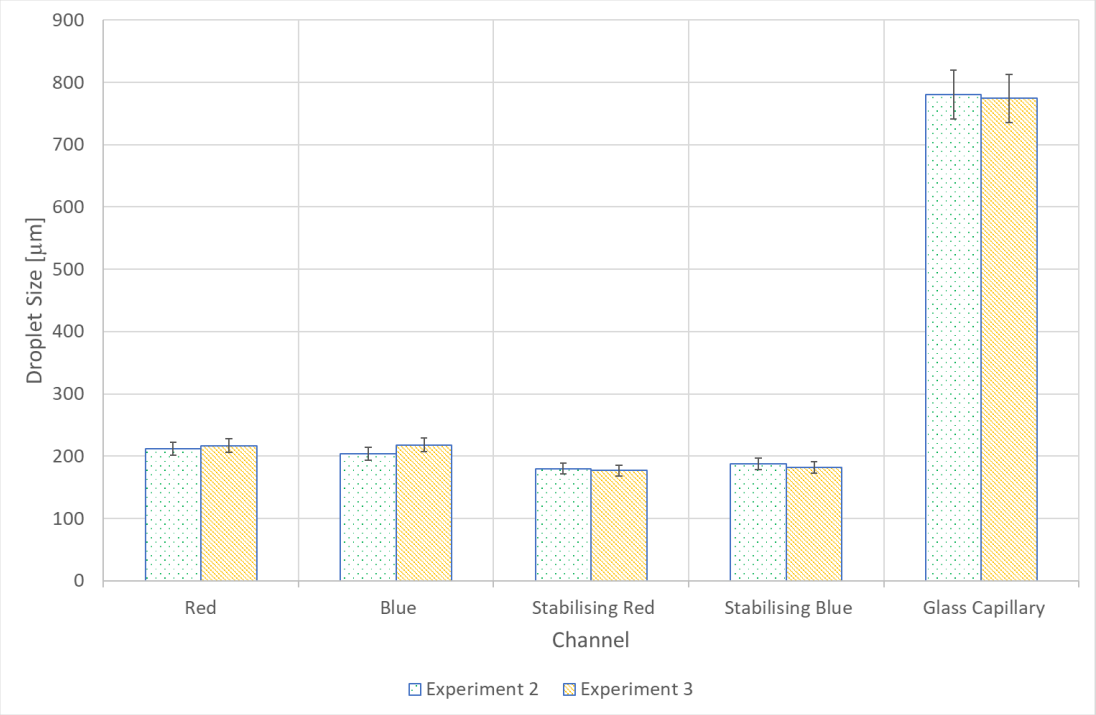

Figure 4-13. Droplet size comparison graph of experiment 2 and experiment 3.

The hybrid system used in experiment 3 was a different device made from the identical mould as experiment 2. The minimum difference between the droplet sizes of both experiments indicating the consistency of the syringe pumps and the hybrid system. Most of the time, the inner droplets generated in the upstream enter the stabilising channel alternatively. The wider stabilising channel slows down the inner droplets pairing them in alternate sequence. The sequence, however was disrupted when entering the capillary tube, further slow down by the larger tube dimension. Both inner droplets entered the stabilising channel simultaneously, instead, rotation and overtaking were observed, altering the colour sequence i.e. red-blue or blue-red (Figure 4-14). The average number of encapsulated inner droplets was 7 droplets with maximum and minimum of 9 and 4 droplets respectively, consistent to experiment 2.

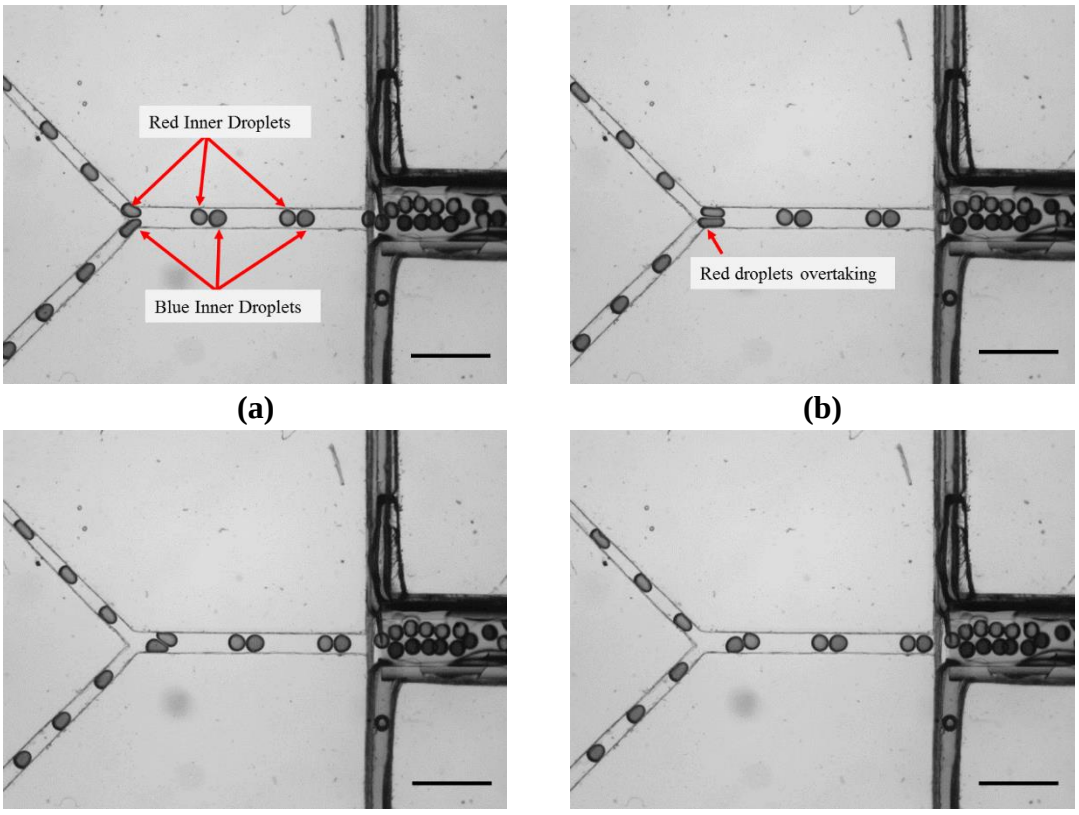

Figure 4-14. (a) Red and blue inner droplets entering the stabilising channel simultaneously. The initial droplet sequence in stabilising channel was blue-red. (b-c) Red inner droplet overtaking the blue inner droplet at the entrance of stabilising channel. (d) The droplet sequence altered to red-blue after the overtaking.

Table 4-8 summarised the design criteria and the objectives including the experimental results of Design A to Design A1b.

Table 4-8: Overview of the transformation of channel geometry design

<table>
<tr><td colspan="5">Labels: a. cooking oil inlet; b. diluted blue dye inlet; c. diluted red dye inlet; d. diluted yellow dye inlet</td></tr>
<tr><td>Design</td><td> 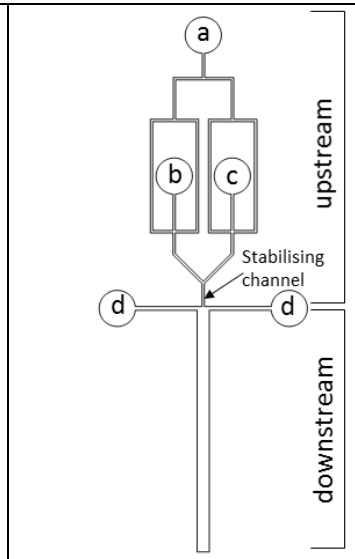
</td><td> 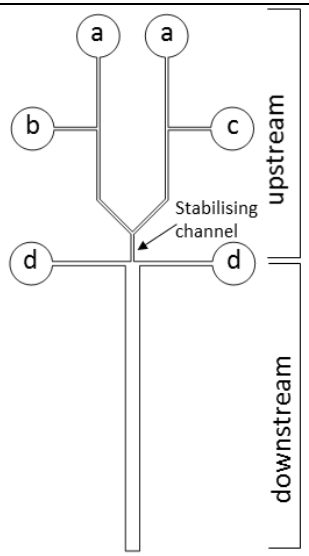
</td><td> 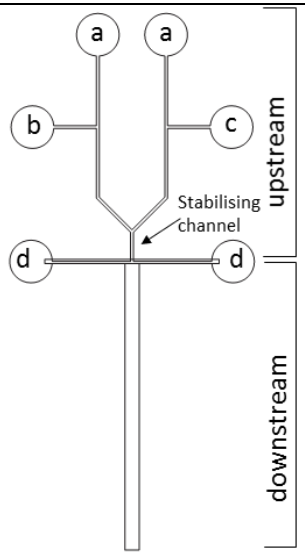
</td><td> 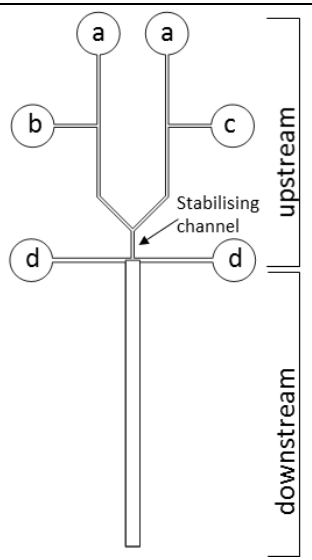
</td></tr>
<tr><td></td><td>Design A
(Preliminary design)</td><td>Design A1</td><td>Design A1a</td><td>Design A1b</td></tr>
<tr><td rowspan="4">Channel dimensions</td><td colspan="4">Upstream channel width and depth = 0.2mm</td></tr>
<tr><td>Stabilising channel width = 0.2mm</td><td colspan="3">Stabilising channel width = 0.3mm</td></tr>
<tr><td colspan="4">Downstream channel width and depth = 1mm</td></tr>
<tr><td colspan="2">Diluted yellow dye channel width =0.3mm</td><td>Diluted yellow dye channel width =0.15mm (Top Layer)
Diluted yellow dye channel width =0.3mm (Bottom Layer)</td><td>Diluted yellow dye channel width =0.3mm</td></tr>
</table>

Objective	To verify practicability of droplet encapsulation using PDMS - glass capillary hybrid system		Upstream Modification for droplet generation using T-junction geometry			1. Downstream modification for capillary control design geometry. 2. To verify experiment SOP		1. Modification for capillary control design geometry 2. To verify experiment SOP	
Design assumptions	Even cooking oil flow in each bifurcated channel		Uniform flow delivered by the syringe pump for identical channel length at upstream						
Design restrictions	Syringe pump limitation – insufficient syringe holder		N/A. Sufficient syringe holder for all inlets						
Design criteria	1. Preliminary design for two distinct inner droplets encapsulation. 2. Droplets generation via cross-junction geometry.		1. Simplified Design A. 2. Inner droplets generated independently 3. Cross-junction geometry replaced by T-junction geometry			1. Modified Design A1. 2. Diluted yellow dye channel width for the top layer was reduced to 0.15 mm serve as the glass capillary control.		1. Modified Design A1. 2. Modified glass capillary control to avoid flow disturbance.	
Analysis Summary:	Droplet size [µm]:		Droplet size [µm]:			Droplet size [µm]:		Droplet size [µm]:	
	Red	265	Red	212	217	Red	N/A	Red	N/A
	Blue	279	Blue	204	218	Blue	N/A	Blue	N/A
	W/O/W	784	W/O/W	780	774	W/O/W	N/A	W/O/W	N/A
	CV [%]:		*CV* [%]:			*CV* [%]:		*CV* [%]:	
	Red	5.8	Red	4.0	4.5	Red	N/A	Red	N/A
	Blue	5.8	Blue	2.6	4.4	Blue	N/A	Blue	N/A
	W/O/W	3.6	W/O/W	1.7	4.8	W/O/W	N/A	W/O/W	N/A
	Flow Ratio [µL/min] = 1: 12: 40		Flow Ratio [µL/min] = 1: 3: 40			Flow Ratio [µL/min] = N/A		Flow Ratio [µL/min] = N/A	
Summary	1. Low repeatability. 2. Uneven flow rate due to bifurcated channel. 3. Complicated start-up		Encapsulation depends on the capillary tube position at downstream cross-junction			Flow disturbance at capillary tube entrance		1. Optimised downstream for capillary tube placement. 2. Lead to Design A2 for alternating droplet sequence.	

CHAPTER 5: OPTIMISATION OF DOUBLE ENCAPSULATION

5.1 Overview

The design criteria of each PGHD was presented in Section 3.4 and summarised in Table 4-8. The channel geometry design was optimised to achieve effortless experimental start-up with successful encapsulation. The optimised design of PGHD-A2 was then further characterised with a few sets of flow rate ratio to achieve quantitative flow characterisation and to obtain a flow profile on different number of inner droplets encapsulation. The optimisation process was divided into few sections from fabrication to experiment SOP, introduced in Section 3.4. Hence, this chapter focus on the optimisation of each section with reference to Design A2. The channel design was justified upon the experiment results.

5.2 Short Summary on Optimised Process

5.2.1 Design Analysis

Design A2, the final design inspired by Okushima *et al.*[27] was reported to produce alternate inner droplet sequence with successful distinct droplets encapsulation. Considering the simple and straightforward upstream channel design – dual T-junction as a merit, the dimensions of the dual T-junction geometry were modified according to the previous experience and experimental results from PGHD-A and PGHD-A1. The modification ensures consistent analysis and enable systematic interpretation on the droplet behaviour for further modification and improvement on the channel design.

Initially in Design A, the microchannel width and height of the upstream were fixed at 0.2mm with the diluted yellow water channel width fixed at 0.3mm. The height was increased to 1mm at the downstream to allocate the glass capillary tube with inner diameter of 0.58mm (Figure 5-1a). The enlarged diluted yellow dye section, A_2 reduced

the fluid velocity with higher inner fluid pressure and hence the W/O emulsion droplets can be easily flow into the glass capillary tube section, A_3 without much restriction. The W/O emulsion droplets flow along the capillary tube and discharged at the collection plate without being encapsulated (Figure 5-1b). This phenomenon states the essentiality of the glass capillary tube placement in inducing shear force to create encapsulation.

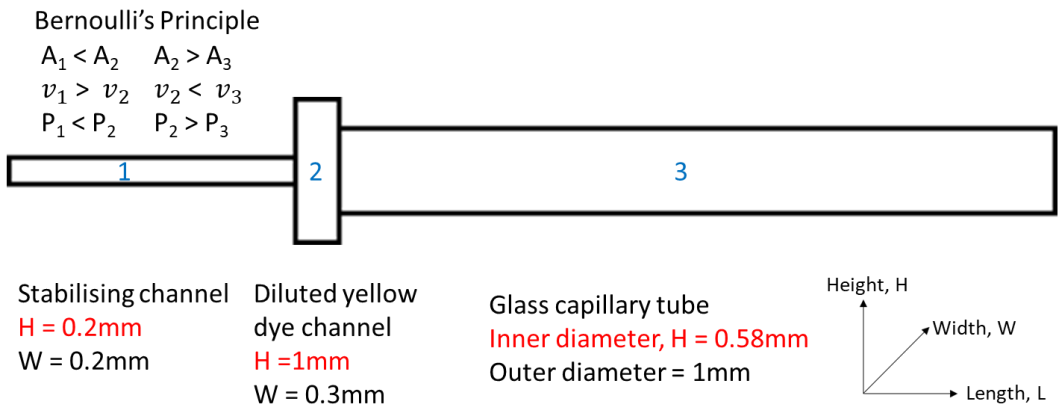

(a)

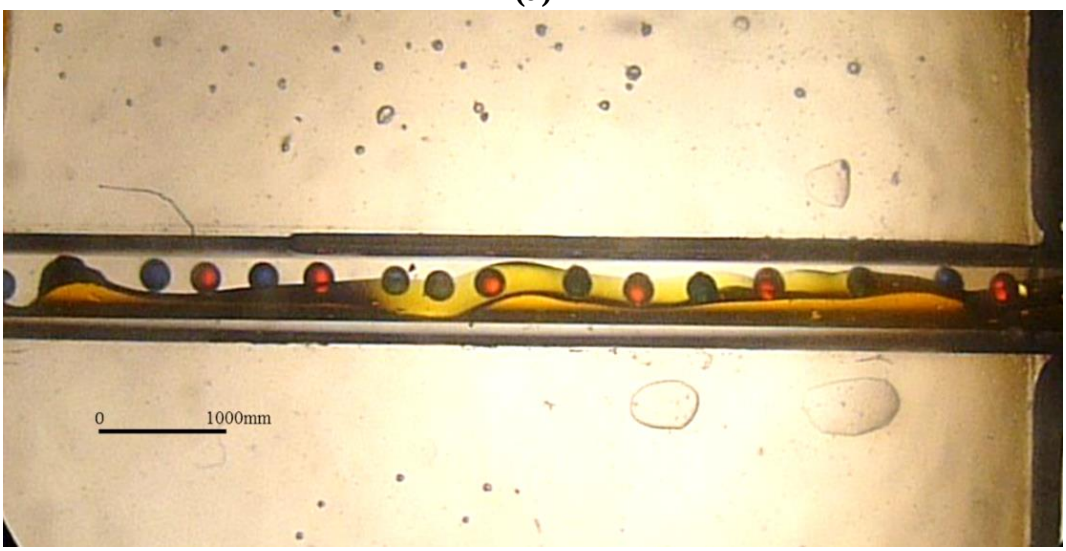

(b)

Figure 5-1. (a) Side view of Design A showing the different height dimensions across the diluted yellow dye channel. (b) Downstream of the PGHD without encapsulation process

In Design A1, the enlarged stabilising channel reduced the flow of the inner droplets, pairing 1 red and 1 blue droplet before entering the glass capillary tube. Although the paired droplets were disturbed by the flow circulation at the entrance of capillary tube,

the inner droplets swirled without collision. Through experimental observations, encapsulation happen when glass capillary tube placed at 0.5δ. The design was extended to Design A1-1 and A1-2 for better control on the capillary tube placement. The extended versions verified glass capillary tube positioned at 0.5δ facilitates the encapsulation process. To achieve alternate droplets sequencing, the upstream design was simplified into a dual T-junction geometry – Design A2.

The channel dimension of PGHD-A2 was improved based on the optimisation objective i.e. simple fabrication and easy experiment start-up. In Design A and A1, the channel width at the upstream was 0.2 mm to constraint the inner droplet size. Based on the calculated v_{sp}, the inner droplets were generated under dripping regime at the upstream (Table 3-1) and hence the cutting quality become the primary concern. The overall channel width was increased (Figure 5-2) for better cutting quality while enhancing the efficiency. The glass capillary control was improved by introducing the diluted yellow dye channel as a right-angled triangle narrowing towards the cross-junction geometry (Figure 5-2). This enhance the accuracy of the placement and reduce the error of manual film stacking. The glass capillary tube was cut and polished to 1.5cm ensuring constant pressure difference for each hybrid device.

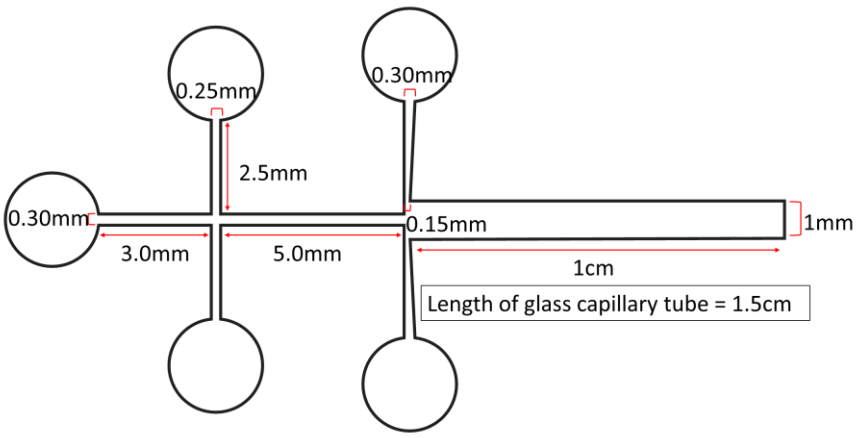

Figure 5-2. Channel dimensions of Design A2.

5.2.2 Experiment SOP

The experiments carried out by PGHD-A2 demonstrated the significance of pumping sequence. Development of the experimental SOP is essential to ensure the positive outcome of the droplet encapsulation. Although vast encapsulation experiments were reported by different research groups, however, most of the experimental methodology only provides general guidelines without further elaboration where some of the experiments are not repeatable. Experience shows that the sequence of the fluid pumping into the system is important to maintain the intrinsic surface properties of the hybrid system.

The protocol aimed to provide a systematic start up, ensuring the success of similar experiments and used as a start-up reference for other hybrid microfluidic devices. Before the protocol was developed, the encapsulation process was random even when the same flow rate ratio was used. Experimental observations show alteration of the encapsulation mechanism when the system was disturbed. Minimal disturbance was amplified greatly under a micro-scale due to its sensitivity, then leads to unsuccessful encapsulation. Through experiments, the problem resulted in the sensitivity of the hybrid microfluidic devices has been slowly identified and resolved.

Regardless of the stabilisation period for droplet generation at upstream, the inner droplet sequences was disturbed once the diluted yellow dye was introduced into the system. This is because balancing between three forces i.e. inner aqueous phase, middle organic phase and outer aqueous phase is essential for the encapsulation to take place. Hence, pre-stabilisation of droplet formation was eliminated. In the earlier stage of research work, it was assumed that the fluctuating flow distribution was caused by the uneven force distributed at the plunger, hence, syringes with smaller volume were used

(Figure 5-3). To avoid refilling during the experiment, the pumps were paused intermittently while waiting for the fluid to filled up the channel and generate droplets. Experiment 3 (Section 4.8.3), however, verify the practicability of syringes volume and hence syringes with larger capacity i.e. 10 mL were used for both diluted red and blue dye and cooking oil whereas 30 mL syringes were used to deliver the diluted yellow dye.

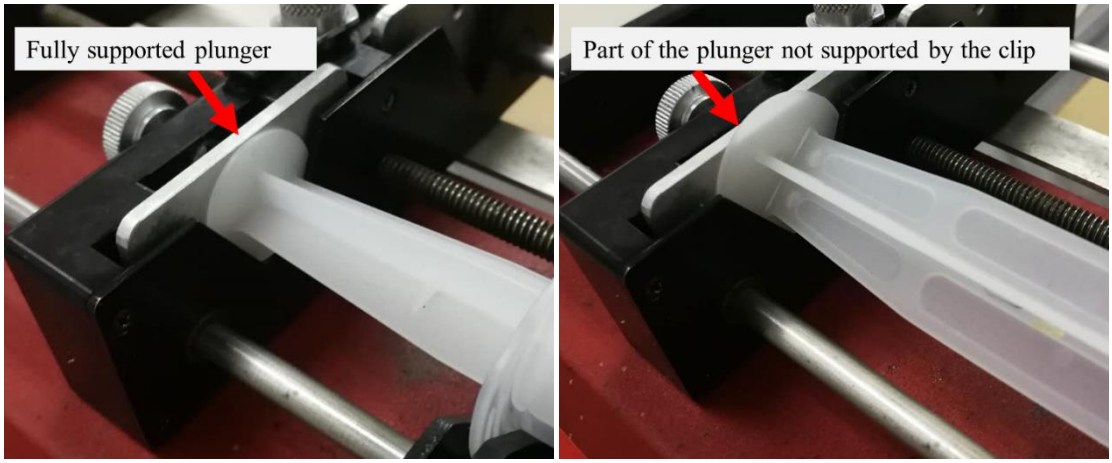

(a) **(b)**

Figure 5-3. (a) 20mL syringe with plunger fully supported by the clip. (b) 30mL syringe plunger unable to be fully supported.

Besides the syringe capacity, the recording method was modified as well. Previously, the video recording requires an 8-minute interval in between each recorded video, prolonging the overall experimental duration. The recording duration was later shortened by first saving the videos into the high-speed camera temporarily. The videos were then extracted into the computer later to avoid unnecessary fluid discharge during the delay. The replacement of larger syringes and the changing of recording method conserve the flow usage during the recording stage and hence generated allowance for pre-stabilised period. In the optimised experimental SOP, both inner and outer aqueous phase were introduced into the PGHD and fill up the system before the cooking oil was pumped in. This prevent the adhesion of cooking oil onto the inner surface of the capillary tube and avoid contamination of the aqueous reservoir by the cooking oil. The success rate of droplet formation and encapsulation was increased to 99.9% at this stage with 0.1%

contributed by human error. Figure 5-4 shows the optimised flow of the experimental SOP.

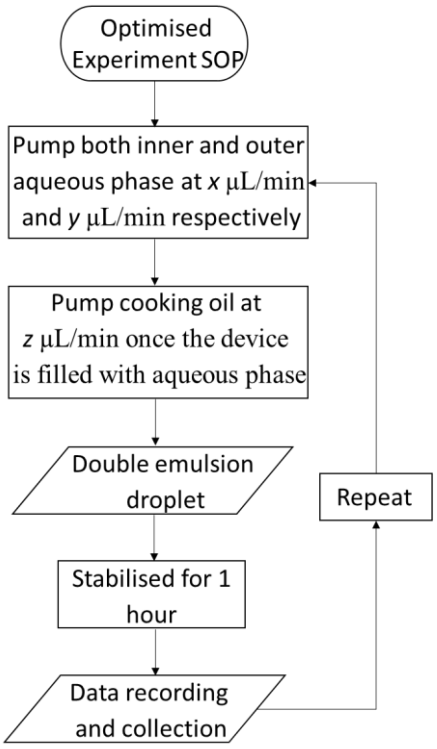

Figure 5-4. Flow chart of the optimised experimental SOP.

5.2.3 Image Analysis

Three measurement methods were tested to determine the suitable method: (i) Straight-Line, (ii) Thresholding 1 and (iii) Thresholding 2. Thresholding 2 was chosen and has been introduced in Section 4.6 on the analysis methodology. This section compares the three methods and justify the method quantitatively. Regardless of the colours, 20 inner droplets were measured to compare the effect of each method towards the size distribution.

Straight-line method was used to analyse the droplets generated by PGHD-A. The diameter of the droplets was defined by the droplet length, manually measured by plotting maximum horizontal line across the droplet (Figure 5-5a). This method highly depends on the human judgement and affected by the clarity of the image. Thresholding method, on the other hand, defines the image through light intensity. Both thresholding 1 and 2 utilise the "try all" function to determine the threshold value. In thresholding 1, a rectangular was drawn to include the outline of the droplets and directly measure the size (Figure 5-5b). Thresholding 2, on the other hand, utilised the function of "Analyse Particles" to measure the droplet size (Figure 5-5d). This function allows measurement of only the outlines of the droplets and eliminate extra background included in the similar intensity range as the object (Figure 5-5c).

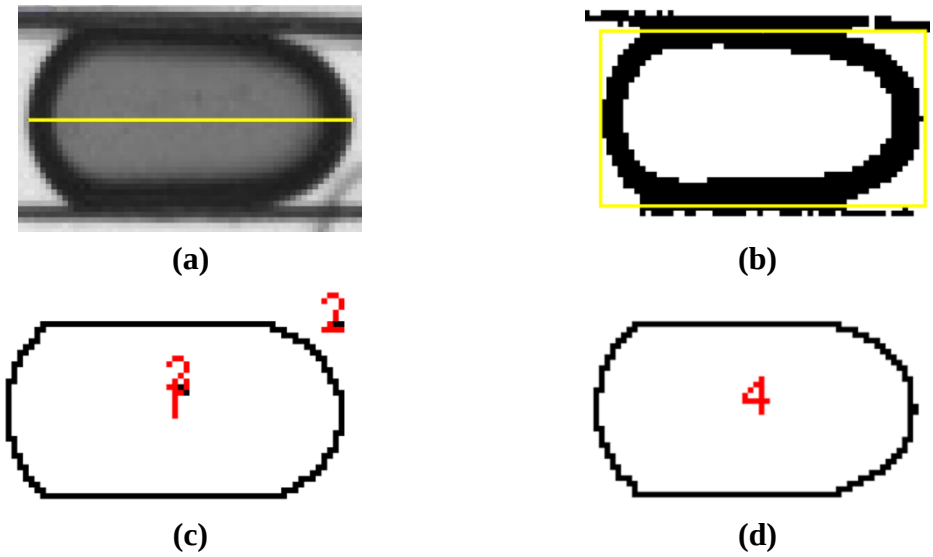

Figure 5-5. Illustration of droplet measurement at each different method. (a) Straight-line. The measurement is done at the longest distance across the droplet. (b) Thresholding 1. Rectangular selection was used to measure the outline of the droplet. (c) Thresholding 2. The background particles were differentiated by different numbers labelling. (d) Thresholding 2. Outline of the droplet for measurement.

The droplet size measured by three methods were tabulated in Table 5-1 with their standard deviation and *CV*. Thresholding 1 shows largest droplet size with lowest standard deviation and *CV* among the three methods, because the measurement shown was according to the area of the rectangle drawn instead the droplets' outline. Droplet size measured by straight-line and thresholding 2 method was similar to each other indicating the consistency of both methods. Thresholding 2, however, was preferred as the measurement was automated, hence eliminating human judgement. The high standard deviation and *CV* for both straight-line and thresholding 2 was caused by the distinctive red and blue inner droplets measurement.

Table 5-1. Comparisons between different measurement methods.

Method	Straight-Line	Thresholding 1	Thresholding 2
Average Droplet Size [µm]	518	599	519
Standard Deviation	31.6	27.8	32.3
CV [%]	6.1	4.6	6.2

5.3 Results and Discussions

This section discusses the experimental results conducted in PGHD-A2. The results were discussed from different perspective, including droplet size distribution, droplet sequencing and the success rate of encapsulating different number of inner droplets.

5.3.1 Short Summary of Numerical Data of Experimental Parameter

The Ca_{total} used in this chapter was modified according to the work of Abate *et al.* [114]. In their work, they defined the superficial velocity by dividing the continuous phase flow rate with the average cross-sectional area occupied by the continuous phase. The average cross-sectional area occupied by the continuous phase was calculated by multiplying the total cross-sectional area of glass capillary tube with the ratio of continuous volumetric flow rate. The modified Ca_{total} was more accurate as it taken the manipulation of middle phase into account.

The *Ca* and flow ratio were calculated using Equation 18 and Equation 19.

$$\boldsymbol{Ca_{in} = \frac{\mu_2 v_{sp,2}}{\gamma_{1,2}}} \quad ; \quad \boldsymbol{Ca_{total} = \frac{\mu_3 v_{sp,3}}{\gamma_{23}}} \qquad \textbf{Equation 18}$$

where Ca_{in} = upstream *Ca*; Ca_{total} = *Ca* of the double emulsion formation calculated using the cross-sectional area of the glass capillary tube and total v_{sp}; μ_2 = viscosity of cooking oil; μ_3 = viscosity of diluted yellow dye; $v_{sp,2}$ = v_{sp} of cooking oil; $v_{sp,3}$ = v_{sp} of diluted yellow dye; $\gamma_{1,2}$ = average γ of diluted red and blue dye in cooking oil; $\gamma_{2,3}$ = average γ of cooking oil in diluted yellow dye.

$$\boldsymbol{\varphi_1 = \frac{Q_{d1}}{Q_{c1}}} \quad ; \quad \boldsymbol{\varphi_{total} = \frac{Q_{d2}}{Q_{c2}}} \qquad \textbf{Equation 19}$$

where φ_1 = flow ratio of the upstream; φ_{total} = flow ratio of the double emulsion formation; Q_{d1} = total dispersed flow rate of diluted red and blue dye; Q_{d2} = total dispersed flow rate

of upstream; Q_{c1} = flow rate of middle phase, cooking oil; Q_{c2} = flow rate of outer aqueous phase, diluted yellow dye.

Table 5-2 summarised the calculated data for each flow rate ratio.

Table 5-2. Summary of Calculated *Ca* and flow ratio, φ for each flow rate ratio.

Flow rate ratio	Ca_{in} ($\times 10^{-2}$)	Ca_{total} ($\times 10^{-4}$)	φ_1	φ_{total}
1:2:40	0.38	5.28	1.00	0.05
1:4:40	0.75	5.41	0.50	0.08
1:4:50	0.75	6.67	0.50	0.06
1:6:40	1.13	5.54	0.33	0.10
1:6:50	1.13	6.79	0.33	0.08
1:6:60	1.13	8.05	0.33	0.07
1:6:70	1.13	9.31	0.33	0.06
1:6:80	1.13	10.57	0.33	0.05
1:8:60	1.51	8.18	0.25	0.08
1:8:70	1.51	9.44	0.25	0.07
1:8:80	1.51	10.70	0.25	0.06

5.3.2 Droplet Size Distribution

The experimental investigation was first carried out using different flow rate ratio to verify the effect towards the droplet size. Throughout all experiments, the inner aqueous flow rate was fixed at 1 µL/min. The flow rate ratio was manipulated accordingly: (1) Fix inner and outer aqueous flow rate and manipulate middle organic phase, (2) Fix inner and middle flow rate and manipulate outer aqueous phase; to understand the effect of middle continuous phase and outer continuous phase towards the size of W/O emulsion and W/O/W double emulsion droplets respectively. To initiate, 6 experiments (Table 5-3) classified into three groups were conducted. More flow rate ratios were then added according to the Ca_{total} and φ_{total}, to obtain a smooth trendline and to further verify the droplets behaviour.

Table 5-3. Initial flow rate ratio experimental objective.

Group	Flow rate ratio [µL/min] (inner: middle: outer)	Experimental Aim
A	1:2:40; 1:4:40 and 1:6:40	To verify the effect of middle continuous phase towards the inner droplet size
B	1:6:40, 1:6:60 and 1:6:80	To verify the effect of outer aqueous phase towards the double emulsion droplet size
C	1:4:40, 1:6:60 and 1:8:80	To observe the droplet size with outer aqueous phase 10x larger than the middle phase.

To better illustrate the relationship of the dimensionless droplet size, L/D and flow ratio, bar charts have been plotted as shown in Figure 5-6**Error! Reference source not found.**, Figure 5-8**Error! Reference source not found.** and Figure 5-10**Error! Reference source not found.**. The percentage shown in the bar chart represents the *CV* value for each droplet size.

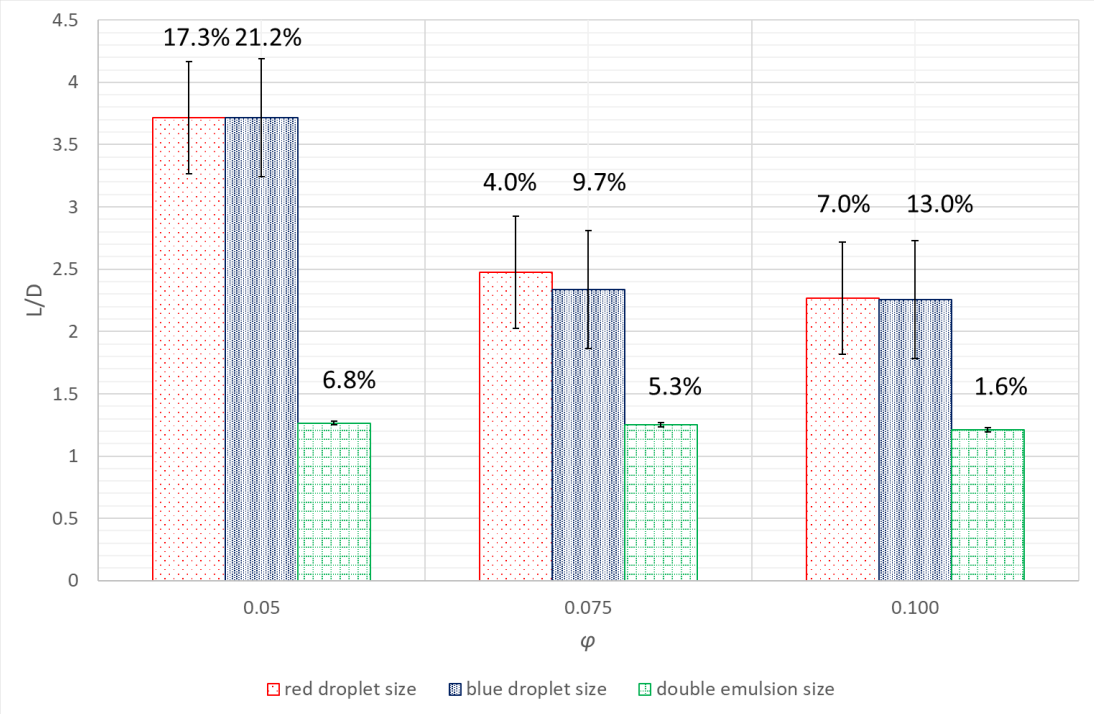

Figure 5-6. Droplet size comparisons between 1:2:40 (0.05), 1:4:40 (0.075) and 1:6:40 (0.100) µL/min (Group A). Percentage shown represents the *CV* value.

Due to the inconsistent flow at 1:2:40 µL/min, the sample size was maintained at 10 droplets with one-hour stabilisation period. Droplet size produced at 1:2:40 µL/min were largest, i.e. plug size 4.5x wider than the channel width indicating droplets produced under squeezing regime. The characteristic of squeezing regime caused merging of the inner droplets at the dual T-junction geometry during the breakup process. As the system become more stabilised, alternate inner droplets were generated at the dual T-junction. The size of the inner droplets generated were consistent due to the break-up mechanism of squeezing regime. As the middle continuous flow rate increases, the inner droplet size generated reduces and the flow regime shifted from squeezing into transient regime. High *CV* value (larger than 5% as shown in Figure 5-6**Error! Reference source not found.**) of the inner droplets were noticed due to the opposition forces between the inner phases. The double emulsion droplets generated decreasing in size, affected by the inner droplet size and the encapsulation configuration as presented in Figure 5-13 later.

Droplet generation at dual T-junction geometry was not only affected by the shear force from the continuous phase, but also by the interfacial tension force from the opposing inner fluid. Two phenomena were observed in the experiment: (1) the tip of the droplet will be forced back to its respective channel by the opposing fluid before further elongating into the main channel (Figure 5-7a-e); (2) the droplets were sheared into smaller size by the opposing fluid before the droplet is fully developed, generating premature droplets (Figure 5-7f). The first condition disrupted and randomised the alternating droplet sequencing. The second condition however is the main reason that affects the consistency of droplet production and thus resulting in higher polydispersity of the inner droplets. Although the droplets frequently flow into the channel alternatively, occasionally one of the fluids will be dominant due to the inconsistent flow. The inconsistent flow in the stabilised system was caused by the syringe pumps where studies

have shown that the stepper motor of syringe pump is a source of fluctuations in microfluidic flows [115].

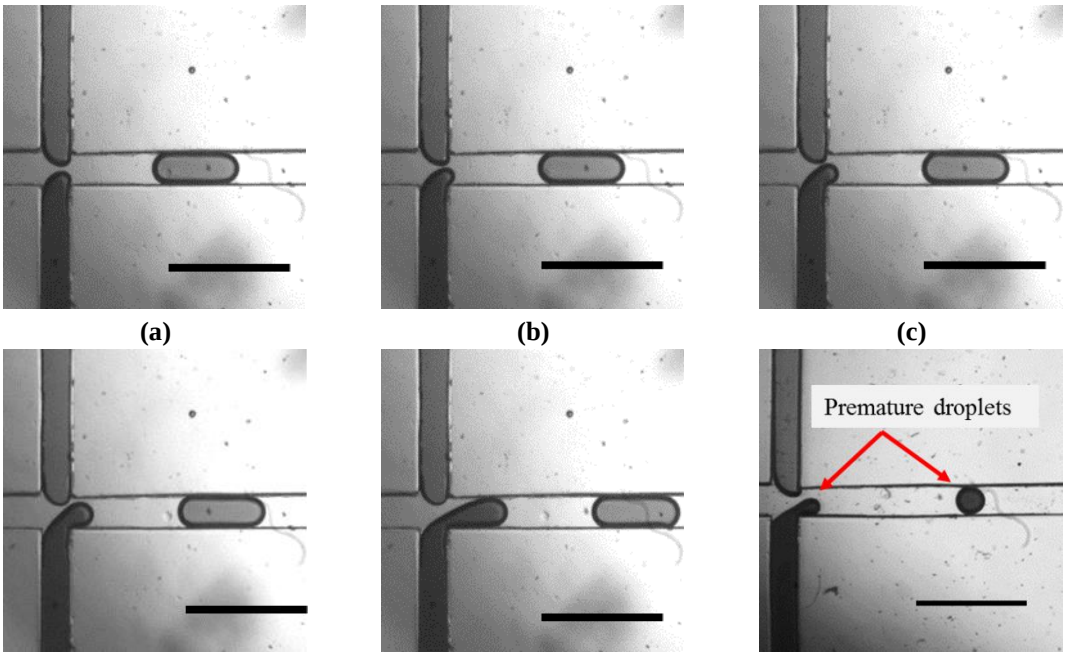

Figure 5-7. Opposition force from both inner phase during droplet generation. (a-b) Both inner fluid advanced to the main channel and flows into the main channel. (c-e) Diluted blue dye managed to flow into the main channel while forcing the tip of diluted red dye back into its channel. (f) Inner blue droplet break before fully developed in the main channel due to the opposition force from the diluted red dye. All scale bars represent 1000 µm.

The opposition force from the inner phase was due to the different interfacial tension between both inner red and blue diluted dye with the cooking oil. As the interfacial tension value decreases, the droplets generated at a higher frequency with reduction in size [116]. However, inner red droplets do not show smaller size as compared to the inner blue droplets due to the fluctuation of pumps. Hence, future work is required to be carried out to investigate the dominance between the interfacial tension and the fluctuations caused by the syringe pump quantitatively.

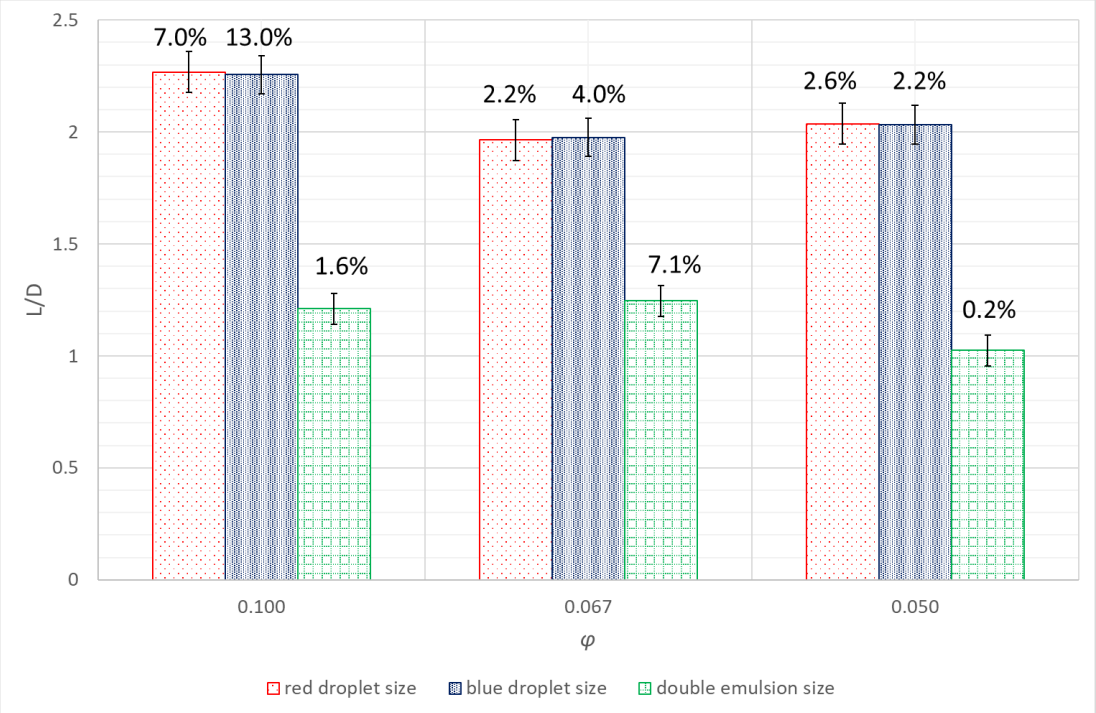

Figure 5-8. Droplet size comparisons between 1:6:40 (0.100), 1:6:60 (0.067) and 1:6:80 (0.050) µL/min (Group B). Percentage shown represents the *CV* value.

Group B fixed the middle continuous phase flow rate with increasing outer aqueous flow rate. The overall monodispersity of the droplet size (Figure 5-8) improved, where *CV* of the double emulsion droplets were all maintained below 3% except at 1:6:60µL/min. This is because the breakup point of the double emulsion droplets is very near towards the outlet of the capillary tube due to the contamination (Figure 5-9). The inner droplet size was indirectly affected by the outer aqueous phase, reducing as the outer aqueous phase increases. The inner droplet size produced at 1:6:80µL/min were slightly higher compared to 1:6:60µL/min due to the small φ. The consistency of both inner droplets have improved i.e. error percentage reduced from 0.6% to 0.2%, verifying the essentiality of equilibrium between three forces i.e. inner, middle and outer phase to stabilise the whole system. The average size of the double emulsion droplets produced at 1:6:80 µL/min was 594 µm, lowest in the group, caused by the highest single droplet encapsulation.

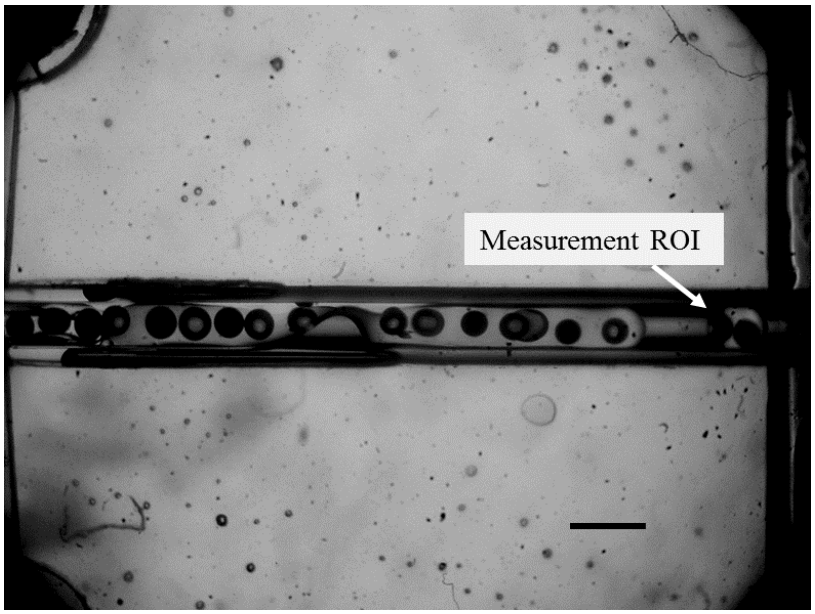

Figure 5-9. Double emulsion droplet breakup point is near to the outlet of the capillary tube due to the contamination. Aqueous droplets adhere to the capillary inner wall affecting the breakup location.

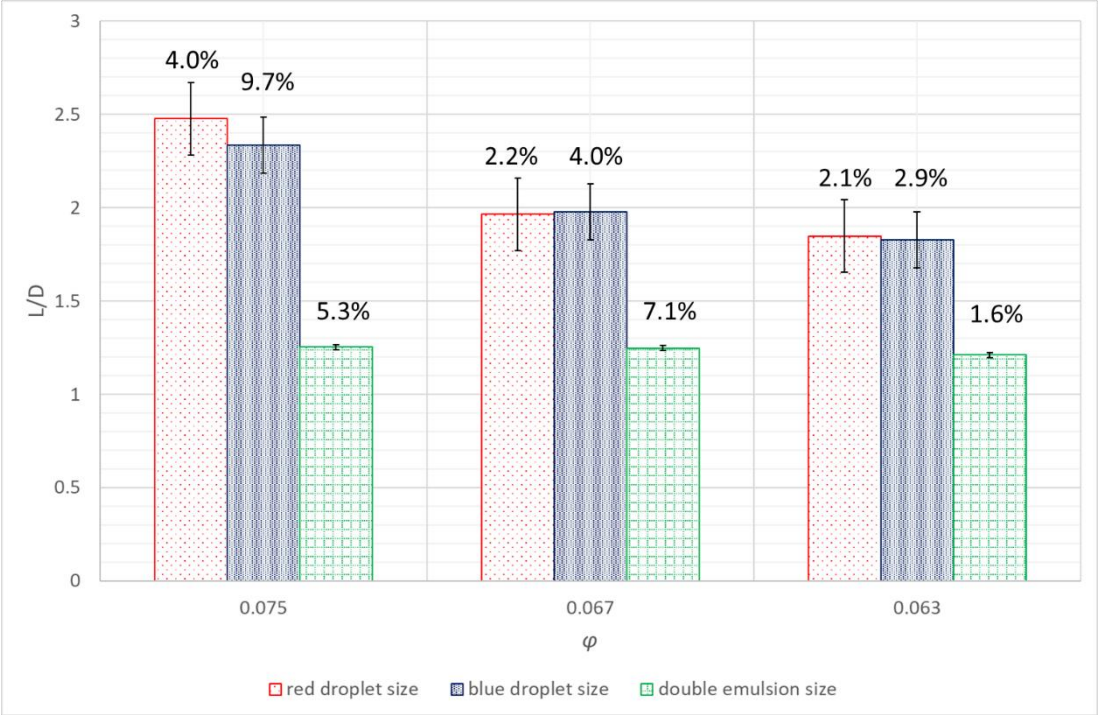

Figure 5-10. Droplet size comparisons between 1:4:40 (0.075), 1:6:60 (0.067) and 1:8:80 (0.063) µL/min (Group C). Percentage shown represents the *CV* value.

At 1:10 ratio of middle: outer phase, 1:6:60 and 1:8:80µL/min generate consistent monodisperse droplets where 1:8:80µL/min shows better results with all *CV* value under 3%. The ratio, however, was not suitable for 1:4:40µL/min due to the insufficient Q_c. The size of the inner droplets decreases with smaller φ and increased *Ca*, consistent with the

experiment and numerical observation by Liu and Zhang [43]. The overall comparisons for all 6 flow rates were shown in Figure 5-11.

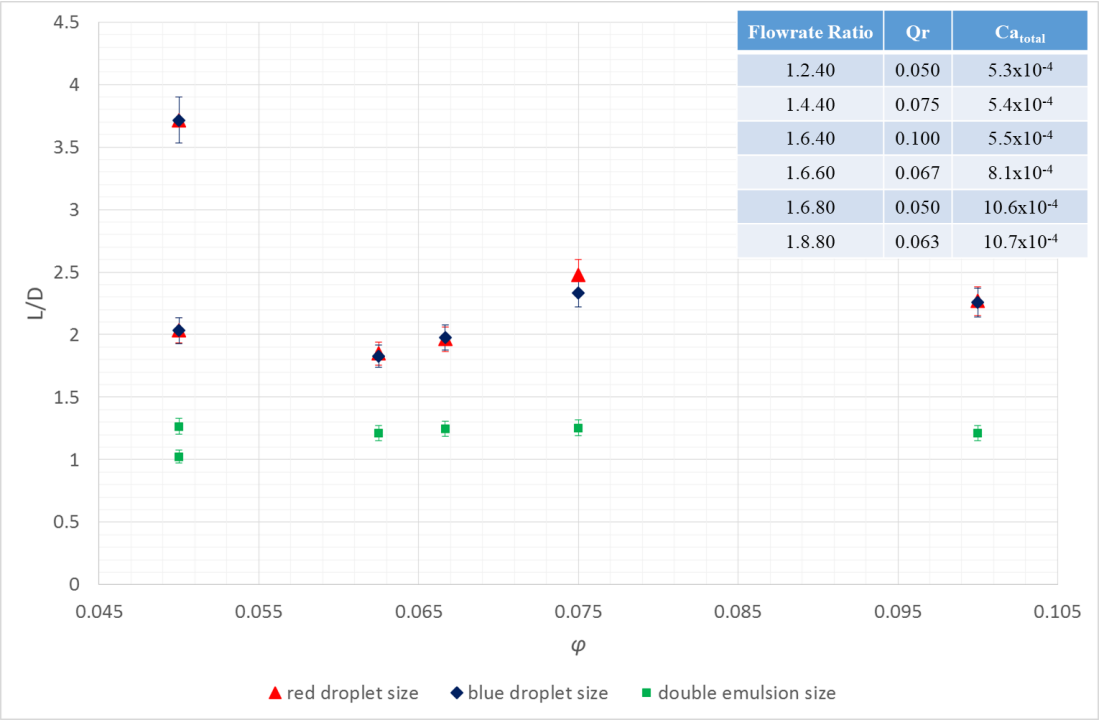

Figure 5-11. Droplet Size Comparisons for all φ.

To further verify the relationship between the size distribution of double emulsion and Ca_{total}, more flow rate ratios were added to obtain a smooth curve (Figure 5-12).

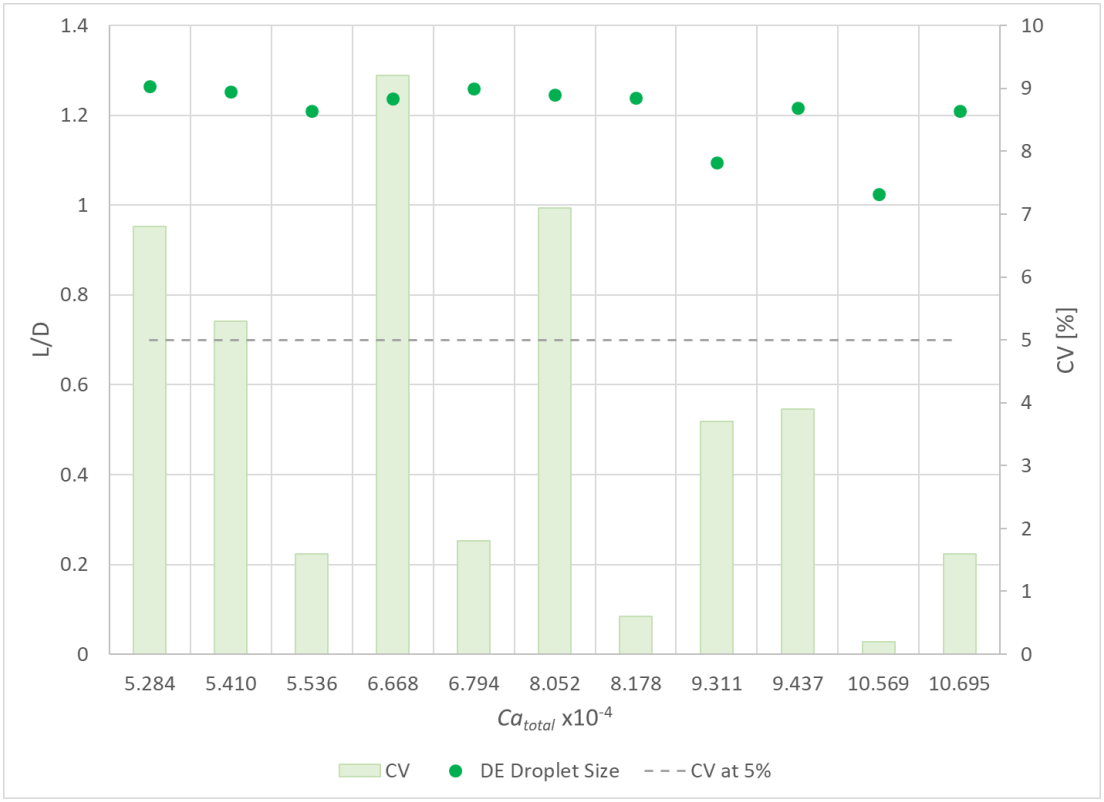

(a)

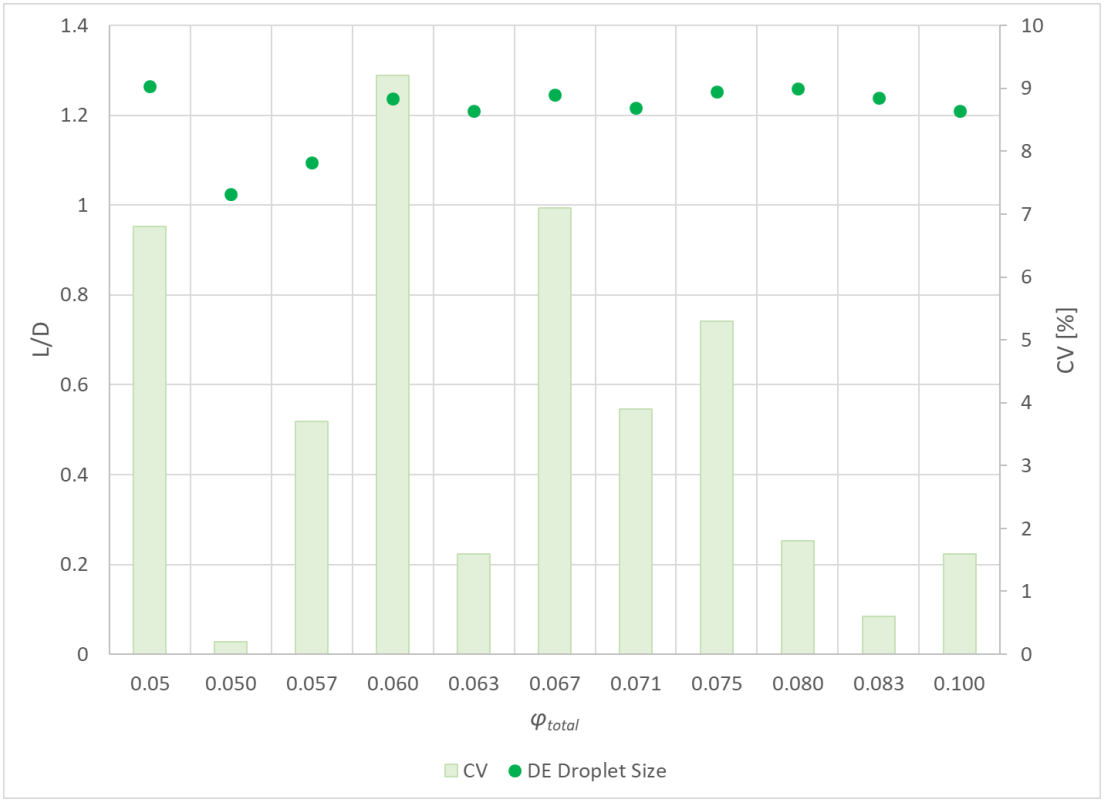

(b)

Figure 5-12(a) Graph of double emulsion droplet size versus Ca_{total} with their respective *CV* value. (b) Graph of double emulsion droplet size versus φ_{total} with their respective *CV* value.

The droplet size was inversely proportional to the Ca_{total} and proportional to φ_{total} as shown in Figure 5-12a and Figure 5-12b respectively, consistent to the reported work by Liu and Zhang [43]. Starting from Ca_{total} of 6.794, the double emulsion droplets generated were all highly monodispersed, indicating the significance of the shear force from the continuous phase to maintain the monodispersity. At Ca_{total} of 10.569, the *CV* value was lowest because of the highest single droplet encapsulation rate (92.5 %) which will be further discussed in Section 5.3.4. Although 1:2:40 and 1:6:80 µL/min shows identical φ_{total} but the droplet size and monodispersity generated were in huge difference, due to the insufficient middle phase shear force, causing inner droplets generated in different flow regime at the upstream.

Pinching is a process where W/O emulsion is being sheared by the diluted yellow dye. During the pinching process, the W/O emulsion plug will form a bulb area towards the end of the pinching point (Figure 5-13a). Since the cross-sectional area of the glass capillary tube expanded, the upstream W/O emulsion flow rate reduces once they entered the downstream glass capillary tube. The pinching distance and pinching rate depends on the flow rate of dispersed phase and continuous phase i.e. Ca_{total}. Experimental observations show that the size of the double emulsion droplet was affected by the location of the inner droplets during the pinching process, the number of encapsulated droplets and its configuration (Figure 5-13b-e).

If the inner droplet was located inside the bulb area during pinching occurs, W/O/W double emulsion droplet with a thin shell will be generated (Figure 5-13b). However, if the inner droplet is at the edge of the pinching neck, the pinching region will tend to elongate downstream to enable the encapsulation of inner droplets without breaking the inner droplets, due to the difference of interfacial tension (Figure 5-13c). However, the

inner droplets tend to break if they located right at the pinching neck, resulting in empty encapsulation (Figure 5-13d). Apart from that, the encapsulated droplets will form a longer plug if the two inner droplets were placed horizontally beside each other (Figure 5-13e). Due to the flow circulation at the cross-junction, the inner droplets tend to rotate when flowing in the plug, the double emulsion droplets will become smaller when the inner droplets overlapped with each other or is positioned diagonally to each other (Figure 5-13f).

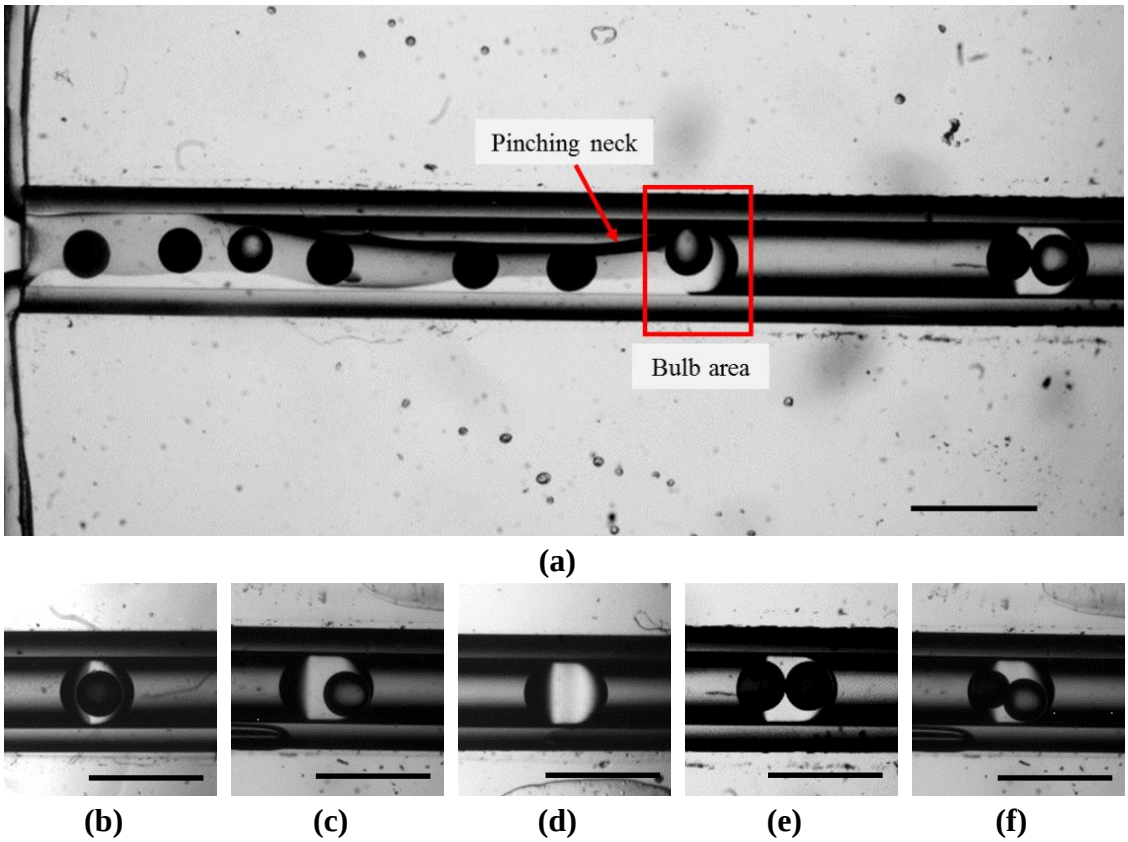

Figure 5-13. (a) Pinching process to form double emulsion droplets. (b) Thin shell double emulsion droplet with single inner droplet. (c) Thick shell double emulsion droplet with single inner droplet. (d) Empty encapsulation as the inner droplet break and mixed with outer aqueous phase. (e) Double emulsion plug with two inner droplets placed horizontally to each other. (f) Smaller double emulsion droplet with two inner droplets placed diagonally to each other.

5.3.3 Droplet Sequencing

PGHD-A2 consists a dual T-junction geometry at the upstream, with single main channel for the continuous cooking oil to generate two distinct inner droplets. Ideally,

alternate droplet sequencing will be obtained referring to Okushima *et al.*, however, experimental observations shows competition between the two inner aqueous phases during droplet generation at the upstream. This section therefore presents the droplet sequencing at each flow rate ratio. The graphs were plotted by representing inner blue droplet as 1 while inner red droplets as 0. Therefore, a sinusoidal curve with sustained oscillation will be obtained when the droplets were generated in alternating sequencing at the upstream. At higher Ca_{total}, the droplet frequency were higher and hence the first 70 droplets were taken for consistent comparisons. Figure 5-14 shows the droplet sequence of Group A, where both inner and outer aqueous phase flow rate were fixed.

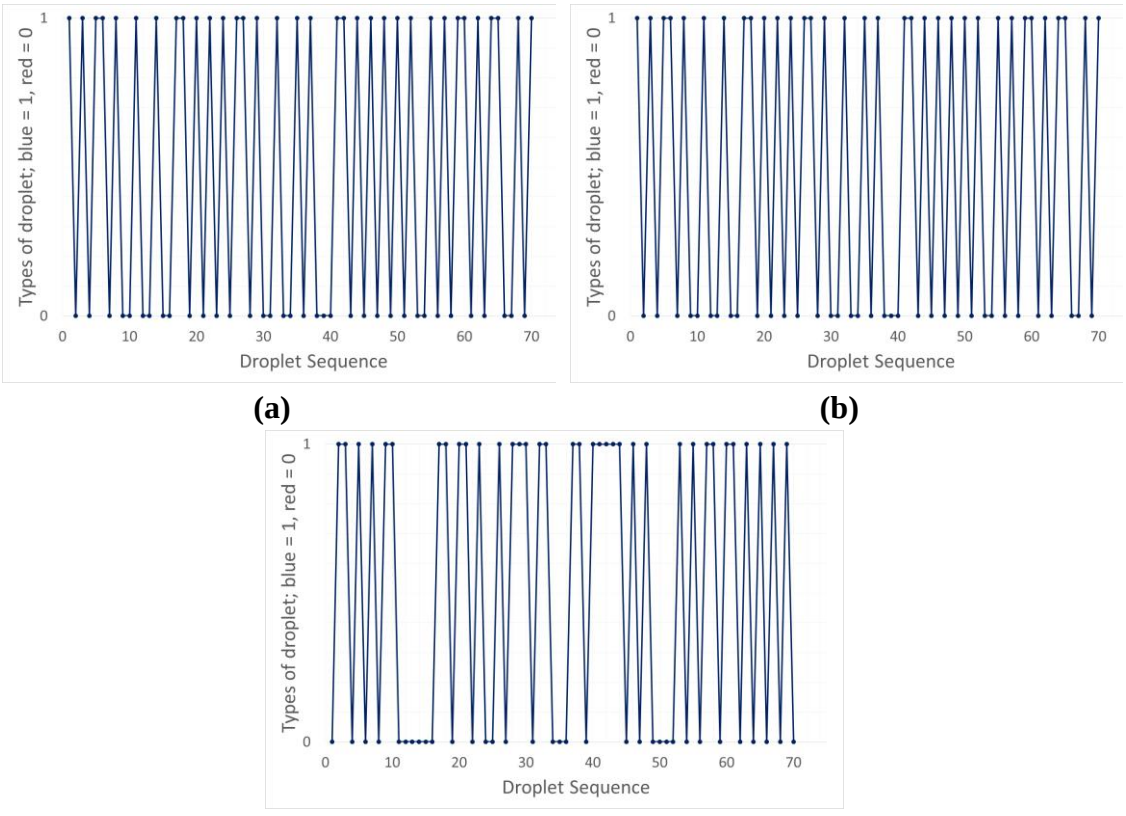

Figure 5-14. Droplet Sequencing at flow rate ratio (a) 1:2:40 µL/min (b) 1:4:40 µL/min (c) 1:6:40 µL/min

Figure 5-14a and b show similar trend while Figure 5-14c (1:6:40 µL/min) shows most inconsistent alternating sequencing. This is due to the insufficient Q_c (outer aqueous flow rate) at the downstream to achieve equilibrium in the system. Hence, induce fluctuations

during the pinching process which lead to the rotation of the inner droplets and disturbed the droplet sequencing. Fixing the inner and middle phase flow rate at 1:6 µL/min, while increasing the outer aqueous flow rate from 50 – 80 µL/min (Figure 5-15), the alternating sequence approaches steady state as the outer aqueous flow rate increases. Overall, 1.6.80 µL/min (Figure 5-15d) shows the steadiest alternating sequencing indicating the optimum flow rate ratio for droplet sequencing.

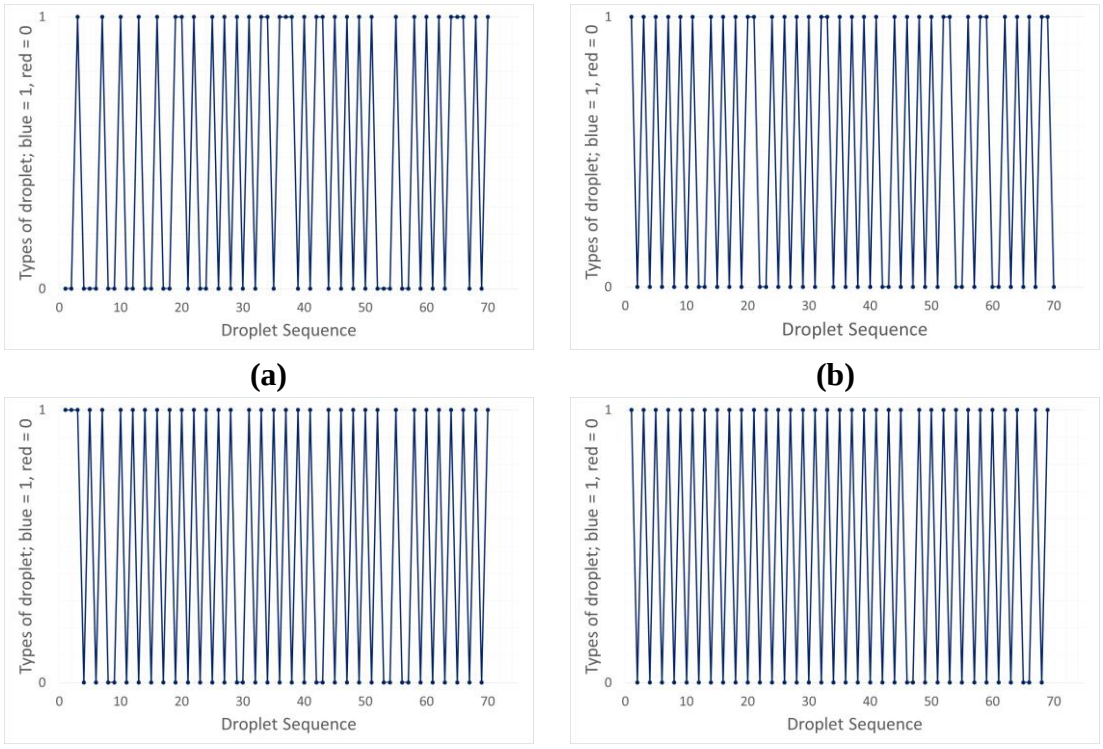

Figure 5-15. Droplet Sequencing at flow rate ratio (a) 1:6:50 µL/min (b) 1:6:60 µL/min (c) 1:6:70 µL/min (d) 1:6:80 µL/min

The middle phase and outer aqueous phase flow rate was then fixed at 1:10 ratio as (Figure 5-16). Figure 5-16a, b and c show no significant difference, hence concluding the ratio of 1:10 or higher for the middle to outer phase is favoured for alternate droplet sequencing, due to the reduction of droplet competing at this ratio.

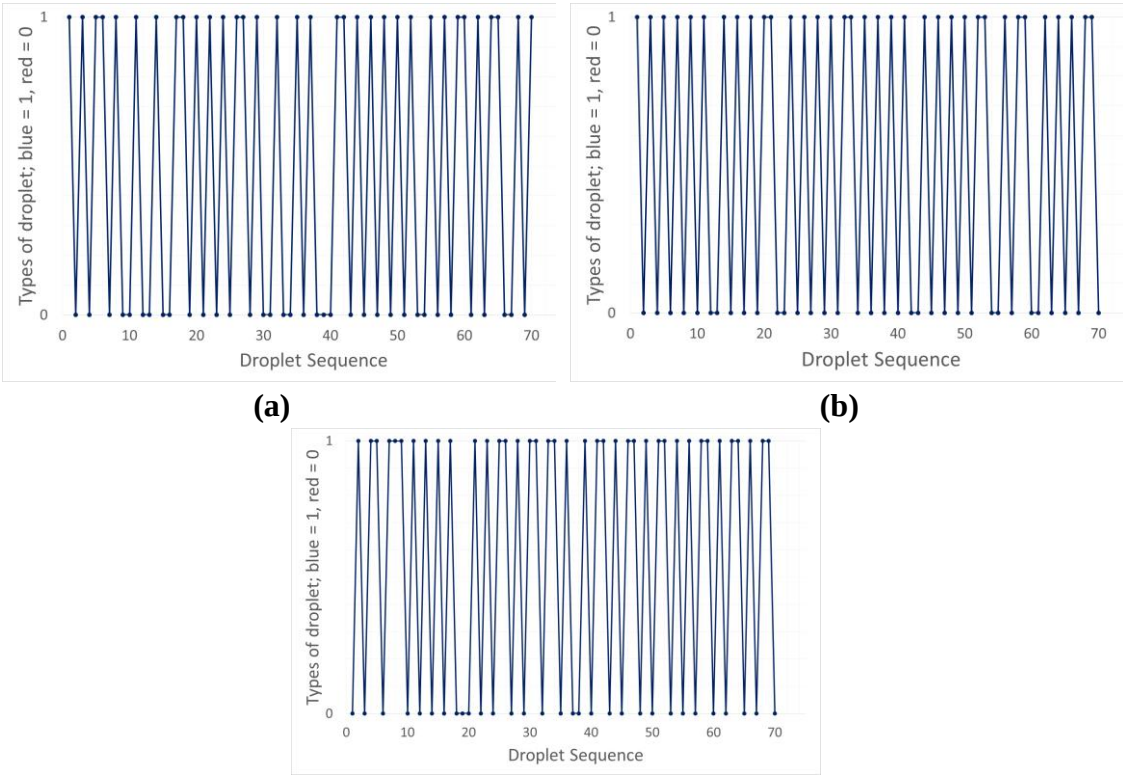

(a) **(b)**

(c)

Figure 5-16. Droplet Sequencing at flow rate ratio (a) 1:8:60 µL/min (b) 1:8:70 µL/min (c) 1:8:80 µL/min

5.3.4 Success Rate of the Droplet Encapsulation

Depending on the droplet sequencing and pinching process, 6 different combinations of encapsulation can be observed in this hybrid microfluidic system (Figure 5-17). As mentioned in Section 5.3.2, the zero encapsulation was resulted when the inner droplet was located at the pinching neck during the pinching process. Hence considered as an anomalous result since the objective of this research work is to encapsulate droplets.

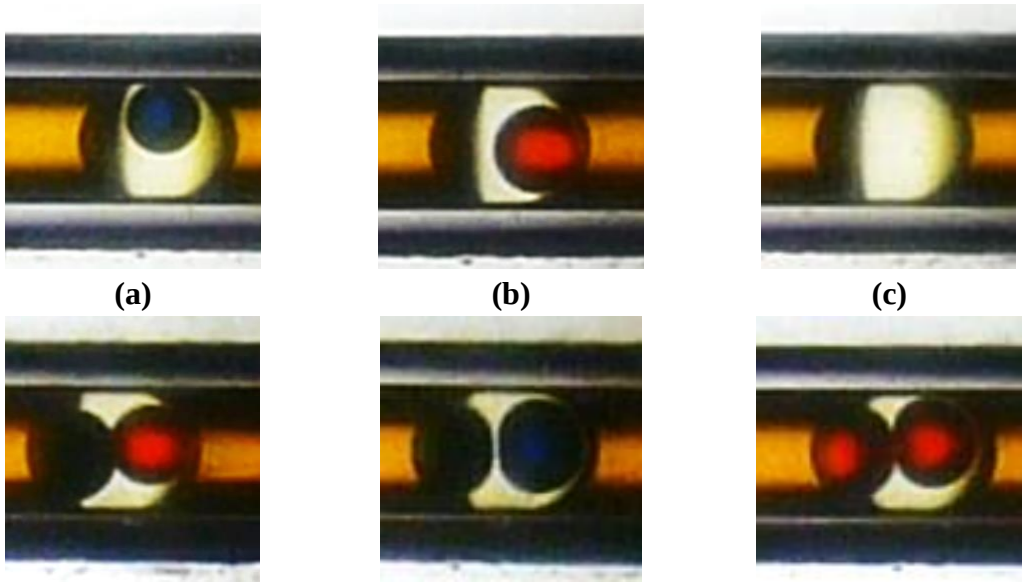

Figure 5-17. Type of encapsulation. (a) Single droplet – 1 blue inner droplet. (b) Single droplet – 1 red inner droplet. (c) Zero encapsulation. (d) Two distinct inner droplets. (e) Two similar droplets – 2 blue inner droplets. (f) Two similar droplets – 2 red inner droplets.

The number of encapsulated droplets were mainly affected by the inner droplets spacing during the pinching process at the downstream. The distance between the inner droplets were affected by the flow rate of middle cooking oil phase. However, the inconsistency of the syringe pump also induce disturbance into the system and hence inconsistent droplet spacing was observed. On top of that, the disruption from the opposed fluid at the upstream also results in unequal spacing between the inner droplets. Hence, the encapsulation pattern was randomised (Figure 5-18).

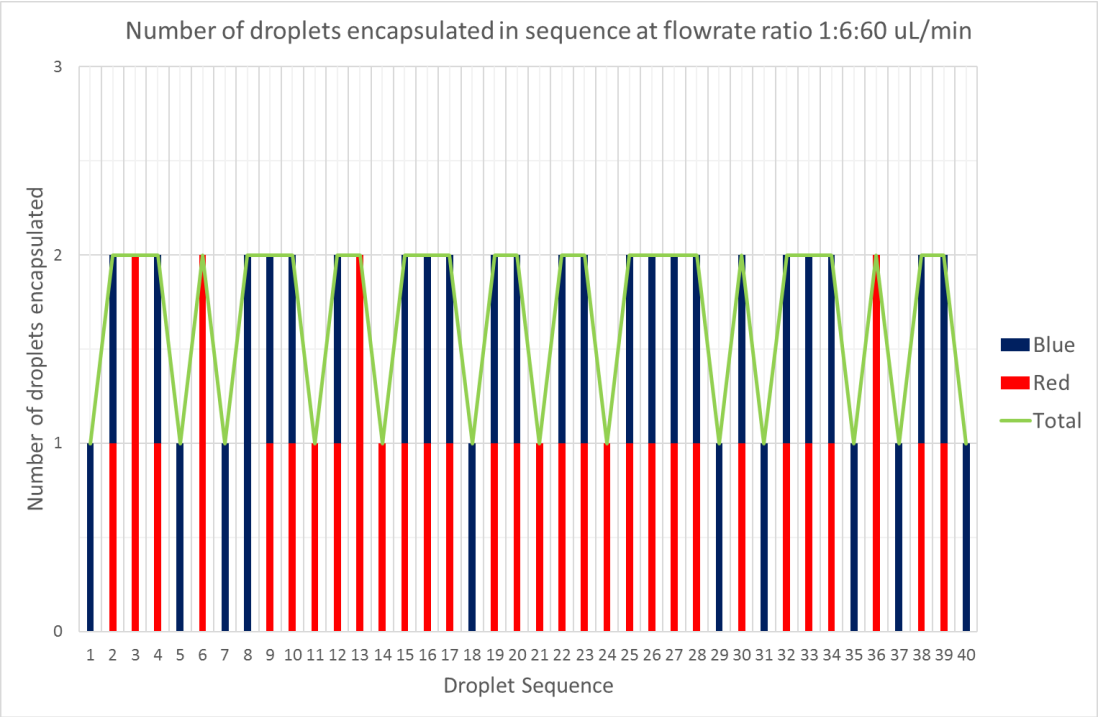

Figure 5-18. Number of droplets encapsulated in sequence at flow rate ratio of 1.6.60 µL/min. (Note: the graph does not show the encapsulation sequence of each inner droplets.)

Experimental data shows inconsistent sequence of the number of encapsulation without a trend to be followed. In addition, the pattern of the encapsulation is random with single droplet encapsulation in between a few double droplets encapsulation. This is mainly caused by the disruption from the opposed fluid at the upstream during the droplet generation, resulting in unequal spacing between the inner droplets. For better illustration and comparisons, the percentage encapsulation for each combination were tabulated in Table 5-4.

Table 5-4: Percentage of encapsulation for each combination.

Flow rate ratio	Ca_{total} (x10^{-4})	φ_{total}	2 distinct [%]	2 similar [%]	Single [%]	Zero [%]	2 total [%]
1:2:40	5.284	0.050	42.5	5	52.5	-	47.5
1:4:40	5.410	0.075	15.0	10.0	65.0	10.0	25
1:6:40	5.536	0.100	40.0	7.5	52.5	-	47.5
1:4:50	6.668	0.060	27.5	2.5	70.0	-	30
1:6:50	6.794	0.080	40.0	10.0	47.5	2.5	50
1:6:60	8.052	0.067	37.5	20.0	42.5	-	57.5
1:8:60	8.178	0.083	15.0	2.5	77.5	5.0	17.5
1:6:70	9.311	0.057	50.0	5.0	45.0	-	55
1:8:70	9.437	0.071	27.5	12.5	60.0	-	40
1:6:80	10.569	0.050	2.5	2.5	92.5	2.5	37.5
1:8:80	10.695	0.063	30.0	2.5	67.5	-	32.5

Ultimately, distinct droplets encapsulation is preferred for better control and application wise. In general, most of the flow rate ratios favour the single droplet encapsulation except at flow rate ratio 1:6:60 µL/min, which has the highest double droplets encapsulation i.e. 57.5%. By increasing the outer aqueous phase, 1:6:70 µL/min encapsulated highest percentage of two distinct droplets (50%), as second highest percentage of double droplets encapsulation i.e. 55%. Comparing among Group A (1:2:40, 1:4:40, 1:6:40), flow rate ratio of 1:4:40 µL/min shows the highest single encapsulation and lowest percentage in double droplets encapsulation, while 1:2:40 and 1:6:40 µL/min obtain similar encapsulation percentage for double droplets and single droplet encapsulation.

As Ca_{total} increases, the viscous force dominates over the interfacial force, the shear stress acting on the dispersed phase by the continuous phase increases. The surface contact between the two fluids increased due to the minimal effect of interfacial tension and hence higher encapsulation of double droplets. However, larger Ca_{total} does not

necessary equivalent to smaller φ_{total} due to the flow rate ratio set. In addition, large Ca_{total} induces hydrodynamic instability since increment of Ca_{total} will shift the flow regime, introducing different mechanism. Hence, the fluctuation in the encapsulation rate for the double droplets encapsulation. On top of that, Q_c was higher when φ_{total} is lower, shearing the droplets at higher frequency with higher monodispersity. Therefore, with sufficiently high Ca_{total}, and low φ_{total}, 1:6:80 µL/min shows highest single droplet encapsulation of 92.5%. On the other hand,1:2:40 µL/min have the same φ_{total} value but Ca_{total} was halved of 1:6:80 µL/min, hence lower single droplet encapsulation (52.5%). This is because the inner droplets were generated under squeezing regime with comparable lower droplets frequency, hence higher double droplets encapsulation rate.

The inner droplets were formed at the upstream, significantly affecting the encapsulation process. Hence Figure 5-19 plotted the encapsulation rate at middle phase flow rate fixed at 6 and 8 µL/min respectively, to further investigate the relationship between Ca_{total} and φ_{total}. At 6 µL/min, the double droplets encapsulation percentage increases with the outer aqueous phase, highest at 1:6:60 µL/min with 57.5% then decreases with reduced φ_{total} (Figure 5-19a). Similar trend was show when middle phase flow rate fixed at 8 µL/min (Figure 5-19b). This shows the number of encapsulation was affected by φ_{total}, where double droplets encapsulation was favourable at optimum φ_{total} of 0.07. To achieve higher encapsulation percentage for double droplets, particularly two distinctive inner droplets, inner phase flow rate should be manipulated as well to further verify the optimum φ_{total} value.

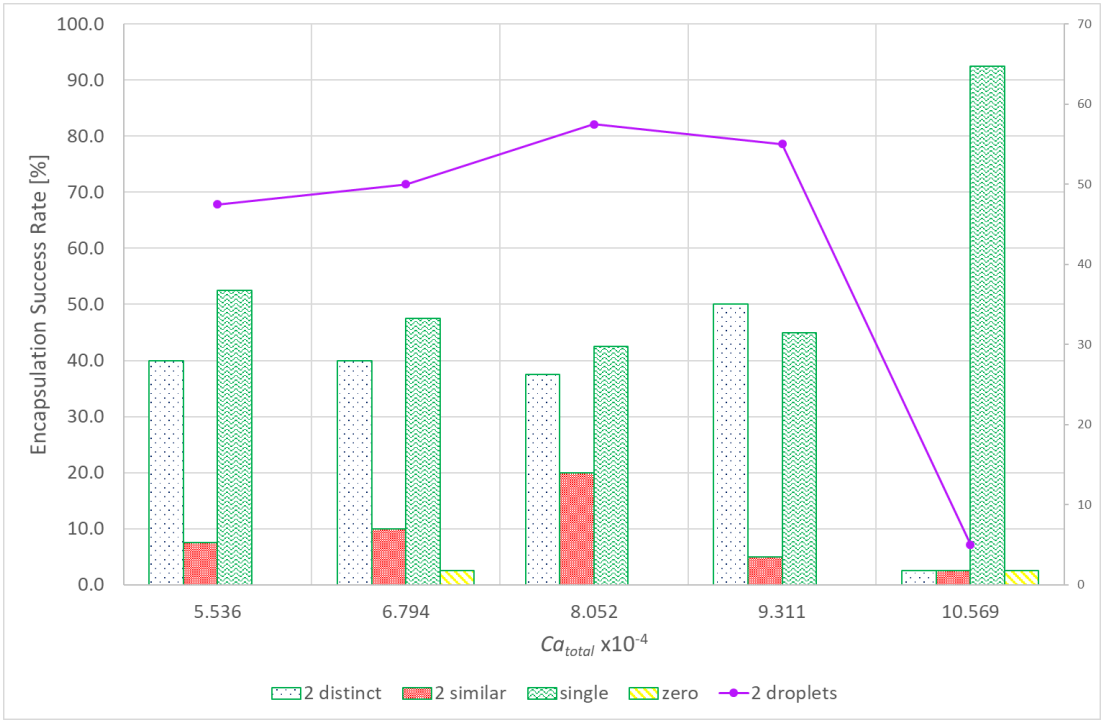

(a)

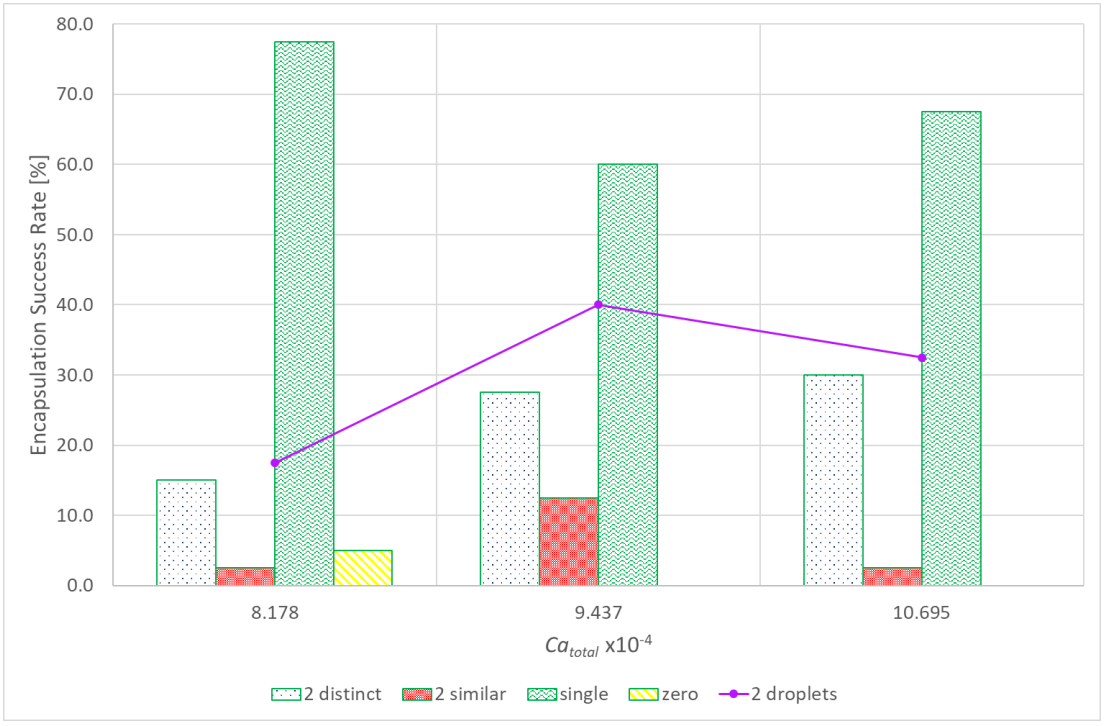

(b)

Figure 5-19. Percentage of encapsulation at middle phase flow rate ratio fixed at (a) 6 µL/min (b) 8 µL/min. 2 droplets were plotted as a total of 2 distinct and 2 similar droplets being encapsulated.

To conclude, a total of 11 flow rate ratios have been conducted to investigate the size of the double emulsion droplets produced in PGHD-A2. Overall, the average double emulsion droplet size produced were in the range of 590 – 730 µm with *CV* value lower

than 5% indicating the monodispersity. Currently, 1.6.80 μL/min produced smallest double emulsion droplets (594 μm) with highest monodispersity (*CV*=0.2%), due to its highest single droplet encapsulation rate (92.5%). Quantitative analysis shows that the droplet size was directly proportional to Ca_{total} and inversely proportional to φ_{total}, consistent with the results reported by Liu and Zhang. Alternating droplet sequencing were highly achievable when the middle phase to outer phase ratio were maintained at 1:10 or above. At high middle to outer phase ratio, the effect from the opposing inner fluid reduces. Although the droplet sequence was interrupted occasionally, but that was mainly due to the flow fluctuations caused by the syringe pumps.

There are 6 combinations of encapsulation observed in the double emulsion droplets produced by PGHD-A2, in which zero encapsulation is recognised as anomalous data. As the Ca_{total} increases, the viscous force dominated the interfacial tension, and hence increasing the range of flow rates that enable droplets generation. The surface area between two immiscible fluid were no longer kept to minimal, increasing the shearing force between two interfaces and hence the increment of double droplets. This, however, was only observed at Ca_{total} less than 9.437. When the Ca_{total} further increases, the hydrodynamic force was unstable, as Ca_{total} directly affects the transition of flow regime. The middle phase flow rate directly affects the droplet formation at the upstream of PGHD. When middle phase was fixed at certain flow rate, manipulating the outer aqueous phase, the double encapsulation rate was highest at φ_{total} of 0.07.

CHAPTER 6: CONCLUSION AND FUTURE WORK

6.1 Conclusion

A simple and low cost PGHD have been developed to produce monodispersed W/O/W double emulsion droplets. The hybrid system was fabricated using a modified Xurography technique, in which the SOP of the fabrication process has been established and optimised. The cutting plotter was optimised to allow precise cutting of channel width as low as 150 μm with a percentage error of 1.1% showing better consistency and precision compared to the reported work. A customised PDMS aligner has been designed to allow precise alignment of two PDMS layer with accurate position of glass capillary tube. With the use of the aligner, the precision error of the capillary tube placement can go as low to 0.4%. The developed SOP for the fabrication scheme and optimised cutting plotter setting was useful as a reference when there is a need to modify the channel geometry, especially with channel width below 200 μm.

Before the PGHD was established and optimised, a series of PGHD have been designed and modified accordingly to overcome the equipment limitations and to simplify the experimental methodology. The geometry design of the PGHD was improved to enable simple experiment start-up and increase the practicability and efficiency of the hybrid system. Quantitative and qualitative analysis have been carried out on PGHD-A and PGHD-A1 for better understanding on the droplet behaviour. The average W/O/W double emulsion droplet size was 784 and 777 μm with *CV* of 3.6 and 3.3% for PGHD-A and PGHD-A1 respectively. Experimental observations show that capillary tube is better positioned at 0.5δ to allow encapsulation process, which was further verified by PGHD-A1a and PGHD-A1b, then leads to the final optimised PGHD-A2. Before the establishment of experimental SOP, the encapsulation process was random due to the improper pumping sequence. Hence, the fluid pumping sequence was reset by taking the

surface properties of the fluid and device material into consideration. The experiment success rate has been increased up to 99%. Besides, the experiment start-up duration reduced significantly and does not required intense attention during the pre-stabilised stage. The flow phenomena and droplet behaviour were further verified using PGHD-A2.

Excluding 1:2:40 µL/min, the average droplet size produced were 514, 505 and 690 µm for inner red, blue and W/O/W double emulsion droplets respectively. The average *CV* of the droplets produced were 3.7, 3.8 and 3.5% respectively for the inner red, blue and W/O/W double emulsion droplets, indicating high monodispersity. By manipulating the flow rate ratio, the number of the encapsulated inner droplets can be controlled. From the research work. 1:6:80 µL/min enabled the highest single droplet encapsulation up to 92.5%, while encapsulation of double inner droplets was highest at 1:6:60 µL/min (57.5%). When the middle flow rate was fixed at 8 µL/min, similar trend was observed. The highest double droplets encapsulation happens when the φ_{total} was 0.07. On the other hand, the alternate droplet sequencing was favoured when the middle to outer flow was at 1:10 ratio or higher. Hence, to achieve higher encapsulation percentage, particularly two distinctive inner droplets, inner phase flow rate should be manipulated to achieve more variation for further verification. The different percentage of encapsulated droplets will be useful for applications such as cell compartment and storage.

Despite the establishment, there are still several limitations which could not be overcome by the developed PGHD due to the material's nature. For example, the chemical incompatibility of PDMS limits its application involving chemical solvent. To overcome, other polymer materials can be used to replace PDMS in fabricating this hybrid device. On top of that, device complexity is limited by the xurography fabrication as it is not mend for micro-scale cutting. Although fine cutting can be carried out through

adjustment of cutting setting, the process requires trial and error and can take up to several hours. The advantages, however lie in the low cost and easy set-up and device fabrication, suitable for researchers restricted by budget. To further improve the system, some of the future works have been recommended in Section 6.2.

6.2 Future Work

Several recommendations of future work to further improve the system were listed:

(1) Limitations of syringe pumps – the characteristics of syringe pumps shows oscillating flow rate, introducing flow disturbance into the system. The oscillating flow rate make insignificant effect for minimum flow rate adjustment. Apart from that, the volume of the syringes limited the achievable flow rate to obtain steady flow system. It is therefore recommended to utilise air pressure pump which enable steady flow profile and allow precise adjustment of flow. Contradicting from the conventional syringe pump, the flow profile of the air pressure pump is consistent within the range of ± 10.

(2) Further verification on φ_{total} of 0.07 to develop an empirical equation/ mathematical model. A mathematical model established the relationship between different variables, allows better understanding on the flow profile in the hybrid system. This will provide a better picture for future reference in manipulating the flow. In this research work, the inner aqueous phase was fixed as constant variable, limiting the flow parameters. Hence, it is recommended to utilise Response Surface Methods (RSM) to design the experiments manipulating inner, middle and outer phase flow rate.

(3) Enhance chemical resistance of PGHD through sol-gel coating technique to exploit wider applications. Current PGHD utilised PDMS as base material, only suitable for biological application. Sol-gel coating technique can be utilised to enhance its chemical

resistance properties, and even modify the system to allow generation of O/W/O double emulsion droplets.

(4) Verify the experiment with numerical simulation. Preliminary simulation was carried out for this research work to provide better understanding on the velocity profile of the droplet encapsulation, however, limited by the computational power, only inner droplets formed at the upstream were obtainable. Numerical simulation provides insight of the droplets formation due to its 3D rotational, unlike experimental work which only allow one-dimensional viewing from the top, limited by the equipment. On top of that, the velocity profile and droplet behaviour at different time scale can be compared. With sufficient computational power, the continuous operation of the system can be simulated for better application in industrial scale.

(5) Repeat experiment with non-Newtonian fluid, or combination of Newtonian/Non-Newtonian fluids. Most of the polymer solutions, useful as precursors to synthesize microparticles are non-Newtonian fluid, hence different technique such that surrounding the non-Newtonian fluid with chaperoning Newtonian fluid is required to form the pre-particle drops [117] Apart from that, double emulsion droplets are very useful in biological application, not to mention the compatibility of the PDMS. Hence, the importance of developing a hybrid system for non-Newtonian fluid to be applied in the industry.

(6) Measure/ control the temperature of the fluids during experimental work to develop larger profile of the hybrid system. Viscosity, a parameter in the calculation of *Ca*, is affected by the temperature and hence a variation of flow profile can be obtained by manipulating it while fixing the φ as constant. On top of that, by manipulating the

temperature of the fluid, microcapsules with core-shell structured, enabling controlled released application can be fabricated.

REFERENCES

[1] A. M. Gañán-Calvo, "Generation of Steady Liquid Microthreads and Micron-Sized Monodisperse Sprays in Gas Streams," *Phys. Rev. Lett.*, vol. 80, no. 2, pp. 285–288, 1998.

[2] T. Thorsen, R. W. Roberts, F. H. Arnold, and S. R. Quake, "Dynamic pattern formation in a vesicle-generating microfluidic device," *Phys. Rev. Lett.*, vol. 86, no. 18, pp. 4163–4166, 2001.

[3] M. G. Simon and A. P. Lee, "Microfluidic Droplet Manipulations and Their Applications," in *Microdroplet Technology Principles and Emerging Applications in Biology and Chemistry*, P. Day, A. Manz, and Y. Zhang, Eds. Springer New York Heidelberg Dordrecht London, 2012, pp. 23–51.

[4] M. Chabert, K. D. Dorfman, and J. L. Viovy, "Droplet fusion by alternating current (AC) field electrocoalescence in microchannels," *Electrophoresis*, vol. 26, no. 19, pp. 3706–3715, 2005.

[5] Y. Wang, P. Wu, Z. Luo, Y. Li, M. Liao, Y. Li and L. He, "Controllable geometry-mediated droplet fission using 'off-the- shelf' capillary microfluidics device," *RSC Adv.*, vol. 4, no. 59, pp. 31184–31187, Jul. 2014.

[6] H. Song, J. D. Tice, and R. F. Ismagilov, "A microfluidic system for controlling reaction networks in time," *Angew. Chemie - Int. Ed.*, vol. 42, no. 7, pp. 768–772, 2003.

[7] L. Mazutis, J. Gilbert, W. L. Ung, D. a Weitz, A. D. Griffiths, and J. a Heyman,

"Single-cell analysis and sorting using droplet-based microfluidics.," *Nat. Protoc.*, vol. 8, no. 5, pp. 870–91, 2013.

[8] T. Nisisako and T. Torii, "Formation of Biphasic Janus Droplets in a Microfabricated Channel for the Synthesis of Shape-Controlled Polymer Microparticles," *Adv. Mater.*, vol. 19, no. 11, pp. 1489–1493, Jun. 2007.

[9] A. S. Utada, E. Lorenceau, D. R. Link, P. D. Kaplan, H. A. Stone, and D. A. Weitz, "Monodisperse double emulsions generated from a microcapillary device," *Science (80-.).*, vol. 308, no. 5721, pp. 537–541, 2005.

[10] T. Kong, J. Wu, K. W. K. Yeung, M. K. T. To, H. C. Shum, and L. Wang, "Microfluidic fabrication of polymeric core-shell microspheres for controlled release applications," *Biomicrofluidics*, vol. 7, no. 4, pp. 1–9, 2013.

[11] T. Kong, L. Wang, H. M. Wyss, and H. C. Shum, "Capillary micromechanics for core-shell particles.," *Soft Matter*, vol. 10, no. 18, pp. 3271–6, 2014.

[12] A. M. Gañán-Calvo and J. M. Gordillo, "Perfectly monodisperse microbubbling by capillary flow focusing.," *Phys. Rev. Lett.*, vol. 87, no. 27, p. 274501, 2001.

[13] P. Garstecki, I. Gitlin, W. Diluzio, G. M. Whitesides, E. Kumacheva, and H. A. Stone, "Formation of monodisperse bubbles in a microfluidic flow-focusing device," *Appl. Phys. Lett.*, vol. 85, no. 13, pp. 2649–2651, 2004.

[14] J. H. Xu, S. W. Li, Y. J. Wang, and G. S. Luo, "Controllable gas-liquid phase flow patterns and monodisperse microbubbles in a microfluidic T-junction device," *Appl. Phys. Lett.*, vol. 88, no. 13, p. 133506, Mar. 2006.

[15] S.-Y. Teh, R. Lin, L.-H. Hung, and A. P. Lee, “Droplet microfluidics.,” *Lab Chip*, vol. 8, no. 2, pp. 198–220, 2008.

[16] W. Seifriz, “Studies in emulsions III. Double reversal of oil emulsions occasioned by the same electrolyte,” *J. Phys. Chem.*, vol. 29, no. 6, pp. 738–749, 1925.

[17] S. Matsumoto, Y. Kita, and D. Yonezawa, “An attempt at preparing water-in-oil-in-water multiple-phase emulsions,” *J. Colloid Interface Sci.*, vol. 57, no. 2, pp. 353–361, Nov. 1976.

[18] L.Y. Chu, A. S. Utada, R. K. Shah, J.W. Kim, and D. A. Weitz, “Controllable Monodisperse Multiple Emulsions,” *Angew. Chemie*, vol. 119, no. 47, pp. 9128–9132, 2007.

[19] P. B. Umbanhowar, V. Prasad, and D. A. Weitz, “Monodisperse emulsion generation via drop break off in a coflowing stream,” *Langmuir*, vol. 16, no. 2, pp. 347–351, 2000.

[20] N. Shembekar, C. Chaipan, R. Utharala, and C. A. Merten, “Droplet-based microfluidics in drug discovery, transcriptomics and high-throughput molecular genetics.,” *Lab Chip*, vol. 16, no. 8, pp. 1314–31, Apr. 2016.

[21] E. Kumacheva and P. Garstecki, “Applications of polymer particles,” in *Microfluidic reactors for polymer particles*, Wiley, 2011, p. 476.

[22] H. C. Shum, A. Bandyopadhyay, S. Bose, and D. A. Weitz, “Double emulsion droplets as microreactors for synthesis of mesoporous hydroxyapatite,” *Chem. Mater.*, vol. 21, no. 22, pp. 5548–5555, 2009.

[23] M. Zhang, W. Wang, R. Xie, X. Ju, Z. Liu, L. Jiang, Q. Chen and L.Y. Chu, "Controllable microfluidic strategies for fabricating microparticles using emulsions as templates," *Particuology*, vol. 24, pp. 18–31, 2016.

[24] R. Dreyfus, P. Tabeling, and H. Willaime, "Ordered and Disordered Patterns in Two-Phase Flows in Microchannels," *Phys. Rev. Lett.*, vol. 90, no. 14, p. 4, 2003.

[25] J. Zhou, D. a. Khodakov, A. V. Ellis, and N. H. Voelcker, "Surface modification for PDMS-based microfluidic devices," *Electrophoresis*, vol. 33, no. 1, pp. 89–104, 2012.

[26] T. Nisisako, S. Okushima, and T. Torii, "Controlled formulation of monodisperse double emulsions in a multiple-phase microfluidic system," *Soft Matter*, vol. 1, no. 1, p. 23, 2005.

[27] S. Okushima, T. Nisisako, T. Torii, and T. Higuchi, "Controlled production of monodisperse double emulsions by two-step droplet breakup in microfluidic devices," *Langmuir*, vol. 20, no. 23, pp. 9905–9908, 2004.

[28] R. K. Shah, H. C. Shum, A. C. Rowat, D. Lee, J. J. Agresti, A. S. Utada, L. Y. Chu, J. W. Kim, A. Fernandez-Nieves, C. J. Martinez and D. A. Weitz, "Designer emulsions using microfluidics," *Mater. Today*, vol. 11, no. 4, pp. 18–27, 2008.

[29] A. R. Abate and D. A. Weitz, "High-order multiple emulsions formed in poly(dimethylsiloxane) microfluidics," *Small*, vol. 5, no. 18, pp. 2030–2032, 2009.

[30] N.N. Deng, Z. J. Meng, R. Xie, X. J. Ju, C. L. Mou, W. Wang and L. Y. Chu, "Simple and cheap microfluidic devices for the preparation of monodisperse emulsions," *Lab Chip*, vol. 11, no. 23, p. 3963, 2011.

[31] C.H. Choi, H. Wang, H. Lee, J. H. Kim, L. Zhang, A. Mao, D. J. Mooney and D. A. Weitz, "One-step generation of cell-laden microgels using double emulsion drops with a sacrificial ultra-thin oil shell.," *Lab Chip*, vol. 16, no. 9, pp. 1549–55, Apr. 2016.

[32] P.-G. de. Gennes, F. Brochard-Wyart, and D. Quéré, *Capillarity and wetting phenomena : drops, bubbles, pearls, waves*. Springer, 2004.

[33] E. Kumacheva and P. Garstecki, *Microfluidic reactors for polymer particles*. Wiley, 2011.

[34] A. S. Utada, A. Fernandez-Nieves, H. A. Stone, and D. A. Weitz, "Dripping to Jetting Transitions in Coflowing Liquid Streams," *Phys. Rev. Lett.*, vol. 99, no. 9, p. 094502, Aug. 2007.

[35] P. Tirandazi and C. H. Hidrovo, "Liquid-in-gas droplet microfluidics; experimental characterization of droplet morphology, generation frequency, and monodispersity in a flow-focusing microfluidic device," *J. Micromechanics Microengineering*, vol. 27, no. 7, p. 075020, Jul. 2017.

[36] A. Jillavenkatesa, S. J. Dapkunas, and L.-S. H. Lum, "Particle Size Characterization," *NIST Spec. Publ.*, vol. 960, no. 1, p. 164, 2001.

[37] S. Takeuchi, P. Garstecki, D. B. Weibel, and G. M. Whitesides, "An axisymmetric flow-focusing microfluidic device," *Adv. Mater.*, vol. 17, no. 8, pp. 1067–1072, 2005.

[38] M. De Menech, P. Garstecki, F. Jousse, and H. A. Stone, "Transition from squeezing to dripping in a microfluidic T-shaped junction," *J. Fluid Mech.*, vol.

595, pp. 141–161, 2008.

[39] S. van der Graaf, M. L. J. Steegmans, R. G. M. van der Sman, C. G. P. H. Schroën, and R. M. Boom, “Droplet formation in a T-shaped microchannel junction: A model system for membrane emulsification,” *Colloids Surfaces A Physicochem. Eng. Asp.*, vol. 266, no. 1–3, pp. 106–116, Sep. 2005.

[40] S. Van Der Graaf, T. Nisisako, C. G. P. H. Schroën, R. G. M. Van Der Sman, and R. M. Boom, “Lattice Boltzmann simulations of droplet formation in a T-shaped microchannel,” *Langmuir*, vol. 22, no. 9, pp. 4144–4152, 2006.

[41] P. Garstecki, M. J. Fuerstman, H. A. Stone, and G. M. Whitesides, “Formation of droplets and bubbles in a microfluidic T-junction-scaling and mechanism of break-up.,” *Lab Chip*, vol. 6, no. 3, pp. 437–446, 2006.

[42] E. Kumacheva and P. Garstecki, “Formation of Droplets in Microfluidic Systems,” in *Microfluidic Reactors for Polymer Particles*, Chichester, UK: John Wiley & Sons, Ltd, 2011, p. 55.

[43] H. Liu and Y. Zhang, “Droplet formation in a T-shaped microfluidic junction,” *J. Appl. Phys.*, vol. 106, no. 3, 2009.

[44] J. K. Nunes, S S H Tsai, J. Wan, and H. A. Stone, “Dripping and jetting in microfluidic multiphase flows applied to particle and fiber synthesis,” *J Phys D Appl Phys.*, vol. 46, no. 11, pp. 1–6, 2013.

[45] J. H. Xu, S. W. Li, J. Tan, and G. S. Luo, “Correlations of droplet formation in T-junction microfluidic devices: from squeezing to dripping,” *Microfluid Nanofluid*, vol. 5, pp. 711–717, 2008.

[46] J. H. Xu, S. W. Li, J. Tan, Y. J. Wang, and G. S. Luo, “Controllable preparation of monodisperse O/W and W/O emulsions in the same microfluidic device,” *Langmuir*, vol. 22, no. 19, pp. 7943–7946, 2006.

[47] J. H. Xu, S. W. Li, J. Tan, Y. J. Wang, and G. S. Luo, “Preparation of highly monodisperse droplet in a T-junction microfluidic device,” *AIChE J.*, vol. 52, no. 9, pp. 3005–3010, Sep. 2006.

[48] J. H. Xu, G. S. Luo, S. W. Li, and G. G. Chen, “Shear force induced monodisperse droplet formation in a microfluidic device by controlling wetting properties,” *Lab Chip*, vol. 6, no. 1, pp. 131–136, 2006.

[49] J. Tan, J. H. Xu, S. W. Li, and G. S. Luo, “Drop dispenser in a cross-junction microfluidic device: Scaling and mechanism of break-up,” *Chem. Eng. J.*, vol. 136, no. 2–3, pp. 306–311, 2008.

[50] V. Mansard, J. M. Mecca, D. L. Dermody, D. Malotky, C. J. Tucker, and T. M. Squires, “Collective Rayleigh-Plateau Instability: A Mimic of Droplet Breakup in High Internal Phase Emulsion,” *Langmuir*, vol. 32, no. 11, pp. 2549–2555, Mar. 2016.

[51] K. F. Lei, “Materials and Fabrication Techniques for Nano- and Microfluidic Devices,” in *Microfluidics in Detection Science*, F. H. Labeed and H. O. Fatoyinbo, Eds. Cambridge: Royal Society of Chemistry, 2014, pp. 1–28.

[52] K. E. Petersen, “Silicon as a mechanical material,” *Proc. IEEE*, vol. 70, no. 5, pp. 420–457, 1982.

[53] A. Daridon, V. Fascio, J. Lichtenberg, R. Wutrich, H. Langen, E. Verpoorte and

N. F. Rooij, “Multi-layer microfluidic glass chips for microanalytical applications,” *Fresenius. J. Anal. Chem.*, vol. 371, no. 2, pp. 261–269, Sep. 2001.

[54] M. A. Unger, H. P. Chou, T. Thorsen, A. Scherer, and S. R. Quake, “Monolithic microfabricated valves and pumps by multilayer soft lithography.,” *Science*, vol. 288, no. 5463, pp. 113–6, Apr. 2000.

[55] S. C. Terry, J. H. Herman, and J. B. Angell, “A gas chromatographic air analyzer fabricated on a silicon wafer,” *IEEE Trans. Electron Devices*, vol. 26, no. 12, pp. 1880–1886, 1979.

[56] D. R. Reyes, D. Iossifidis, P. A. Auroux, and A. Manz, “Micro total analysis systems. 1. Introduction, theory, and technology,” *Anal. Chem.*, vol. 74, no. 12, pp. 2623–2636, 2002.

[57] G. M. Whitesides, “The origins and the future of microfluidics.,” *Nature*, vol. 442, no. 7101, pp. 368–73, Jul. 2006.

[58] P. Pal and K. Sato, “Various shapes of silicon freestanding microfluidic channels and microstructures in one-step lithography,” *J. Micromechanics Microengineering*, vol. 19, no. 5, p. 055003, May 2009.

[59] F. Marty, L. Rousseau, B. Saadany, B. Mercier, O. Francais, Y. Mita and T. Bourouina, “Advanced etching of silicon based on deep reactive ion etching for silicon high aspect ratio microstructures and three-dimensional micro- and nanostructures,” *Microelectronics J.*, vol. 36, no. 7, pp. 673–677, Jul. 2005.

[60] K. Ren, J. Zhou, and H. Wu, “Materials for microfluidic chip fabrication,” *Acc. Chem. Res.*, vol. 46, no. 11, pp. 2396–2406, 2013.

[61] P. J. A. Kenis, R. F. Ismagilov, S. Takayama, G. M. Whitesides, S. Li, and H. S. White, “Fabrication inside Microchannels Using Fluid Flow,” *Acc. Chem. Res.*, vol. 33, no. 12, pp. 841–847, Dec. 2000.

[62] S. Marre and K. F. Jensen, “Synthesis of micro and nanostructures in microfluidic systems,” *Chem. Soc. Rev.*, vol. 39, no. 3, p. 1183, 2010.

[63] J. C. Love, J. R. Anderson, and G. M. Whitesides, “Fabrication of Three-Dimensional Microfluidic Systems by Soft Lithography,” *Mater. Res. Soc.*, no. July, pp. 523–528, 2001.

[64] R. F. Ismagilov, D. Rosmarin, P. J. A. Kenis, D. T. Chiu, W. Zhang, H. A. Stone and G. M. Whitesides, “Pressure-driven laminar flow in tangential microchannels: An elastomeric microfluidic switch,” *Anal. Chem.*, vol. 73, no. 19, pp. 4682–4687, 2001.

[65] J. R. Anderson, D. T. Chiu, R. J. Jackman, O. Cherniavskaya, J. C. Mcdonald, H. Wu, S. H. Whitesides and G. M. Whitesides, “Fabrication of Topologically Complex Three-Dimensional Microfluidic Systems in PDMS by Rapid Prototyping Fabrication of Topologically Complex Three-Dimensional Microfluidic Systems in PDMS by Rapid Prototyping,” *Anal. Chem.*, vol. 72, no. 14, pp. 3158–3164, 2000.

[66] K. Zhou, X. G. Zhu, Y. Li, and J. Liu, “Fabrication of PDMS micro through-holes using micromolding in open capillaries,” *RSC Adv.*, vol. 4, no. 60, pp. 31988–31993, 2014.

[67] M. W. L. Watson, M. Abdelgawad, G. Ye, N. Yonson, J. Trottier, and A. R.

Wheeler, “Microcontact printing-based fabrication of digital microfluidic devices,” *Anal. Chem.*, vol. 78, no. 22, pp. 7877–7885, 2006.

[68] J. Cooper McDonald and George M. Whitesides, “Poly(dimethylsiloxane) as a Material for Fabricating Microfluidic Devices,” *Acc. Chem. Res.*, vol. 35, no. 7, pp. 491–499, 2002.

[69] Abraham D. Stroock and George M. Whitesides, “Controlling Flows in Microchannels with Patterned Surface Charge and Topography,” *Acc. Chem. Res.*, vol. 36, no. 8, pp. 597–604, 2003.

[70] X. Mu, W. Zheng, J. Sun, W. Zhang, and X. Jiang, “Microfluidics for Manipulating Cells,” *Small*, vol. 9, no. 1, pp. 9–21, Jan. 2013.

[71] A. Khademhosseini, R. Langer, J. Borenstein, and J. P. Vacanti, “Microscale technologies for tissue engineering and biology.,” *Proc. Natl. Acad. Sci. U. S. A.*, vol. 103, no. 8, pp. 2480–7, Feb. 2006.

[72] J. El-Ali, P. K. Sorger, and K. F. Jensen, “Cells on chips,” *Nature*, vol. 442, no. 7101, pp. 403–411, Jul. 2006.

[73] S. Vudayagiri, M. D. Junker, and A. L. Skov, “Factors affecting the surface and release properties of thin polydimethylsiloxane films,” *Polym. J.*, vol. 45, no. 8, pp. 871–878, 2013.

[74] J. C. McDonald, D. C. Duffy, J. R. Anderson, D. T. Chiu, H. Wu, O. J. A. Schueller and G. M. Whitesides, “Fabrication of microfluidic systems in poly(dimethylsiloxane),” *Electrophoresis*, vol. 21, pp. 27–40, 2000.

[75] D. A. Bartholomeusz, R. W. Boutté, and J. D. Andrade, “Xurography: Rapid prototyping of microstructures using a cutting plotter,” *J. Microelectromechanical Syst.*, vol. 14, no. 6, pp. 1364–1374, 2005.

[76] R.R. Meehan, J. Kumar, M. Earl, E. Svenson, and S.J. Burns, “The role of blade sharpness in cutting instabilities of polyethylene terephthalate,” *J. Mater. Sci. Lett.*, vol. 18, pp. 93–95, 1999.

[77] C. Arcona and T. A. Dow, “The role of knife sharpness in the slitting of plastic films,” *J. Mater. Sci.*, vol. 31, no. 5, pp. 1327–1334, 1996.

[78] R. R. Meehan and S. J. Burns, “Mechanics of slitting and cutting webs,” *Exp. Mech.*, vol. 38, no. 2, pp. 103–109, Jun. 1998.

[79] P. K. Yuen and V. N. Goral, “Low-cost rapid prototyping of flexible microfluidic devices using a desktop digital craft cutter,” *Lab Chip*, vol. 10, no. 3, pp. 384–387, 2010.

[80] J. Do, J. Y. Zhang, and C. M. Klapperich, “Maskless writing of microfluidics: Rapid prototyping of 3D microfluidics using scratch on a polymer substrate,” *Robot. Comput. Integr. Manuf.*, vol. 27, no. 2, pp. 245–248, 2011.

[81] J. Atencia, G. A. Cooksey, and L. E. Locascio, “A robust diffusion-based gradient generator for dynamic cell assays,” *Lab Chip*, vol. 12, no. 2, pp. 309–316, 2012.

[82] P. P. de Santana, T. P. Segato, E. Carrilho, R. S. Lima, N. Dossi, M. Y. Kamogawa, A. L. Gobbi M. H. Piazzeta and E. Piccin, “Fabrication of glass microchannels by xurography for electrophoresis applications,” *Analyst*, vol. 138, no. 6, p. 1660, 2013.

[83] M. Islam, R. Natu, and R. Martinez-Duarte, “A study on the limits and advantages of using a desktop cutter plotter to fabricate microfluidic networks,” *Microfluid. Nanofluidics*, vol. 19, no. 4, pp. 973–985, 2015.

[84] E. Pinto, V. Faustino, R. O. Rodrigues, D. Pinho, V. Garcia, J. M. Miranda and R. Lima, “A rapid and low-cost nonlithographic method to fabricate biomedical microdevices for blood flow analysis,” *Micromachines*, vol. 6, no. 1, pp. 121–135, 2015.

[85] S. Cosson, L. G. Aeberli, N. Brandenberg, and M. P. Lutolf, “Ultra-rapid prototyping of flexible, multi-layered microfluidic devices via razor writing,” *Lab Chip*, vol. 15, no. 1, pp. 72–76, 2015.

[86] W. Wang, R. Xie, X. J. Ju, T. Luo, L. Liu, D. A. Weitz and L. Y. Chu, “Controllable microfluidic production of multicomponent multiple emulsions,” *Lab Chip*, vol. 11, no. 9, p. 1587, 2011.

[87] “What is Photolithography?” [Online]. Available: http://www.tech-faq.com/photolithography.html. [Accessed: 03-Apr-2018].

[88] S. L. Anna, N. Bontoux, and H. a. Stone, “Formation of dispersions using ‘flow focusing’ in microchannels,” *Appl. Phys. Lett.*, vol. 82, no. 3, pp. 364–366, 2003.

[89] M. Joanicot and A. Ajdari, “Droplet control for microfluidics.,” *Science (80-.).*, vol. 309, no. 5736, pp. 887–888, Aug. 2005.

[90] P. Garstecki, H. A. Stone, and G. M. Whitesides, “Mechanism for Flow-Rate Controlled Breakup in Confined Geometries: A Route to Monodisperse Emulsions,” *Phys. Rev. Lett.*, vol. 94, no. 16, p. 164501, Apr. 2005.

[91] J. D. Tice, H. Song, A. D. Lyon, and R. F. Ismagilov, “Formation of Droplets and Mixing in Multiphase Microfluidics at Low Values of the Reynolds and the Capillary Numbers,” *Langmuir*, vol. 19, no. 22, pp. 9127–9133, 2003.

[92] J. D. Tice, R. F. Ismagilov, and B. Zheng, “Formation of droplets of alternating composition in microfluidic channels and applications to indexing of concentrations in droplet-based assays,” *Anal. Chem.*, vol. 76, no. 17, pp. 4977–4982, 2004.

[93] P. Guillot and A. Colin, “Stability of parallel flows in a microchannel after a T junction,” *Phys. Rev. E*, vol. 72, no. 6, p. 066301, Dec. 2005.

[94] A. Rotem, A. R. Abate, A. S. Utada, V. Van Steijn, and D. A. Weitz, “Drop formation in non-planar microfluidic devices,” *Lab Chip*, vol. 12, no. 21, p. 4263, 2012.

[95] T. Li, L. Zhao, W. Liu, J. Xu, and J. Wang, “Simple and reusable off-the-shelf microfluidic devices for the versatile generation of droplets,” *Lab Chip*, vol. 16, no. 24, pp. 4718–4724, 2016.

[96] A. J. L. Morgan, L. H. S. Jose, W. D. Jamieson, J. M. Wymant, B. Song, P. Stephens, D. A. Barrow and O. K. Castell, “Simple and versatile 3D printed microfluidics using fused filament fabrication,” *PLoS One*, vol. 11, no. 4, pp. 1–17, 2016.

[97] B. Zheng, J. D. Tice, and R. F. Ismagilov, “Formation of arrayed droplets by soft lithography and two-phase fluid flow, and application in protein crystallization,” *Adv. Mater.*, vol. 16, no. 15 SPEC. ISS., pp. 1365–1368, 2004.

[98] J. Thiele, A. R. Abate, H. C. Shum, S. Bachtler, S. Förster, and D. A. Weitz, "Fabrication of polymersomes using double-emulsion templates in glass-coated stamped microfluidic devices," *Small*, vol. 6, no. 16, pp. 1723–1727, 2010.

[99] D. E. Discher and A. Eisenberg, "Polymer Vesicles," *Science (80-.).*, vol. 297, no. 5583, pp. 967–973, Aug. 2002.

[100] B. M. Discher *et al.*, "Polymersomes: tough vesicles made from diblock copolymers.," *Science*, vol. 284, no. 5417, pp. 1143–6, May 1999.

[101] K. Kita-Tokarczyk, J. Grumelard, T. Haefele, and W. Meier, "Block copolymer vesicles—using concepts from polymer chemistry to mimic biomembranes," *Polymer (Guildf).*, vol. 46, pp. 3540–3563, 2005.

[102] G. Nurumbetov, N. Ballard, and S. A. F. Bon, "A simple microfluidic device for fabrication of double emulsion droplets and polymer microcapsules," *Polym. Chem.*, vol. 3, no. 4, p. 1043, 2012.

[103] D. Li, X. Li, C. Chen, Z. Zheng, and H. Chang, "Monodisperse water-in-oil-in-water emulsions generation for synthesising alginate hydrogel microspheres via locally hydrophobic modification to PMMA microchannels," *Sensors Actuators, B Chem.*, vol. 255, pp. 1048–1056, 2018.

[104] S. Bhattacharya, A. Datta, J. M. Berg, and S. Gangopadhyay, "Studies on surface wettability of poly(dimethyl) siloxane (PDMS) and glass under oxygen-plasma treatment and correlation with bond strength," *J. Microelectromechanical Syst.*, vol. 14, no. 3, pp. 590–597, Jun. 2005.

[105] J. Zhou, A. V. Ellis, and N. H. Voelcker, "Recent developments in PDMS surface

modification for microfluidic devices," *Electrophoresis*, vol. 31, no. 1, pp. 2–16, 2010.

[106] A. Abate, A. Krummel, D. Lee, M. Marquez, C. Holtze, and D. A. Weitz, "Photoreactive coating for high-contrast spatial patterning of microfluidic device wettability," *Lab Chip*, vol. 8, pp. 2157–2160, 2008.

[107] W. J. Duncanson, A. Abbaspourrad, H. C. Shum, S. H. Kim, L. L. A. Adams, and D. A. Weitz, "Monodisperse gas-filled microparticles from reactions in double emulsions," *Langmuir*, vol. 28, no. 17, pp. 6742–6745, 2012.

[108] C. N. Lim, K. S. Koh, Y. Ren, J. K. Chin, Y. Shi, and Y. Yan, "Analysis of liquid-liquid droplets fission and encapsulation in single/two layer microfluidic devices fabricated by xurographic method," *Micromachines*, vol. 8, no. 2, 2017.

[109] J. N. Lee, C. Park, and G. M. Whitesides, "Solvent Compatibility of Poly(dimethylsiloxane)-Based Microfluidic Devices," *Anal. Chem.*, vol. 75, no. 23, pp. 6544–6554, 2003.

[110] J. C. Stull, A. Erenberg, and R. D. Leff, "Flow rate variability from electronic infusion devices.," *Crit. Care Med.*, vol. 16, no. 9, pp. 888–91, Sep. 1988.

[111] Y. Zhang and H. Liu, "Physics of multiphase microflows and microdroplets," in *Microdroplet Technology: Principles and Emerging Applications in Biology and Chemistry*, Philip Day, Andreas Manz, and Yonghao Zhang, Eds. Verlag New York: Springer, 2012, pp. 1–21.

[112] N. Otsu, "A Threshold Selection Method from Gray-Level Histograms," *IEEE Trans. Syst. Man. Cybern.*, vol. 9, no. 1, pp. 62–66, 1979.

[113] J. Kittler and J. Illingworth, “Minimum error thresholding,” *Pattern Recognit.*, vol. 19, no. 1, pp. 41–47, 1986.

[114] A. R. Abate, A. Poitzsch, Y. Hwang, J. Lee, J. Czerwinska, and D. A. Weitz, “Impact of inlet channel geometry on microfluidic drop formation,” *Phys. Rev. E - Stat. Nonlinear, Soft Matter Phys.*, vol. 80, no. 2, pp. 1–5, 2009.

[115] Z. Li, S. Y. Mak, A. Sauret, and H. C. Shum, “Syringe-pump-induced fluctuation in all-aqueous microfluidic system implications for flow rate accuracy,” *Lab Chip*, vol. 14, no. 4, pp. 744–749, 2014.

[116] L. Peng, M. Yang, S. Guo, W. Liu, and X. Zhao, “The effect of interfacial tension on droplet formation in flow-focusing microfluidic device,” *Biomed. Microdevices*, vol. 13, no. 3, pp. 559–564, Jun. 2011.

[117] A. R. Abate, M. Kutsovsky, S. Seiffert, M. Windbergs, L. F. V. Pinto, A. Rotem, A. S. Utada and D. A. Weitz, “Synthesis of Monodisperse Microparticles from Non-Newtonian Polymer Solutions with Microfluidic Devices,” *Adv. Mater.*, vol. 23, no. 15, pp. 1757–1760, Apr. 2011.

APPENDIX A.1: FLUID PROPERTIES – CONTACT ANGLE

Surface tension results | Contact angle results

No.	Time	Theta (L)	Theta (R)	Theta (Avg)	Dev.	Height	Width	Area	Volume
Experiment: 147963			Start at: 11:16:48 PM						
1	0.006	46.36	40.45	43.40	2.96	1.037	6.024	31.53	15.35
2	59.95	45.55	40.22	42.89	2.67	1.023	6.030	31.62	15.33
3	119.9	44.82	41.16	42.99	1.83	1.012	6.034	31.64	15.36
4	179.9	44.30	41.69	43.00	1.31	1.001	6.037	31.62	15.30
5	239.9	43.71	42.67	43.19	0.52	0.990	6.039	31.60	15.24
6	300.0	43.16	42.93	43.05	0.12	0.982	6.041	31.54	15.10
7	359.9	42.93	42.98	42.95	0.03	0.977	6.042	31.51	15.04
8	419.9	42.86	43.13	42.99	0.13	0.974	6.043	31.49	14.98
9	479.9	42.21	42.73	42.47	0.26	0.971	6.068	31.72	15.02
10	539.9	42.13	42.90	42.52	0.39	0.968	6.072	31.70	14.99
	Mean:	43.80	42.09	42.95	1.02	0.993	6.043	31.60	15.17
Std.dev.:		0.45	0.35	0.09	0.35	0.008	0.005	0.02	0.05

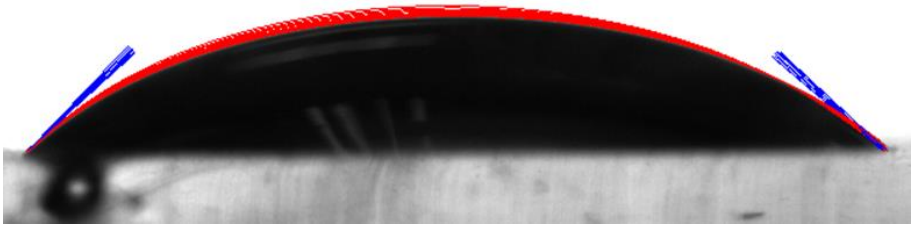

Figure 6-1. Contact Angle of Cooking Oil on PDMS Layer

Surface tension results | Contact angle results

No.	Time	Theta (L)	Theta (R)	Theta (Avg)	Dev.	Height	Width	Area	Volume
Experiment: 123456789			Start at: 10:53:21 PM						
1	0.014	105.62	103.71	104.67	0.96	1.967	3.264	21.00	12.62
2	59.95	105.62	103.86	104.74	0.88	1.948	3.263	20.80	12.45
3	119.9	104.64	105.23	104.93	0.30	1.915	3.265	20.48	12.18
4	179.9	103.71	104.26	103.99	0.28	1.883	3.292	20.25	12.00
5	239.9	102.53	103.30	102.91	0.39	1.855	3.320	20.06	11.86
6	299.9	101.60	102.39	102.00	0.39	1.834	3.331	19.86	11.69
7	359.9	101.26	101.66	101.46	0.20	1.813	3.340	19.66	11.53
8	419.9	100.41	100.75	100.58	0.17	1.795	3.348	19.48	11.39
9	479.9	100.23	99.71	99.97	0.26	1.782	3.353	19.33	11.26
10	539.9	99.98	99.13	99.56	0.43	1.770	3.356	19.21	11.16
	Mean:	102.56	102.40	102.48	0.42	1.856	3.313	20.01	11.81
Std.dev.:		0.70	0.64	0.65	0.09	0.022	0.012	0.19	0.16

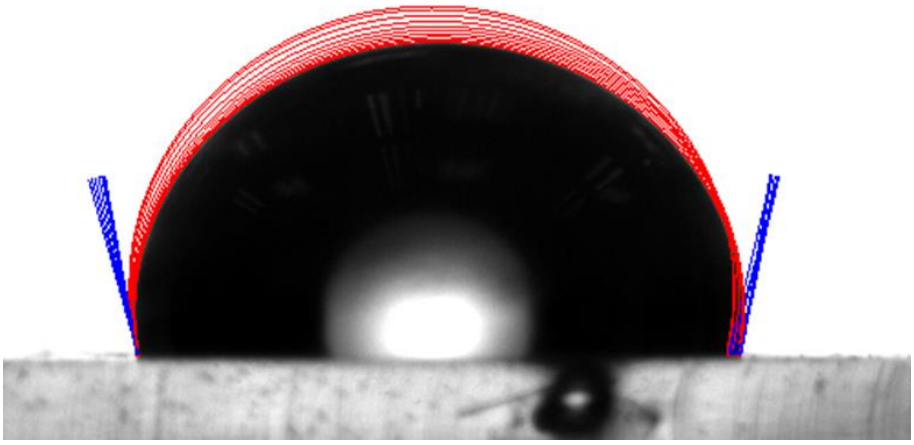

Figure 6-2. Contact Angle of DI Water on PDMS Layer

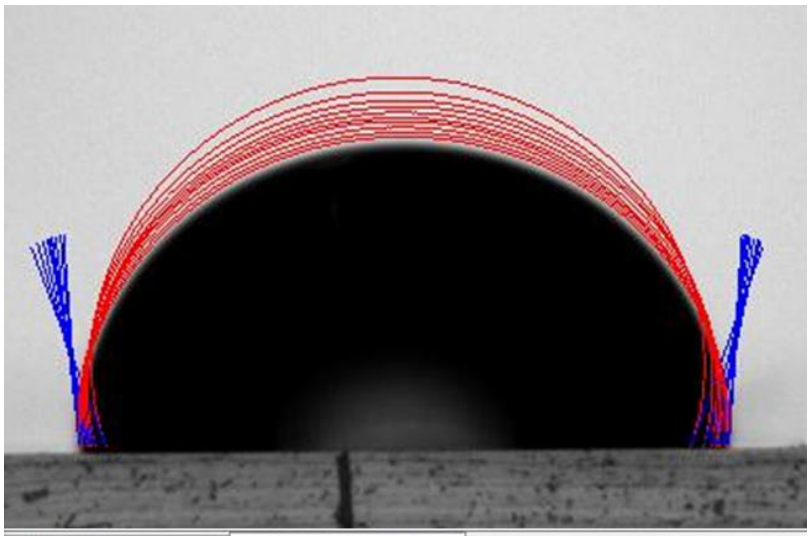

Surface tension results | Contact angle results

No.	Time	Theta (L)	Theta (R)	Theta (Avg)	Dev.	Height	Width	Area	Volume
3	119.9	101.63	101.63	101.63	0.00	1.923	3.544	22.08	13.73
4	180.0	101.06	101.22	101.14	0.08	1.904	3.544	21.86	13.53
5	240.0	100.66	100.79	100.73	0.07	1.887	3.545	21.65	13.34
6	299.9	100.11	100.34	100.23	0.11	1.869	3.545	21.42	13.14
7	359.9	99.65	99.56	99.60	0.05	1.850	3.545	21.20	12.94
8	419.9	98.92	98.99	98.96	0.04	1.831	3.546	20.97	12.73
9	479.9	98.28	98.40	98.34	0.06	1.813	3.546	20.74	12.53
10	539.9	97.69	97.78	97.73	0.05	1.794	3.546	20.50	12.32
	Mean:	100.27	100.33	100.30	0.06	1.877	3.545	21.52	13.23
Std.dev.:		0.52	0.51	0.51	0.01	0.018	0.000	0.21	0.19
Experiment: JKC2_contact angle_010414						Start at: 11:14:02 AM			
1	0.014	112.74	114.88	113.81	1.07	1.899	2.729	17.63	9.49
2	59.95	109.06	109.83	109.45	0.38	1.825	2.865	17.35	9.40
	Mean:	110.90	112.35	111.63	0.73	1.862	2.797	17.49	9.44
Std.dev.:		1.84	2.52	2.18	0.34	0.037	0.068	0.14	0.04
Experiment: JKC2_contact angle_010414						Start at: 11:16:44 AM			
1	0.014	114.59	115.45	115.02	0.43	1.926	2.726	17.96	9.72
2	59.94	114.71	114.28	114.49	0.22	1.894	2.758	17.78	9.62
3	119.9	109.42	110.08	109.75	0.33	1.830	2.878	17.48	9.50
4	180.0	105.66	107.27	106.47	0.80	1.788	2.955	17.29	9.42
5	240.0	105.94	106.13	106.03	0.10	1.759	2.965	17.05	9.25
6	299.9	103.11	104.61	103.86	0.75	1.731	3.003	16.88	9.14
7	360.0	102.77	104.16	103.47	0.70	1.707	3.014	16.69	8.99
8	419.9	102.70	103.07	102.88	0.18	1.687	3.020	16.50	8.85
9	479.9	101.92	101.54	101.73	0.19	1.669	3.031	16.33	8.73
10	539.9	101.34	101.05	101.20	0.14	1.652	3.036	16.17	8.61
	Mean:	106.22	106.76	106.49	0.38	1.764	2.938	17.01	9.18
Std.dev.:		1.59	1.59	1.59	0.09	0.030	0.036	0.19	0.12
Experiment: JKC2_contact angle_010414						Start at: 11:28:41 AM			
1	0.017	112.24	111.97	112.11	0.13	1.854	2.723	16.99	9.01
2	59.95	107.71	109.01	108.36	0.65	1.786	2.851	16.78	8.96
3	120.0	106.14	106.48	106.31	0.17	1.739	2.901	16.51	8.79
4	179.9	104.61	104.57	104.59	0.02	1.708	2.934	16.31	8.67
5	239.9	102.46	102.85	102.65	0.20	1.667	2.976	16.07	8.50
6	299.9	100.60	101.01	100.81	0.21	1.634	3.013	15.89	8.39
7	359.9	99.28	100.22	99.75	0.47	1.611	3.030	15.74	8.27
8	419.9	98.40	99.40	98.90	0.50	1.592	3.039	15.58	8.15
9	479.9	97.23	97.95	97.59	0.36	1.569	3.059	15.43	8.05
10	540.0	96.05	96.92	96.48	0.44	1.545	3.074	15.26	7.92
	Mean:	102.47	103.04	102.75	0.31	1.670	2.960	16.05	8.47
Std.dev.:		1.63	1.56	1.59	0.06	0.032	0.035	0.18	0.12
Experiment: JKC2_contact angle_010414						Start at: 11:42:45 AM			
1	0.012	110.58	109.69	110.14	0.45	1.837	2.871	17.52	9.53
2	59.96	105.85	105.44	105.64	0.20	1.764	2.991	17.21	9.38
3	119.9	103.29	103.13	103.21	0.08	1.724	3.047	17.01	9.26
4	179.9	101.63	101.47	101.55	0.08	1.693	3.075	16.79	9.10
5	240.0	100.51	99.94	100.23	0.29	1.664	3.097	16.58	8.95
6	299.9	98.64	98.73	98.69	0.04	1.638	3.120	16.40	8.81
7	359.9	98.87	97.67	98.27	0.60	1.620	3.128	16.26	8.70
8	419.9	96.60	95.54	96.07	0.53	1.592	3.180	16.21	8.67
9	480.0	95.09	94.34	94.71	0.38	1.566	3.196	16.01	8.51
10	539.9	94.30	93.69	93.99	0.30	1.545	3.196	15.80	8.34
	Mean:	100.54	99.96	100.25	0.30	1.664	3.090	16.58	8.92
Std.dev.:		1.59	1.61	1.60	0.06	0.029	0.032	0.17	0.12

.

Figure 6-3. Contact Angle of Diluted Red Dye on PDMS Layer

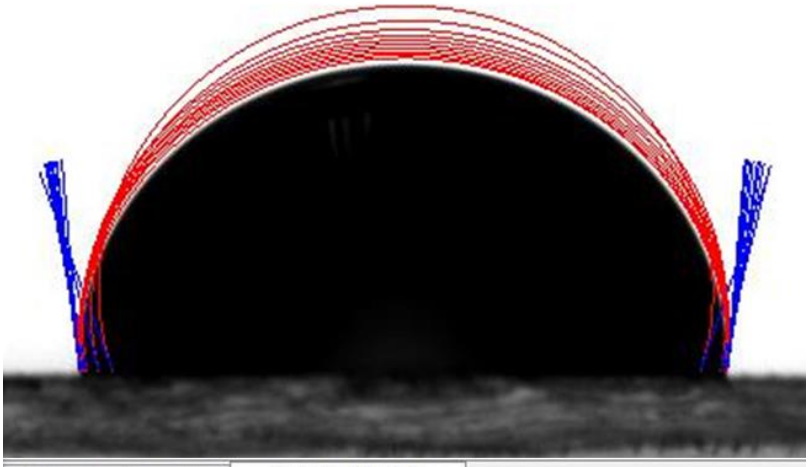

Surface tension results | Contact angle results

No.	Time	Theta (L)	Theta (R)	Theta (Avg)	Dev.	Height	Width	Area	Volume
	Mean:	95.46	94.44	94.95	0.60	1.667	3.536	19.15	11.10
Std.dev.:		1.35	1.41	1.37	0.11	0.030	0.023	0.23	0.20
Experiment: JKC2_contact angle Start at: 4:38:16 PM									
1	0.016	103.46	101.97	102.71	0.74	1.760	3.193	18.24	10.30
2	59.95	100.70	100.90	100.80	0.10	1.726	3.237	18.06	10.17
3	119.9	100.68	99.17	99.92	0.75	1.702	3.244	17.82	9.97
4	180.0	98.81	98.33	98.57	0.24	1.680	3.257	17.62	9.81
5	240.0	97.13	97.74	97.44	0.30	1.659	3.266	17.41	9.64
6	300.0	96.57	97.02	96.79	0.22	1.641	3.266	17.22	9.49
7	360.0	96.33	96.18	96.25	0.07	1.625	3.266	17.05	9.35
8	419.9	95.26	96.05	95.65	0.39	1.610	3.266	16.88	9.21
9	479.9	94.62	95.39	95.00	0.39	1.594	3.266	16.71	9.07
10	539.9	94.39	94.40	94.40	0.01	1.580	3.267	16.55	8.95
	Mean:	97.79	97.71	97.75	0.32	1.658	3.253	17.36	9.60
Std.dev.:		0.95	0.77	0.86	0.08	0.019	0.007	0.18	0.15
Experiment: JKC2_contact angle Start at: 4:56:26 PM									
1	0.022	97.07	96.39	96.73	0.34	1.821	3.591	20.96	12.74
2	59.95	96.60	96.09	96.35	0.25	1.803	3.591	20.77	12.57
3	119.9	96.41	95.77	96.09	0.32	1.783	3.592	20.58	12.40
4	179.9	95.87	95.33	95.60	0.27	1.766	3.592	20.39	12.23
5	240.0	95.32	95.00	95.16	0.16	1.750	3.592	20.21	12.06
6	300.0	94.93	94.59	94.76	0.17	1.736	3.591	20.04	11.92
7	360.0	94.44	94.09	94.27	0.18	1.721	3.591	19.86	11.76
8	420.0	93.86	93.63	93.74	0.12	1.706	3.591	19.70	11.61
9	479.9	93.48	92.99	93.24	0.25	1.692	3.590	19.53	11.45
10	539.9	93.03	92.42	92.72	0.30	1.676	3.589	19.35	11.29
	Mean:	95.10	94.63	94.87	0.24	1.745	3.591	20.14	12.00
Std.dev.:		0.44	0.42	0.43	0.02	0.015	0.000	0.17	0.15
Experiment: JKC2_contact angle Start at: 5:18:50 PM									
1	0.024	106.74	106.78	106.76	0.02	1.839	2.955	17.80	9.81
2	59.95	103.77	102.56	103.16	0.60	1.757	3.053	17.36	9.53
3	119.9	100.76	101.89	101.32	0.56	1.694	3.092	16.91	9.20
4	180.0	99.50	100.79	100.15	0.65	1.659	3.100	16.59	8.95
5	239.9	98.76	99.83	99.29	0.53	1.632	3.105	16.34	8.76
6	299.9	97.62	99.12	98.37	0.75	1.611	3.111	16.14	8.60
7	359.9	96.68	98.35	97.51	0.84	1.590	3.119	15.95	8.46
8	420.0	95.81	97.84	96.82	1.02	1.574	3.120	15.78	8.32
9	480.0	95.13	97.30	96.22	1.08	1.558	3.119	15.61	8.19
10	539.9	95.11	96.17	95.64	0.53	1.544	3.119	15.45	8.07
	Mean:	98.99	100.06	99.53	0.66	1.646	3.089	16.39	8.79
Std.dev.:		1.22	0.98	1.10	0.09	0.030	0.016	0.24	0.18
Experiment: JKC2_contact angle Start at: 5:32:24 PM									
1	0.024	110.12	108.95	109.53	0.59	1.815	2.872	17.29	9.36
2	59.95	104.30	103.55	103.93	0.38	1.743	3.043	17.23	9.42
3	119.9	101.41	100.46	100.93	0.48	1.698	3.125	17.11	9.37
4	179.9	100.40	99.29	99.84	0.55	1.670	3.143	16.89	9.20
5	240.0	99.61	98.35	98.98	0.63	1.647	3.152	16.69	9.04
6	300.0	98.26	97.12	97.69	0.57	1.627	3.164	16.51	8.91
7	360.0	97.33	96.33	96.83	0.50	1.609	3.172	16.34	8.78
8	419.9	96.52	95.38	95.95	0.57	1.590	3.173	16.15	8.62
9	479.9	96.24	94.80	95.52	0.72	1.575	3.174	16.00	8.50
10	539.9	94.87	94.93	94.90	0.03	1.560	3.175	15.84	8.37
	Mean:	99.91	98.92	99.41	0.50	1.653	3.119	16.60	8.96
Std.dev.:		1.44	1.41	1.42	0.06	0.025	0.030	0.16	0.12

Figure 6-4. Contact Angle of Diluted Blue Dye on PDMS Layer

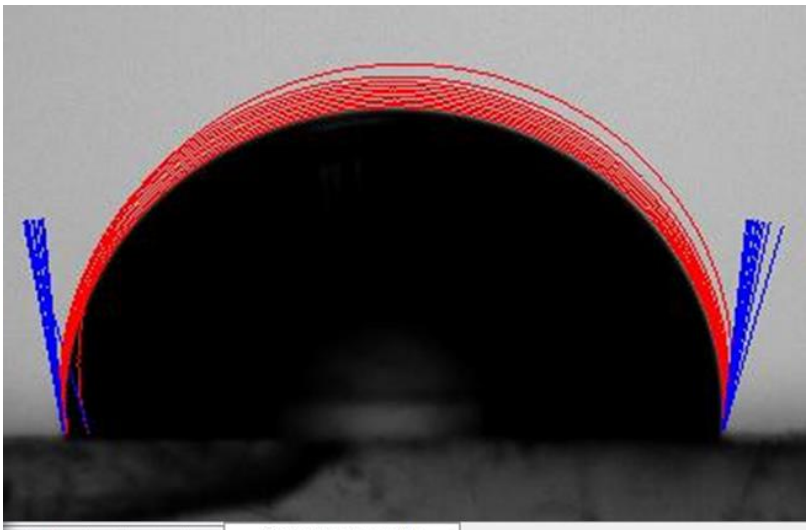

Surface tension results | Contact angle results

No.	Time	Theta (L)	Theta (R)	Theta (Avg)	Dev.	Height	Width	Area	Volume
	Mean:	105.53	107.27	106.40	0.87	1.722	2.847	16.06	8.42
Std.dev.:		1.29	1.21	1.24	0.09	0.023	0.026	0.16	0.10
Experiment: jkc2_contact angle_020414						Start at: 11:39:57 AM			
1	0.025	101.31	103.97	102.64	1.33	1.892	3.345	20.49	12.24
2	59.95	101.21	103.61	102.41	1.20	1.882	3.344	20.36	12.13
3	119.9	100.74	103.64	102.19	1.45	1.869	3.344	20.23	12.02
4	179.9	100.76	103.72	102.24	1.48	1.857	3.343	20.12	11.91
5	239.9	100.71	103.31	102.01	1.30	1.845	3.343	19.97	11.80
6	299.9	100.18	103.05	101.61	1.44	1.834	3.344	19.84	11.69
7	360.0	99.91	102.79	101.35	1.44	1.823	3.344	19.73	11.58
8	420.0	99.69	102.11	100.90	1.21	1.810	3.348	19.62	11.48
9	479.9	99.15	101.15	100.15	1.00	1.797	3.360	19.49	11.40
10	540.0	98.39	100.52	99.46	1.06	1.787	3.364	19.37	11.30
	Mean:	100.20	102.79	101.50	1.29	1.840	3.348	19.92	11.75
Std.dev.:		0.30	0.37	0.33	0.05	0.011	0.002	0.12	0.10
Experiment: jkc2_contact angle_020414						Start at: 11:52:44 AM			
1	0.030	107.13	108.45	107.79	0.66	1.916	3.088	19.51	11.24
2	59.95	107.11	108.28	107.69	0.58	1.901	3.088	19.35	11.12
3	119.9	105.82	106.94	106.38	0.56	1.866	3.120	19.10	10.94
4	179.9	103.53	103.68	103.60	0.07	1.826	3.170	18.83	10.76
5	239.9	102.83	102.62	102.73	0.11	1.801	3.196	18.67	10.64
6	299.9	101.97	101.43	101.70	0.27	1.782	3.220	18.56	10.57
7	360.0	101.04	100.79	100.92	0.13	1.766	3.228	18.40	10.44
8	420.0	100.53	100.12	100.33	0.21	1.752	3.233	18.27	10.33
9	479.9	100.08	99.69	99.88	0.20	1.739	3.234	18.12	10.22
10	539.9	99.51	99.44	99.47	0.04	1.727	3.235	17.99	10.11
	Mean:	102.96	103.14	103.05	0.28	1.807	3.181	18.68	10.64
Std.dev.:		0.91	1.12	1.01	0.07	0.021	0.019	0.16	0.12
Experiment: jkc2_contact angle_020414						Start at: 12:06:23 PM			
1	0.007	110.63	111.12	110.88	0.25	1.749	2.683	15.64	8.01
2	59.94	107.09	107.85	107.47	0.38	1.686	2.761	15.28	7.81
3	119.9	103.64	106.36	105.00	1.36	1.639	2.815	15.01	7.65
4	179.9	102.06	104.73	103.40	1.33	1.614	2.836	14.81	7.52
5	239.9	99.19	103.40	101.30	2.11	1.591	2.862	14.64	7.41
6	300.0	98.98	102.63	100.80	1.82	1.572	2.863	14.46	7.28
7	359.9	98.15	101.86	100.01	1.85	1.555	2.865	14.29	7.15
8	419.9	97.37	101.04	99.21	1.83	1.537	2.865	14.09	7.01
9	479.9	96.64	100.31	98.47	1.84	1.517	2.864	13.88	6.86
10	539.9	95.95	99.62	97.79	1.83	1.497	2.862	13.69	6.72
	Mean:	100.97	103.89	102.43	1.46	1.596	2.828	14.58	7.34
Std.dev.:		1.53	1.15	1.34	0.21	0.025	0.019	0.20	0.13
Experiment: jkc2_contact angle_020414						Start at: 12:21:59 PM			
1	0.010	106.86	106.07	106.47	0.39	1.803	3.053	18.07	10.08
2	59.96	101.16	102.34	101.75	0.59	1.742	3.157	17.81	9.94
3	120.0	100.22	100.85	100.54	0.31	1.716	3.174	17.60	9.77
4	179.9	99.89	100.16	100.03	0.14	1.698	3.173	17.39	9.61
5	239.9	99.35	99.37	99.36	0.01	1.681	3.173	17.19	9.45
6	299.9	98.24	99.03	98.64	0.40	1.663	3.172	16.97	9.28
7	359.9	97.85	98.09	97.97	0.12	1.646	3.171	16.77	9.12
8	420.0	96.88	97.73	97.30	0.43	1.630	3.170	16.58	8.97
9	479.9	96.16	97.31	96.73	0.58	1.615	3.169	16.41	8.82
10	540.0	95.63	96.60	96.12	0.48	1.600	3.169	16.23	8.69
	Mean:	99.22	99.76	99.49	0.34	1.680	3.158	17.10	9.37
Std.dev.:		1.02	0.89	0.95	0.06	0.020	0.012	0.19	0.15

Figure 6-5. Contact Angle of Diluted Yellow Dye on PDMS Layer

APPENDIX A.2: FLUID PROPERTIES – VISCOSITY

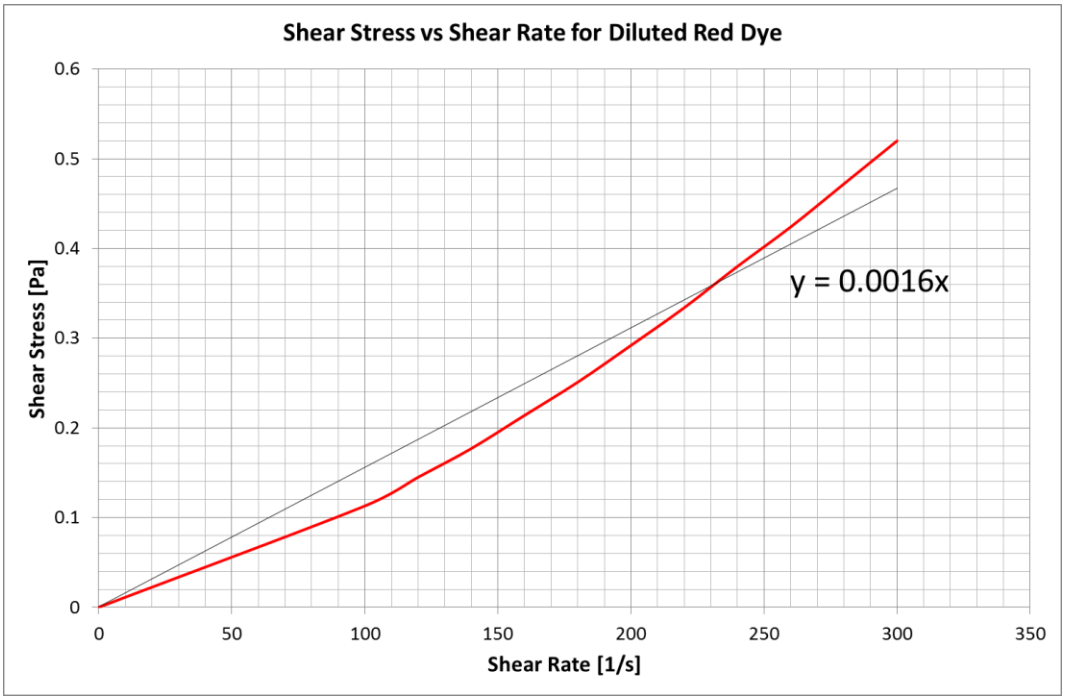

Figure 6-6. Viscosity of diluted red dye. (Viscosity = Gradient = 0.0016 Pa.s)

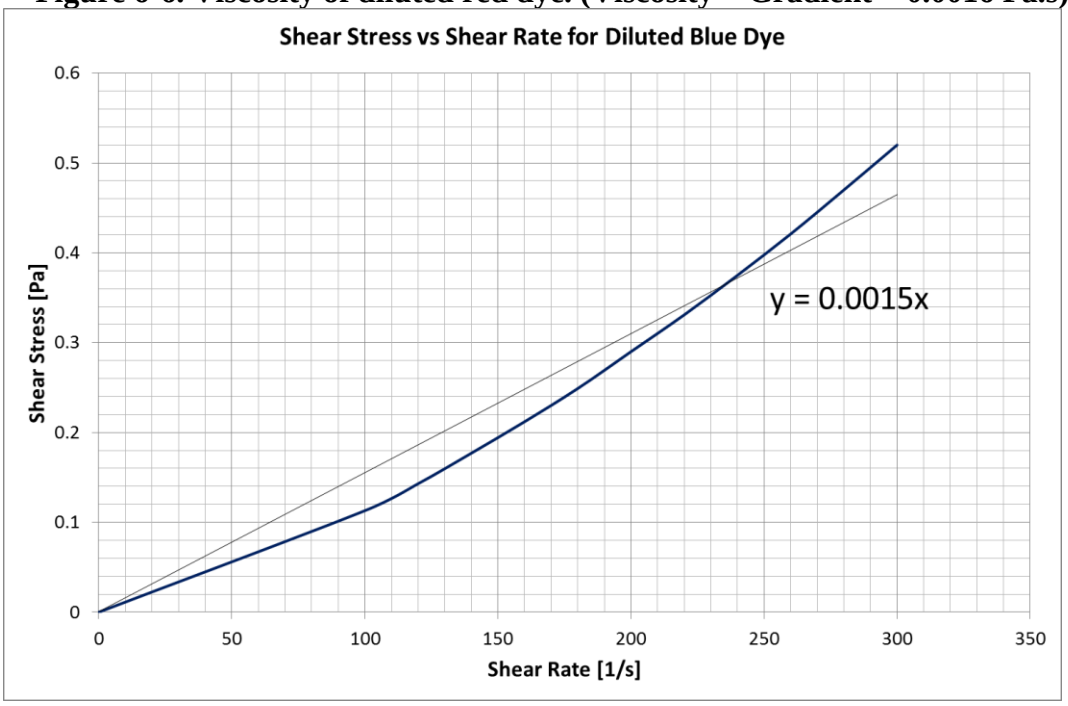

Figure 6-7. Viscosity of diluted blue dye. (Viscosity = Gradient = 0.0015 Pa.s)

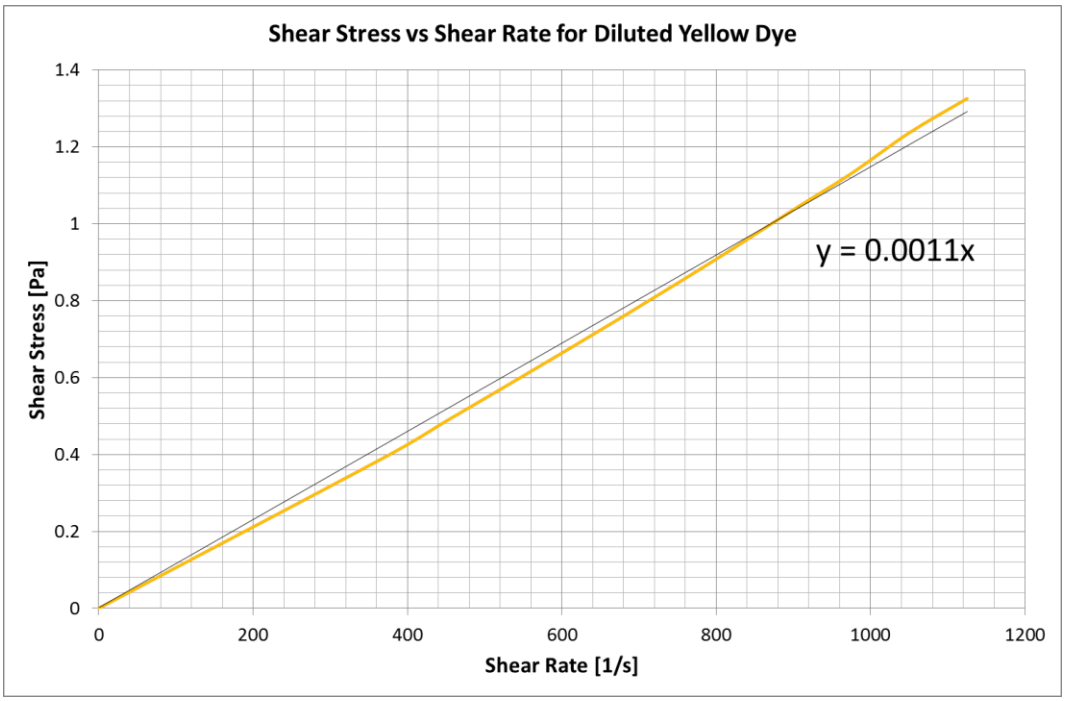

Figure 6-8. Viscosity of diluted yellow dye. (Viscosity = Gradient = 0.0011 Pa.s)

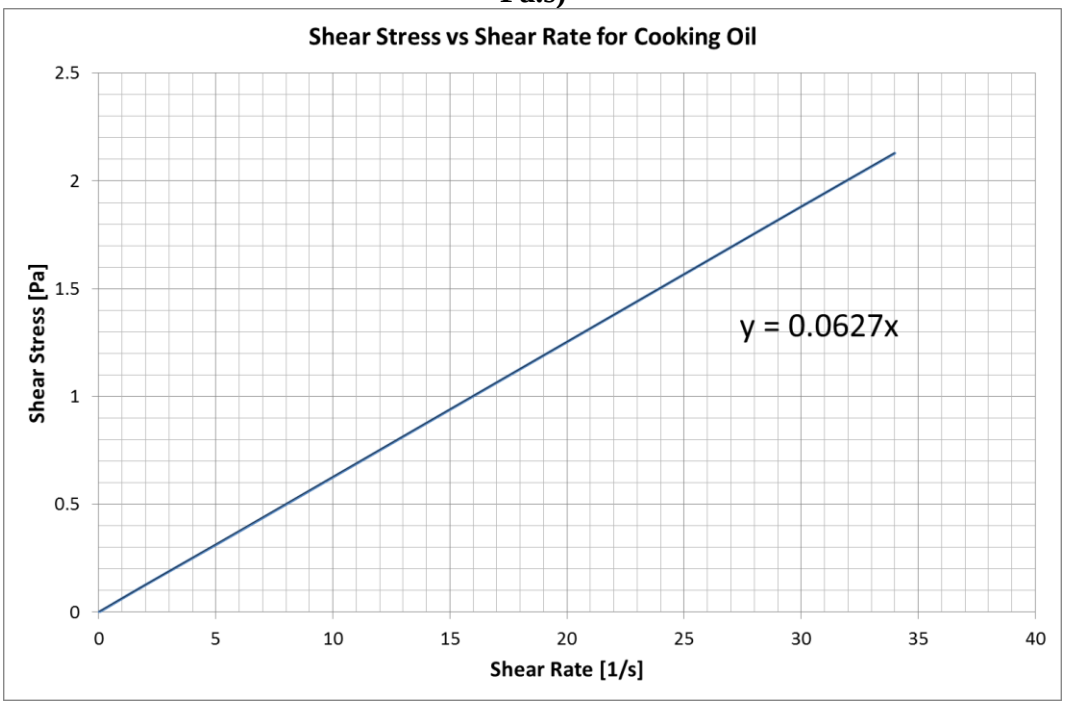

Figure 6-9. Viscosity of cooking oil. (Viscosity = Gradient = 0.0627 Pa.s)